Insights on Earthquakes and Thermochemical Heterogeneity in Earth's Deep Interior: Generation and Propagation of Seismic Waves

by

Meichen Liu

A dissertation submitted in partial fulfillment
of the requirements for the degree of
Doctor of Philosophy
(Earth and Environmental Sciences)
in the University of Michigan
2024

Doctoral Committee:

Professor Jeroen Ritsema, Co-Chair
Associate Professor Yihe Huang, Co-Chair
Assistant Professor Estéfan Garcia
Associate Professor Eric Hetland
Assistant Professor Zack Spica

Meichen Liu
meichenl@umich.edu
ORCID ID: 0000-0001-7952-340X

ACKNOWLEDGMENTS

I owe my deepest gratitude to my esteemed doctoral thesis advisors, Dr. Jeroen Ritsema and Dr. Yihe Huang, for providing me with the remarkable opportunity to work on intellectually stimulating research projects. Their support, invaluable mentorship, profound insights, encouragement, and remarkable patience have been the cornerstones of this endeavor, without which this project would not have come to fruition.

My heartfelt thanks extend to Dr. Zack Spica for his invaluable collaboration and guidance on the Distributed Acoustic Sensing project, which significantly expanded my knowledge and expertise. I am also indebted to Dr. Eric Hetland and Dr. Estéfan Garcia for their dedicated service on my thesis committee. Their constructive feedback and incisive scientific discussions at the University of Michigan have been instrumental in shaping my research.

I would like to express my gratitude to my parents for their support and understanding throughout this academic journey. I want to thank my lab mates, colleagues, and friends for their unwavering support, both professionally and personally: Dr. Daoyuan Sun, Dr. Marlon Ramos, Dr. Prithvi Thakur, Jing Ci Neo, Dr. Yi Wang, Dr. Yi Niu, Maria, Dr. Guolei Han, Dr. Xiaofei Pu, Dr. Bian Wang, Dr. Samuel Haugland, Dr. Ross Maguire, Dr. Sha Chen, Dr. Hong Shen, Dr. Madelyn Cook, Dr. Olivia Walbert, Dr. Yudan Liu, Dr. Dongdong Yao, Dr. Amir Salaree, Eric, Sydney, Yang, Leo, Yaolin, Peng, Xue, Bobo, Jiaqi, Hanxiao, Zixuan, Dongyuan, Dr. Liguo Jin, and Dr. Xian Li. They have all enriched my academic journey and contributed to my growth as a researcher. My deep appreciation also extends to Anne Hudon, Paula Frank, Chrissy Zigulis, Nico Spraggins, and all staff in the Earth department for their invaluable assistance in navigating the intricacies of academia and administration.

I would also like to acknowledge the funding sources that have made this research possible. This work was supported by the National Science Foundation (Grant Award EAR-2019379), Rackham International Student Fellowship, Rackham Predoctoral Fellowship, UMich Earth Department Ernest A. Novak Scholarship, and Michigan Institutes of Computational Discovery and Engineering Fellowship.

TABLE OF CONTENTS

LIST OF FIGURES

ABSTRACT

Seismic waves deliver valuable messages about earthquake faulting processes and Earth's structures. This thesis includes seismological studies that address two frontier research questions: how do earthquake faults rupture and how can seismic waves be used to map the subsurface velocity structures. Comprising three chapters dedicated to the investigation of earthquake source parameter estimation and an additional three chapters focused on the depth inversion of layered structures, this work advances our understanding of the source and structures spanning from Earth's deep interior to the surface.

In Chapter 2, we focused on estimating corner frequencies and stress drops for deep-focus earthquakes. By applying spectral ratio analysis based on empirical Green's function, the median stress drop estimates for deep-focus earthquakes are estimated to be one order of magnitude higher than those for shallow earthquakes. This difference suggests that the shear stress of faults in the mantle transition is on average higher the crust by an order of magnitude, indicative of the coexistence of multiple physical mechanisms in Earth's deep ruptures in the mantle.

In Chapter 3, we explore the potential biases in corner frequency estimates when utilizing the Brune source model for earthquakes with multiple subevents. We adopted a source time function decomposition approach that treats complex seismic sources as a composite of multiple Brune sources. We found that earthquake corner frequency correlates best with the corner frequency of the subevent with the highest moment release. This observation implies that when employing the Brune model, the estimated corner frequency, and consequently the stress drop of a complex earthquake, is predominantly determined by the most substantial subevent rather than the overall rupture area.

In Chapter 4, we introduced a point-wise stacking method for the precise estimation of stress drop. This approach optimizes the utilization of source spectra, resulting in a more robust estimate of corner frequencies, holding the potential to significantly mitigate the substantial variation often observed in stress drop estimates. In synthetic tests, the point-wise method yields stable less sensitive estimates to the quality of source spectra. This is promising for deep-focus earthquakes with limited high quality of source spectra.

In Chapter 5, we investigated the influence of velocity heterogeneity on imaging of the mantle transition zone using long-period SH-wave reverberations and assessed the method efficacy using synthetic waveforms simulated based on the spectral element method. The depth difference of 410-km discontinuity beneath the western US than the central-eastern US disappeared after we corrected travel times using a 3-D shear wave velocity model, highlighting the importance of accounting for 3-D velocity variations in subsurface imaging.

In Chapter 6, we investigated the global and regional cross-correlation of earthquake coda waves. Using Global Seismic Network, we established global correlograms that align with the correlograms derived from synthetic waveforms. Using the Southern California Seismic Network, we identified plausible reflection signals from the mantle transition zone. To enhance our interpretation of these reflection signals, we plan to conduct synthetic tests involving high-frequency coda waves at higher frequencies up to 0.1 Hz.

Finally, in Chapter 7, we conducted a preliminary exploration of Distributed Acoustic Sensing (DAS) data in Cordova, Alaska. We detected tidal signals strongly correlated with tide heights. We further applied surface wave inversion through cross-correlation to image the subsurface velocity structure. Our future work will focus on improving long-period signal detection and refining subsurface imaging techniques.

CHAPTER 1

Introduction

Seismic waves are generated by earthquake sources through fracture and slip of fault zone ruptures. These waves, propagating throughout the Earth and meticulously recorded by terrestrial and marine seismic stations, act as a comprehensive scanner, capturing every detail along their propagation and standing as the primary resource for investigating Earth's structure and earthquake mechanisms. In seismic recordings, the characteristics of seismic waves including the waveform amplitude, phase, and travel time, result from the convolution of the earthquake source, the media along the propagating path, and the site response close to the seismic station. By employing waveform analytical techniques in both time and frequency domains, we aim to address the two frontier research questions in seismology about understanding fault rupture processes of earthquake sources and mapping Earth's physical and thermal-chemical structures that seismic waves propagate through.

Earthquake sources are described by a multitude of parameters, including magnitude, depth, focal mechanism, rupture size and velocity, corner frequencies, and stress drop. The understanding of these parameters is fundamental for modeling and comprehending earthquake processes, contributing significantly to seismic hazard assessment and earthquake research (*Geller*, 1976). Corner frequencies and stress drops, among the plenty of parameters, emerge as particularly crucial. Corner frequency, denoting the frequency above which source spectra exhibit a power law decrease, plays a pivotal role in controlling the high-frequency energy release during an earthquake (e.g., *Savage*, 1972; *Motazedian and Atkinson*, 2005). High-frequency energy poses increasing danger to the ground and underground constructions, therefore the accurate estimation of corner frequencies is crucial in mitigating seismic hazards(e.g., *Papageorgiou and Aki*, 1983; *Purvance and Anderson*, 2003; *Sitharam and Anbazhagan*, 2007). Stress drop, on the other hand, representing the stress released during an earthquake, offers insights into the forces acting on the fault. It's an important parameter for understanding the physics of earthquakes and for ground motion modeling (e.g., *Anderson*, 1997; *Ye et al.*, 2016; *Kaneko and Shearer*, 2015). The stress drop can influence the frequency content of the seismic waves, with higher stress

drops generally leading to more high-frequency energy being released. Assuming a certain source model and fault structure, stress drop and corner frequency are usually linked with each other.

While previous studies have extensively examined corner frequencies and stress drops in shallow earthquakes(e.g., *Abercrombie*, 1995, 2014, 2015), the understanding of these parameters for deep-focus earthquakes (>350 km) in the mantle remains limited, so as the physical mechanisms. These infrequent seismic events, occurring near subducting plate boundaries, pose unique challenges due to their complex rupture processes under high-TP conditions of the mantle transition zone (MTZ). Shallow earthquakes are found to have a brittle failure mechanism in which the rock breaks due to abrupt fracture rather than deformation, which however is impractical for deep-focus earthquakes as rocks undergo ductile failure under high-TP (temperature and pressure) conditions of the MTZ (*Meade and Jeanloz*, 1991). Currently, two mechanisms of deep-focus earthquakes have been proposed. One is a shear-induced melting mechanism (*Green and Burnley*, 1989; *Green and Houston*, 1995) that is frictional melt acting as lubricant leads cascading failure, and the other is a phase transformation mechanism (*Aki*, 1972; *Kanamori et al.*, 1998) that is the volume decrease during the phase transformation forms large rupture, yet previous studies produce inconsistent results (*Persh and Houston*, 2004; *Poli and Prieto*, 2016). Therefore, Chapter 2 of this thesis identifies stress characteristics of deep-focus earthquakes, aiming to gain insight into the physical mechanism of earthquakes in the mantle transition zone.

The earthquake source model, initially proposed by J. Brune (*Brune*, 1970), has served as a cornerstone in source studies, being widely applied to both shallow and deep earthquakes (e.g., *García et al.*, 2004; *Allmann and Shearer*, 2009; *Oth*, 2013; *Huang et al.*, 2016; *Trugman et al.*, 2017; *Yu et al.*, 2020), including those explored in Chapter 2 concerning deep-focus earthquakes. However, the investigation on stress drop in Chapter 2 reveals a commonality in the occurrence of complex rupture processes for deep-focus earthquakes have complex rupture processes, in contrast to Brune's source model describing earthquakes as a single energy pulse. Considering that earthquakes are complex in a wide range of depths and magnitudes (e.g., *Huang and Ampuero*, 2011; *Ando and Kaneko*, 2018; *Ye et al.*, 2016; *Boatwright*, 1984), a question concerning the applicability of the Brune source model for stress drops estimation was raised. In light of this, Chapter 3 systematically investigates potential biases in corner frequency estimates when utilizing the Brune source model for earthquakes with multiple subevents. The pervasive complexity of earthquake sources is accompanied by a pronounced variability in stress drop estimates (e.g., *Allmann and Shearer*, 2007, 2009; *Uchide et al.*, 2014; *Goertz-Allmann et al.*, 2011), partly stemming from both source intricacies and the limited availability of high-quality

seismic waveforms. Previous studies employed a default stacking method, stacking entire source spectra based on quality control criteria, an approach suitable for a large dataset due to its averaging effect. However, this method introduces significant bias when dealing with a limited number of spectra, particularly relevant for deep-focus earthquakes, which occur near subducting plate boundaries at a frequency of 5% compared to crustal shallow earthquakes. To enhance the accuracy of average stress drop estimations, Chapter 4 introduces an innovative stacking method, addressing the challenges posed by the small number and poor quality of source spectra.

Following a comprehensive exploration of the physical mechanisms underlying deep-focus earthquakes, a nuanced understanding of the mantle transition zone (MTZ) becomes imperative, as it serves as the setting for 99% of these seismic events. Bounded by phase transformations of olivine occurring around 410 km and 660 km, the MTZ signifies a transitional region between the heterogeneous upper mantle and the more homogeneous lower mantle. The depth of the MTZ is intricately controlled by temperature and pressure, influencing global mantle convection, heat conduction, and the development of plumes, such as thermal upwellings from the core-mantle boundary beneath the MTZ to the Earth's surface that results in intraplate volcanism. Recordings of long-period ($T > 10$ s) shear waves are widely used to map seismic discontinuities and velocity gradients in the MTZ since short-period waves are highly attenuated at large depths. Most studies imaging the depth of MTZ are based on 1-D seismic reference profiles and ray theory. However, long-period shear waves are sensitive to seismic inhomogeneities in the mantle, so ray-theoretical calculations of traveltimes and waveform shifts may be inaccurate (*Tromp et al.*, 2005). One of the largest depth contrasts of the MTZ is the western and eastern US, with the MTZ depth beneath the western US found to be about 40 km deeper than the eastern US (*Gao and Liu*, 2014; *Shearer and Buehler*, 2019) using various imaging methods (e.g., receiver functions, SS precursors, ScS reverberations). This contrast of the MTZ depth raises the question of whether the difference between the tectonic-active western US and the tectonic-quiet eastern US originates from the depth down to MTZ. Chapter 5 of my thesis endeavors to enhance our understanding of how 3-D velocity structure improves the imaging of MTZ beneath the contiguous US and the relationship to its tectonic activities.

Simultaneously, the analysis of hours-long seismograms recorded after earthquakes provides a unique opportunity to capture the intricate interactions of seismic waves with Earth's layered structures (*Tkalčić et al.*, 2020). In the field of ambient noise, the cross-correlation function between two seismograms measures the similarity of waveforms. For a fully diffuse wavefield, the cross-correlation between continuous recordings at two seismic receivers precisely reflects the inter-receiver medium response (i.e., Green's func-

tions)(*Claerbout*, 1968). While the routine practice involves the reconstruction of surface wave correlograms through the stacking of cross-correlation functions, the creation of body wave correlograms encounters stringent limitations concerning seismic sources (*Zhan et al.*, 2010; *Poli et al.*, 2012; *Pedersen and Colombi*, 2018; *Boué et al.*, 2013; *Nishida*, 2013). An alternative approach involves utilizing recordings from teleseismic earthquakes. The application of correlation of seismic coda waves has been extended beyond our planet to celestial bodies such as Mars and the Moon (*Wang and Tkalčić*, 2023). This innovative methodology, unveiling diverse phases reflected from the core and refracted within Earth's interior, poses a critical question: Can coda correlation wavefields be effectively employed to image the mantle transition zone? Chapter 6 of this thesis presents the detection of reflections from the MTZ, meanwhile emphasizing the meticulous preprocessing required for the coda wave recordings.

After computing correlation wavefields of coda waves, our research extends to the realm of Distributed Acoustic Sensing (DAS), a cutting-edge technique revolutionizing source and structure studies, that also involves correlation analysis. Distributed Acoustic Sensing (DAS) is a rapidly developing geophysical technology that transforms optical fibers into an ultra-dense seismo-acoustic array. It measures phase changes in Rayleigh-scattered laser pulses, recording high-resolution data on acoustic vibrations or strain fluctuations. DAS has been applied to diverse fields such as subsurface structure imaging, seismic activity monitoring, earthquake sources investigations, urban vibrations, and the study of oceanic dynamics (*Lindsey et al.*, 2019; *Zhan*, 2020; *Lindsey and Martin*, 2021), capturing various signal types, including seismic waves in the solid Earth, ocean acoustic waves, and ocean gravity waves. Among these signals, long-period waves (i.e., period $>$ 1 s), particularly recorded at Ocean Bottom DAS (OBDAS), carry invaluable information. For instance, at around 1 Hz, seismic waves observed at OBDAS enable seismologists to conduct unprecedented high-resolution subsurface imaging (*Viens et al.*, 2023); at 0.1-1 Hz, prominent ocean surface gravity waves at OBDAS have been harnessed for precise ocean current measurements; at even lower frequencies in the millihertz range, recent OBDAS investigations have identified clear temperature changes associated with internal tidal fluctuations (*Ide et al.*, 2021; *Williams et al.*, 2023), achieving the required precision for measuring subtle seafloor strain signals after correcting temperature variations (*Zumberge et al.*, 2018). With its cost-effectiveness, robustness in harsh conditions and the widespread availability of marine fiber cables, OBDAS holds the potential to become a transformative observing system for the study of coastal ocean dynamics, seafloor geodesy, and geo-hazard investigations. However, several significant challenges need to be overcome to achieve these goals. The foremost challenge arises from OBDAS's decreasing sensitivity as the observed

signal's frequency increases (*Lindsey and Martin*, 2021). Additionally, our understanding of how OBDAS senses various signal types remains limited, resulting in substantial uncertainty and ambiguity when interpreting the data. Lastly, extracting precise physical variables from OBDAS records often requires well-designed calibration instrumentation. Hence, Chapter 7 primarily focuses on addressing these challenges and further exploring the potential applications of OBDAS.

In conclusion, this thesis represents a groundbreaking contribution to the field of seismology, offering novel insights into the complex dynamics of earthquakes and the structure of Earth's interior. The work in the realms of earthquake sources, not only provides a first estimation of stress drop for deep-focus earthquakes but also paves the way for more accurate and comprehensive investigations of earthquake physical mechanisms. In the study of the realms of structure, we challenge existing models and significantly enhance our understanding of the mantle transition zone by meticulously analyzing seismic waves and employing advanced methodologies of coda wave correlation. This thesis substantially enhances our understanding of source rupture processes and Earth's layered structures, playing a vital role in unraveling the mystery of our planet's internal dynamics.

CHAPTER 2

Stress Drop Variation of Deep-Focus Earthquakes Based on Empirical Green's Functions *

Abstract

We analyze source characteristics of global, deep-focus (>350 km) earthquakes with moment magnitudes (Mw) larger than 6.0–8.2 using teleseismic P-wave and S-wave spectra and an empirical Green's functions approach. We estimate the corner frequency assuming Brune's source model and calculate stress drops assuming a circular crack model. Based on P-wave and S-wave spectra, the one standard deviation ranges are 3.5–369.8 and 8.2–328.9 MPa, respectively. Based on the P-wave analysis, the median of our stress drop estimates is about a factor of 10 higher than the median stress drop of shallow earthquakes with the same magnitude estimated by Allmann and Shearer (2009, https://doi.org/10.1029/2008JB005821). This suggests that, on average, the shear stress of deep faults in the mantle transition zone is an order of magnitude higher than the shear stress of faults in the crust. The wide range of stress drops implies coexistence of multiple physical mechanisms.

2.1 Introduction

High temperatures and stresses in excess of 1,000 MPa should inhibit brittle failure at depths larger than 50 km. However, approximately 25% of earthquakes occur at these large depths (*Frohlich*, 1989), and they have nearly double-couple mechanisms. This suggests

*Chapter 2 is published in *Geophysical Research Letters*: Liu, Meichen, Yihe Huang, and Jeroen Ritsema. "Stress drop variation of deep-focus earthquakes based on empirical Green's functions." Geophysical Research Letters 47, no. 9 (2020): e2019GL086055.

that deep earthquakes involve shear faulting on a planar surface similar to crustal earthquakes.

Previous studies have proposed two physical mechanisms of deep-focus (>350 km) earthquakes as shear failures: (1) metastable phase transformation (e.g., *Green and Burnley*, 1989; *Green and Houston*, 1995; *Kirby*, 1987) and (2) shear-induced melting (e.g., *Aki*, 1972; *Kanamori et al.*, 1998; *Karato et al.*, 2001). In the first mechanism, small lenticular cracks nucleate as a result of the volume decrease during the olivine-to-spinel phase transformation and form macroscopic faults. In the second mechanism, frictional melts on preexisting faults lubricate the fault plane, reduce dynamic shear strength, and facilitate earthquake rupture. Once triggered, a shear instability evolves into a cascading failure (*Chen and Wen*, 2015), which may propagate at a supershear rupture velocity (*Zhan et al.*, 2015).

Previous studies of deep-focus earthquakes produced inconsistent results. For example, *Poli and Prieto* (2016) determined that the radiation efficiencies of intermediate-depth (30–350 km) and deep-focus earthquakes are different. *Persh and Houston* (2004) related distinct changes of aftershock productivity at depths of 300 and 550 km to different metastable phase transformations. Both studies suggest a change of the rupture mechanism with depth. In contrast, *Campus and Das* (2000) did not observe an obvious difference in the spectral properties and the source time functions of intermediate-depth and deep-focus events. The global invariance of strain drops with depth based on the analysis of source time functions (*Vallée*, 2013) indicates that one single mechanism could be responsible for all earthquakes.

In this paper, we evaluate whether stress drops of shallow and deep-focus earthquakes are significantly different. Stress drop is the difference between shear stresses along the fault before and after an earthquake. It is a fundamental parameter for understanding the physics of the rupture process (*Kanamori and Brodsky*, 2004). If the shear-failure processes are similar, deep-focus earthquakes should exhibit higher stress drops than shallow earthquakes due to larger fault shear stresses.

Early studies by *Aki* (1972) and *Kanamori and Anderson* (1975) suggested that stress drops of deep earthquakes are an order of magnitude larger than the range of 1–10 MPa of crustal earthquakes. However, recent analyses of larger data sets indicate that stress drops of crustal earthquakes can vary significantly and that stress drops of shallow and deep earthquakes are similar. For example, the stress drops of 95% of global crustal earthquakes studied by *Allmann and Shearer* (2009) using globally averaged empirical Green's functions (eGfs) are between 0.22 and 66 MPa. *Poli and Prieto* (2016) found that the stress drops of 95% of earthquakes at depths of 400–700 km are 3.6–49.2 MPa from the analysis

of source time functions.

To measure stress drops of deep-focus earthquakes (Fig. 2.1), we analyze teleseismic P-wave and S-wave spectra using the spectral ratio approach based on eGfs (*Huang et al.*, 2016). We compare our stress drops of deep-focus earthquakes to those of shallow earthquakes estimated by *Allmann and Shearer* (2009), the only published stress drop study for global shallow earthquakes based on eGfs.

2.2 Methods

2.2.1 Corner Frequency and Stress Drop Estimates

The spectrum of a teleseismic P wave or S wave is $u(f) = S(f)P(f)R(f)$, where the factors S, P, and R are the source, path, and receiver-side contributions, respectively. We can determine the ratio of the source spectra $S_M(f)$ and $S_{eGf}(f)$ by dividing the P-wave or S-wave spectra u_M for a large earthquake (i.e., the master event) by the spectra u_{eGf} for a smaller nearby earthquake (i.e., the eGf) recorded at the same station (*Aki*, 1967; *Abercrombie*, 2015; *Frankel and Wennerberg*, 1989; *Imanishi and Ellsworth*, 2006; *Mueller*, 1985). For the Brune source model (*Brune*, 1970) $S(f, f_c) = M_0/(1 + (f/f_c)^2)$, where M_0 is the seismic moment and f_c is the corner frequency, $S_M(f)/S_{eGf}(f)$ has a sigmoidal shape with a high plateau at low frequencies determined by the ratio of the seismic moments and a spectral fall-off between the corner frequencies of the master event and the eGf. From here on, we denote the corner frequencies of the master event and the eGf as f_M and f_{eGf}.

Abercrombie (2015) recommended to select eGfs that are located within one-source dimension of the master event in order to cancel out $P(f)$ and $R(f)$.We therefore choose eGfs at hypocentral distances within 100, 300, and 500 km from master events with moment magnitudes in the range of 6–7, 7–8, and 8–9 (only two events), respectively. Using a distance threshold of 300 km for the two Mw 8 events does not significantly change our stress drop estimates (Fig. 2.5). We require the eGfs to have magnitudes that are at least 0.5 lower to ensure that fM and feGf are distinguishable. We allow eGfs to have different focal mechanisms because the source-radiation effects are small when spectra are averaged from stations over a wide range of source azimuths (*Calderoni et al.*, 2015; *Ross and Ben-Zion*, 2016).

The source radius r of a master earthquake is related to f_c by $r = kv/f_c$, where v is the S-wave velocity varying with depth. We assume a circular shear crack model, so the stress drop $\Delta\tau$ is related to r as $\Delta\tau = 7M_0/16r^3$ (*Eshelby*, 1957). Here, we assume that the rupture velocity is constant and 90% of the shear-wave velocity and choose $k_P = 0.32$ for

P wave and $k_S = 0.21$ for S wave following (*Madariaga*, 1976) to facilitate the comparison with (*Allmann and Shearer*, 2009). It is possible that the stress drop variability observed in this study stems from rupture velocity variation. Both stress drop and rupture velocity determine the corner frequency and the rupture velocities of individual earthquakes that are poorly constrained (*Chounet et al.*, 2018; *Houston*, 2015). This is the case for deep-focus as well as shallow earthquakes (*Allmann and Shearer*, 2009; *Vallée*, 2013). (*Houston*, 2015) has shown that the majority of deep-focus earthquakes have rupture velocities that range between 50% and 90% of the shear-wave velocity. If we assume that the rupture velocity is 50% of the shear-wave velocity, $\Delta\tau$ estimated from P-wave and S-wave spectra would increase by a factor of $\sim$2.5 and $\sim$1.7, respectively, based on estimates of k_P and k_S by (*Sato and Hirasawa*, 1973) and (*Kaneko and Shearer*, 2014). The increase is small compared to the differences in the stress drops of deep-focus and shallow earthquakes (Fig. 2.6).

2.2.2 P-Wave and S-Wave Spectral Ratio Analysis

We analyze P-wave and S-wave spectra using vertical-component and transverse-component waveforms recorded at epicentral distances smaller than 85$\circ$. We apply the multiwindow method (*Huang et al.*, 2016; *Imanishi and Ellsworth*, 2006) to stack spectra for five windows that are each 40 s long and overlap by 20 s. The first window begins 5 s before the theoretical (i.e., PREM *Dziewonski and Anderson*, 1981) arrival time. The windows include coda waves with important source information (*Aki and Chouet*, 1975). We find that stacked spectra for window lengths from 60 to 120 s are not significantly different.

We use data with a signal-to-noise ratio (SNR) higher than 2 in each of the frequency bands 0.025–0.1, 0.1–0.4, 0.4–0.9, and 0.9–2.0 Hz. The SNR is defined as the ratio of the P-wave or S-wave amplitude and the average amplitude of the noise in the 40-s-long window before the P-wave and S-wave onsets. We average the spectral ratios from at least three stations. The corner frequency f_M may be underestimated when it is within a factor of 1.5 (*Ruhl et al.*, 2017) to 3.0 (*Abercrombie*, 2015) of the maximum signal frequency. It is difficult to resolve f_M if the low-frequency plateau is not distinguishable from the high-frequency spectral fall-off, but we can estimate f_M reliably if it has a value between 0.05 and 0.67 Hz. Due to the limited bandwidth of our data, f_{eGf} is poorly resolved for most eGfs. In addition, we require that the magnitude difference between the master events and the eGfs, determined by moment ratios, is within 0.5 units of the magnitude difference in the ANSS Comprehensive Earthquake Catalog (Fig. 2.7).

After resampling the P-wave and S-wave spectra evenly in the log domain, we estimate

f_M of the master event and its uncertainty by fitting the average spectral ratio to the theoretical curve in the 0.025- to 2.0-Hz frequency range using two approaches. The first approach is based on a grid search. We compute the least squares misfit between the stacked and the theoretical spectral ratios (assuming the Brune model) as a function of f_M and f_{eGf} for a fixed moment ratio determined by the spectral ratio at the lowest frequencies. In the second approach, we estimate f_M using the trust-region-reflective least squares algorithm by *Branch et al.* (1999). We bootstrap the residuals between the observed and the best fit spectral ratios at each frequency and create a synthetic spectral ratio by adding the bootstrapping residuals to the best fit spectral ratios. We repeat this process 1,000 times to obtain a Gaussian distribution of f_M values for 1,000 synthetic spectral ratios. The 95% confidence interval is similar to the range of resolved values along the 1.01 misfit contour (defining the minimum misfit to be 1). We retain an estimate of f_M only when its distribution has a two standard deviation smaller than 0.05 in the log domain, which is within 0.89–1.12 times the best fit corner frequency. We likely underestimate the uncertainties in the estimate of the corner frequency because we have not considered the effects of imperfect cancelation of propagation path and site effects in our analysis.

Fig. 2.2 illustrates our analysis for the 2013 Sea of Okhotsk earthquake (Event 5 in Table S1). Fig. 2.2a shows station-averaged P-wave spectral ratios for three eGfs (1 December 2009, Mw6.3; 1 October 2013, Mw 6.7; and 24 May 2013, Mw 6.7). The estimates of f_M range from 0.075 to 0.15 Hz. Three panels in Fig. 2.2b show that the spectra of the three eGfs can be matched by theoretical ratios within a misfit of 1.01 when estimates of f_M of Event 5 vary between 0.11-0.13 Hz for eGf 1, 0.074-0.08 Hz for eGf 2, and 0.14-0.16 Hz for eGf 3. The bootstrapping results in Fig. 2.2c indicate that f_M is 0.12, 0.08, and 0.15 Hz for eGfs 1, 2, and 3, respectively. In Table S1, we report that Event 5 has a corner frequency $f_M = 0.11 \pm 0.01$ Hz based on this analysis.

2.3 Estimates of Corner Frequencies and Stress Drop

Our analysis is based on global waveform data of earthquakes from 2000 to 2018 listed in the ANSS Comprehensive Earthquake Catalog with focal depths larger than 400 km and moment magnitudes higher than 5.5. Using 2,860 P-wave recordings of 28 earthquakes and 2,296 S-wave recordings of 29 earthquakes, we measure 116 and 95 corner frequencies from analyses of P-wave and S-wave spectra that meet the quality control criteria. We show observed and modeled spectral ratios in Fig. 2.8 and document source parameters in Table S1.

Fig. 2.3a and 2.3b show estimates of f_M from the analysis of P waves and S waves,

respectively. The P-wave corner frequencies vary from 0.05 to 0.67 Hz, which is the same as the resolvable frequency range, whereas the S-wave corner frequencies vary from 0.06 to 0.26 Hz. In Fig. 2.9, we show that the estimates of f_M are similar for the Boatwright model (*Boatwright*, 1980), which predicts a steeper decrease of the source spectra at frequencies higher than f_M. f_M varies by a factor of 6 (for S waves) to 10 (for P waves), but a dependence on magnitude is not obvious. For example, f_M for Events 41 and 53 (see Fig. 2.8) are similar, although the event magnitudes are different by about 1. The magnitudes of Events 36, 42, and 53 are between 7.6 and 7.9, but estimates of f_M for these events differ by a factor of 10.

Since f_M does not depend on magnitude, the stress drop $\Delta\tau$ increases with magnitude (Fig. 2.3c and 2.3d). *Poli and Prieto* (2016) also observe an increase of $\Delta\tau$ with moment for 415 earthquakes deeper than 100 km by measuring total rupture durations from source time functions. However, f_M estimated in this study is affected more by the time at which the moment rate is the highest than by the total rupture duration (*Archuleta and Ji*, 2016). Furthermore, the increase of the stress drop in Fig. 2.3c and 3d may be due to the narrow range of resolvable corner frequencies in our data set. According to our spectral ratio analysis, several master events and corresponding eGfs in Fig. 2.8 have similar seismic moments and therefore similar magnitudes, especially for P-wave results (Fig. 2.7). Nevertheless, the ranges of P-wave and S-wave $\Delta\tau$ are similar, and omitting these earthquake pairs does not change our interpretation (Fig. 2.10). One standard deviation ranges of $\Delta\tau$ for P waves and S waves are 3.5–369.8 and 8.2–328.9 MPa, respectively. Their median values of 50.0 and 51.0 MPa are higher than the estimate of 13.4 MPa from *Poli and Prieto* (2016).We do not observe a dependence of $\Delta\tau$ on event depth and focal mechanism (Fig. 2.11 and Fig. 2.12 *Shearer et al.* (2006)). Moreover, the earthquakes with the highest (Event 42) and lowest (Event 54) P-wave corner frequencies and stress drops have double-couple components smaller than 40%. Since the Brune source model is based on shear failure of a planar fault, the corner frequencies of non-double-couple events may be poorly resolved.

In Fig. 2.4, we compare our P-wave estimates of f_M and $\Delta\tau$ to the estimates from *Allmann and Shearer* (2009) who analyzed shallow (<50 km) earthquakes using teleseismic P waves and globally averaged eGfs. The highest value for $\Delta\tau$ in *Allmann and Shearer* (2009) is 1,000 MPa. Assuming a Gaussian distribution, 95% of their stress drops are between 0.22 and 66 MPa and have a median value of 4.0 MPa. Thus, Fig. 2.4 suggests that the median stress drop of shallow earthquakes is 12.5 times smaller than the median stress drop of deep-focus earthquakes in the same magnitude range.

2.4 Dissusion

Our study indicates that the stress drop of deep-focus earthquakes is higher than the stress drop of crustal earthquakes. This suggests that the mantle transition zone can accommodate shear faulting with higher stress drops. However, the difference in stress drop of shallow and deep-focus earthquakes may partly originate from the applied approaches. *Shearer et al.* (2019) compared the spectral ratio approach used in this study with the global eGf fitting approach used by *Allmann and Shearer* (2009). They found that, for the Brune source model, corner frequencies of a cluster of Landers aftershocks estimated using the spectral ratio approach are systematically higher than estimates using the global eGf fitting approach. However, it cannot explain the one order of magnitude difference of median stress drops of shallow and deep-focus earthquakes shown (Fig. 2.4c). Moreover, assuming the Boatwright source model, the estimated corner frequencies have less scatter, and there is better agreement between the two approaches.

The one standard deviation range of 3.5–369.8 MPa of the estimated stress drop (using P waves) implies that multiple physical mechanisms underlie deep-focus earthquake faulting. Shear-induced melting can accommodate shear failure with higher stress drops than phase transformation due to the large reduction of fault friction. The stress drop of the 1994 Mw 8.3 Bolivia earthquake is estimated to be higher than 100 MPa (e.g., *Antolik et al.*, 1996; *Kikuchi and Kanamori*, 1994), and faulting may have caused shear-induced melting (*Kanamori et al.*, 1998; *Zhan et al.*, 2014). In contrast, the 2013 Mw 8.3 Sea of Okhotsk earthquake has a much smaller stress drop of 12–15MPa (*Ye et al.*, 2013) and may have been triggered by phase transformation (*Zhan et al.*, 2014). Deep-focus earthquakes may also involve a combination of shear melting and phase transformation (*Fan et al.*, 2019; *Meng et al.*, 2014; *Zhan*, 2017).

In our analysis, the source radius r can be much smaller than the dimension of the rupture plane estimated from finite-fault inversions or back-projection studies because our estimate of the corner frequency is primarily sensitive to the area of the fault plane with highest slip. For example, we estimate that r =9.4 km (i.e., rupture dimension of 278 km2) for the 24 May 2013 Sea of Okhotsk earthquake (Event 5 in Table S1). Although *Ye et al.* (2013) determined by kinematic slip inversion that the fault plane area was 180×60 km^2, our estimate of rupture dimension is consistent with the highest slip in *Ye et al.* (2013) ($\sim$600 km^2 for the 9.9-m slip contour in their Fig. 2.1 and Fig. 2.13a) and in *Zhan et al.* (2014) ($\sim$314 km2 for the 8.0-m slip contour in their Figure S3a). Similarly, we estimate that the rupture area of the 19 August 2018 Fiji earthquake (Event 19 in Table S1) is 800 km2 (r = 16.2 km), which is 10 times smaller than 80×100 km^2 determined by *Fan*

et al. (2019) from a back-projection analysis. Thus, stress drops interpreted in this study are primarily sensitive to the largest slip (*Archuleta and Ji*, 2016; *Luco*, 1985), whereas finite-fault inversions and back-projection analyses resolve stress drops based on the overall dimension of the fault plane. Consequently, it is important to study stress drop variations using a consistent approach.

Our results suggest that the fault shear stress in the mantle transition zone is one order of magnitude higher than in the crust. This is significantly smaller than the two orders of magnitude difference of pressure in the crust and mantle (hundreds of MPa vs. tens of GPa). One explanation is high P-T experiments (e.g., *Green et al.*, 2015; *Paola et al.*, 2015) indicate that ground-boundary sliding may weaken faults if accompanied by phase transformation, with very low frictional resistance (*Green et al.*, 2015) slightly depending on confining stress (*Tingle et al.*, 1993). In this case, shear failure can occur under shear stresses significantly smaller than static friction. Moreover, buoyancy forces caused by phase transformation that reach crustal shear stress (*Bina*, 1997; *Yoshioka et al.*, 1997) or even higher level (*Goto et al.*, 1987) can trigger rupture of faults.

2.5 Conclusion

We measure the corner frequencies of global deep-focus earthquakes using the spectral ratio analysis based on teleseismic P-wave and S-wave spectra and a Brune source model. We find the one standard deviation ranges of P-wave and S-wave stress drop estimates are 3.5–369.8 and 8.2–328.9 MPa, respectively. The medians of the P-wave and S-wave stress drop estimates are 50.0 and 51.0 MPa, respectively. These medians are about one order of magnitude higher than the median stress drop of global shallow earthquakes estimated by *Allmann and Shearer* (2009). The large variation of stress drops implies that both phase transformation and shear heating processes play important roles in the rupture processes of deep-focus earthquakes. Despite the two orders of magnitude difference in the pressure in the mantle transition zone and crust, the comparison of median stress drops of shallow and deep-focus earthquakes suggests that the fault shear stress in the mantle is one order of magnitude higher than shear stresses in the crust.

2.6 Figures - Chapter 2

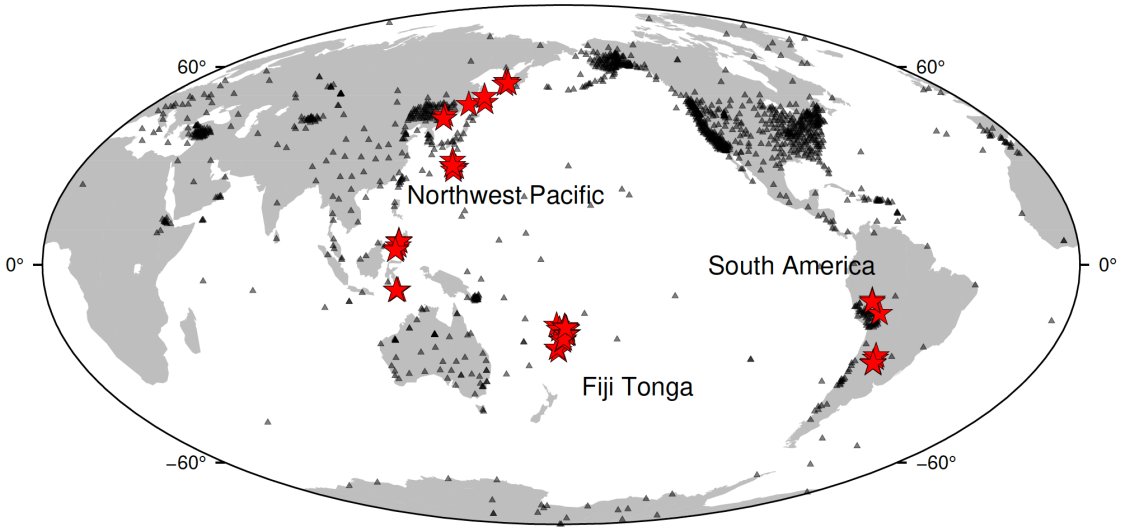

Figure 2.1: Global distribution of master events (stars; see also Table S1) and stations (triangles) used in this study

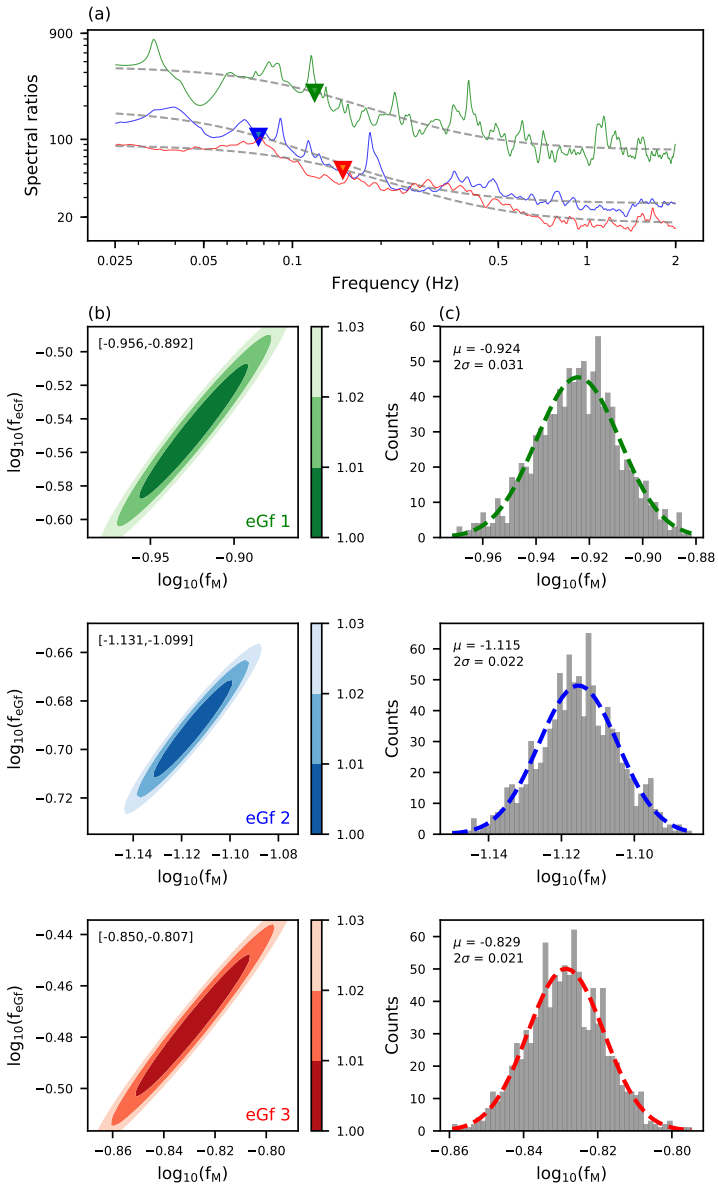

Figure 2.2: (a) Estimates of the S-wave spectral ratios (green, blue, and red solid lines) and corner frequencies (green, blue, and red triangles) of Event 5 (24 May 2013; Sea of Okhotsk) based on three eGfs. The best fit ratios are shown with dashed lines. (b) Contours of the misfit (scaled to minimum misfit) as a function of the corner frequencies of the master event (x axis, log10(f_M)) and the eGf (y axis, log10(f_{eGf})) for the same three eGfs as in (a). Values in the upper left of each panel indicate the variation of log10(f_M) for a misfit of 1.01. (c) Histograms of the estimated log10(f_M) based on bootstrapping analysis. Dashed curves are best fit Gaussians. Means (μ) and two standard deviations ($s\sigma$) are indicated on the upper left of each panel. Note that spectral ratios and results of grid search and bootstrapping for the same eGf are depicted in the same color.

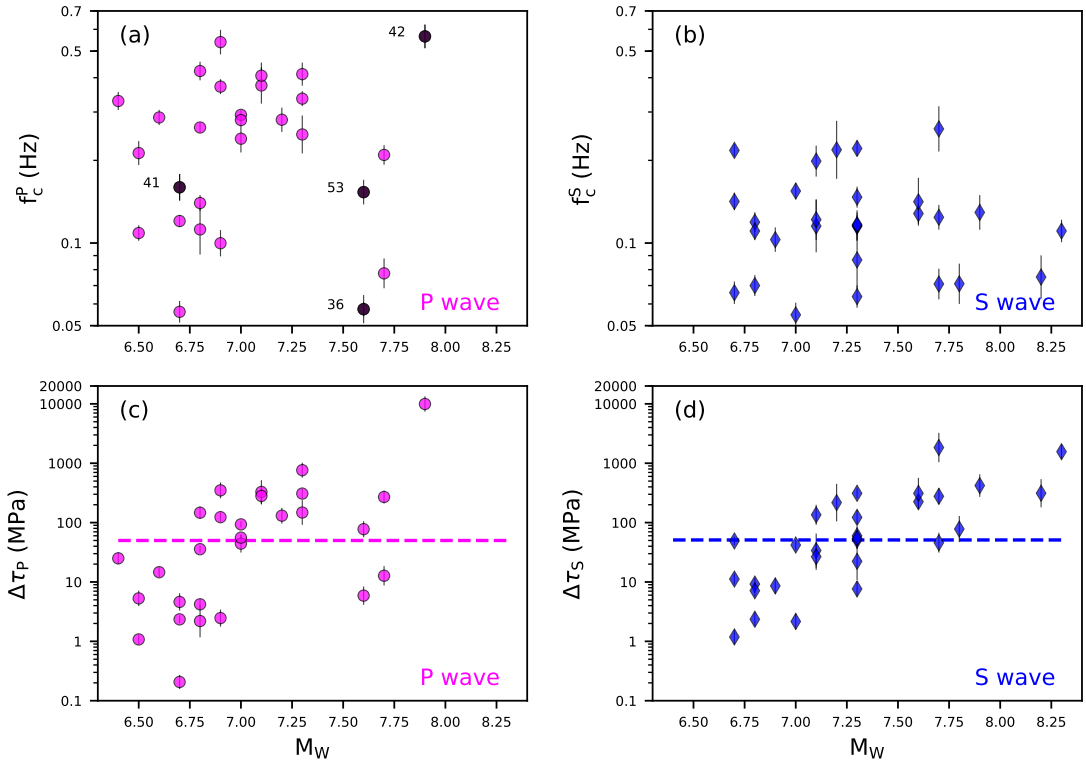

Figure 2.3: Corner frequencies (a, b) and stress drops (c, d) of master events as a function of moment magnitudes estimated from P-wave (a, c) and S-wave (b, d) spectra using Brune's source model. Vertical lines indicate 2σ uncertainties determined by bootstrapping analysis. (a) Numbers to the left of four data points are the associated event numbers in Table S1. In (c) and (d), shaded areas are one standard deviation ranges of P-wave (3.5–369.8 MPa) and S-wave (8.2–328.9 MPa) stress drop estimates; dashed lines in (c) and (d) indicate medians of P-wave (50.0 MPa) and S-wave (51.0 MPa) stress drops estimates.

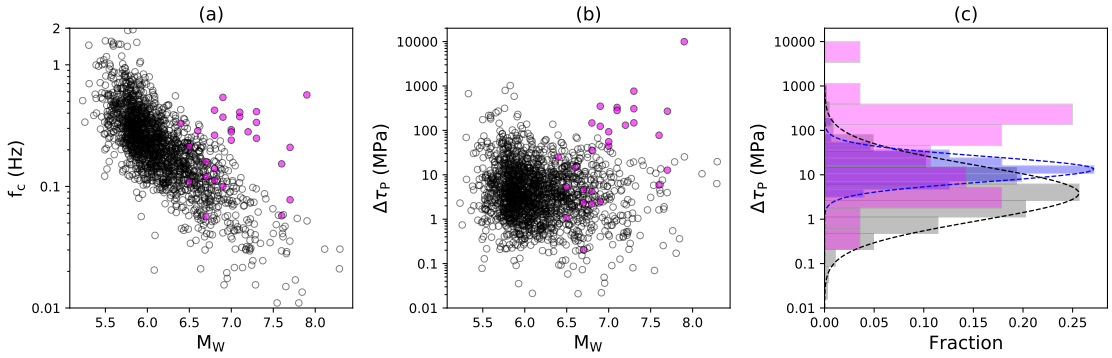

Figure 2.4: (a) Corner frequencies and (b) stress drops of shallow earthquakes (white circles) by *Allmann and Shearer* (2009) and estimates for deep-focus earthquakes in this study (magenta circles). (c) Histograms of the stress drop distributions corresponding to data in (a) and (b). Dashed lines are Gaussian contours fitting to histograms. The median stress drops of magenta, blue, and gray histograms are 50.0, 13.4, and 4.0 MPa.

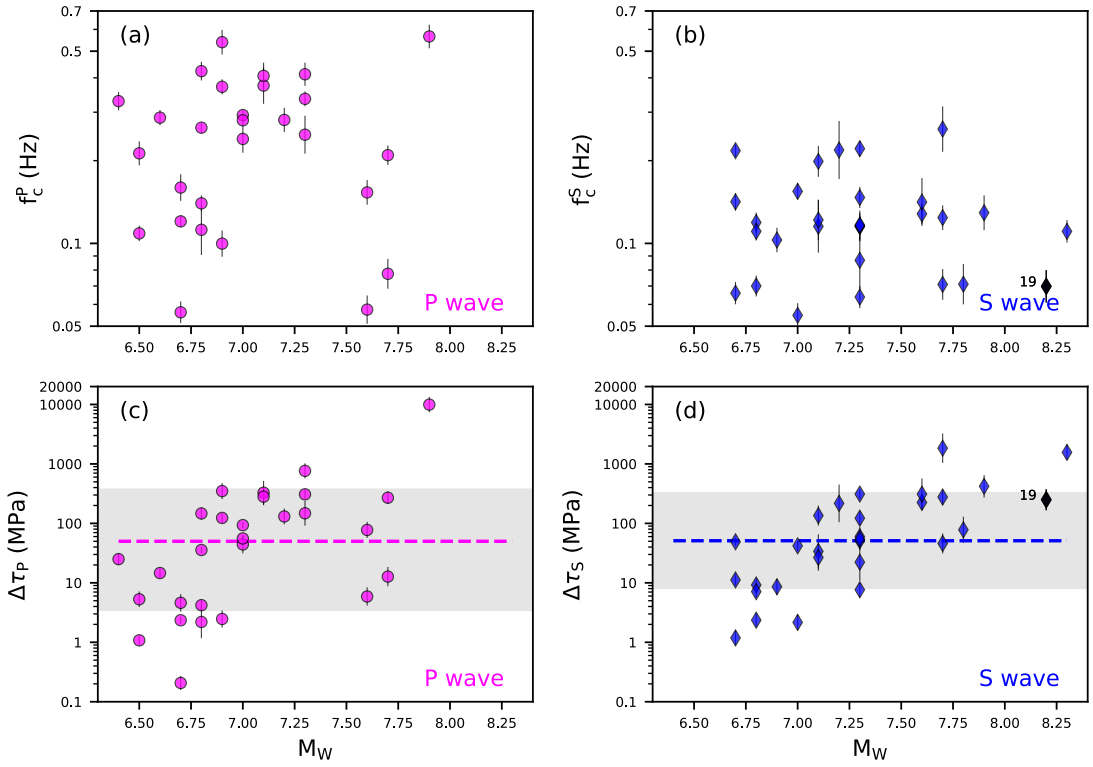

Figure 2.5: Corner frequencies ((a) and (b)) and stress drops ((c) and (d)) of master events as a function of moment magnitudes estimated from P-wave ((a) and (c)) and S-wave spectra using Brune's source model considering eGfs within 300 km. The only event having eGfs further than 300 km is event 19 in S-wave estimation (black diamonds in (b) and (d)). Compared to Figure 3 in the main text, 4 out of 9 eGfs of event 19 are excluded, causing its best-fit corner frequency to change from 0.075 to 0.070 Hz and stress drop to decrease from 312.5 to 250.0 MPa. The S-wave one standard deviation range thus changes from 8.2-328.9 MPa to 8.2-324.3 MPa, whereas the S-wave median is not affected

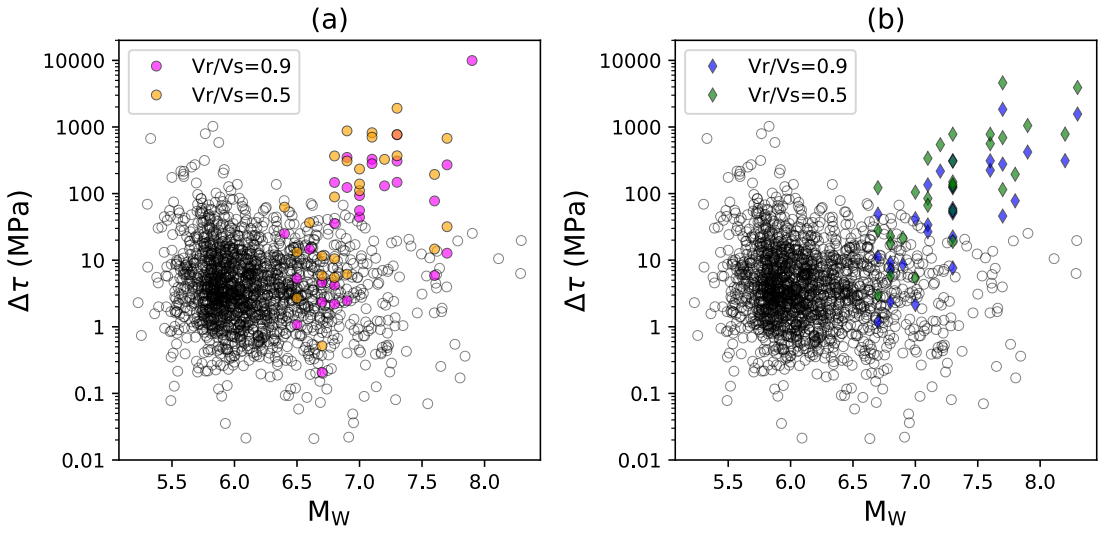

Figure 2.6: P-wave (a) and S-wave (b) stress drop estimates of deep-focus earthquakes (colored circles) compared to P-wave shallow earthquakes (open circles). The colored circles are estimates of the stress drop under the assumption that the rupture velocity is 50% and 90% of the shear wave velocity. The estimates of the stress drops vary by a factor of 2.5 or 1.7 for P or S wave analysis depending on the chosen rupture velocity but the stress drops of deep-focus earthquakes are distinguishable from those of shallow earthquakes.

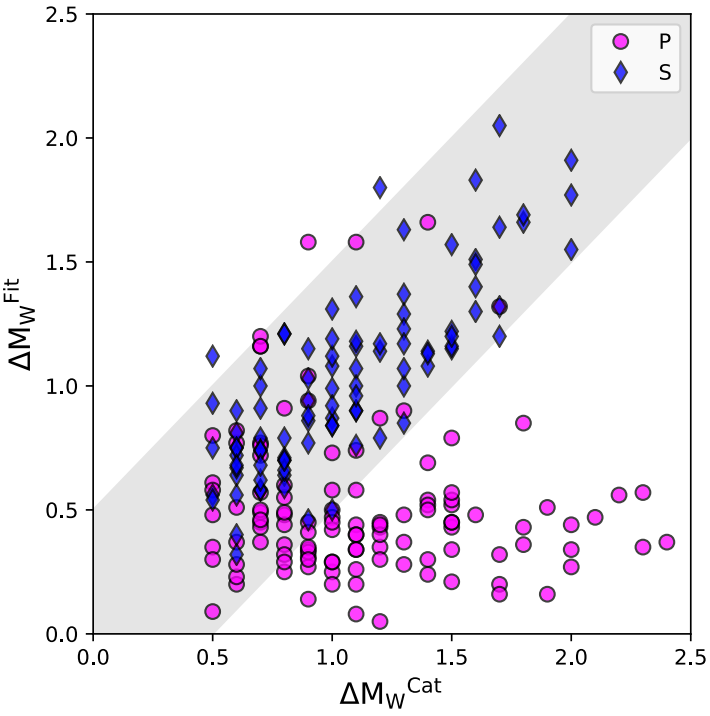

Figure 2.7: Best-fit magnitude difference as a function of catalog magnitude difference of earthquake pairs. Note that one master event can have multiple eGfs. S-wave pairs and P-wave pairs are in blue diamonds and magenta circles, respectively. Shaded area indicates a maximum error of 0.5, out of which earthquake pairs are excluded in our analysis.

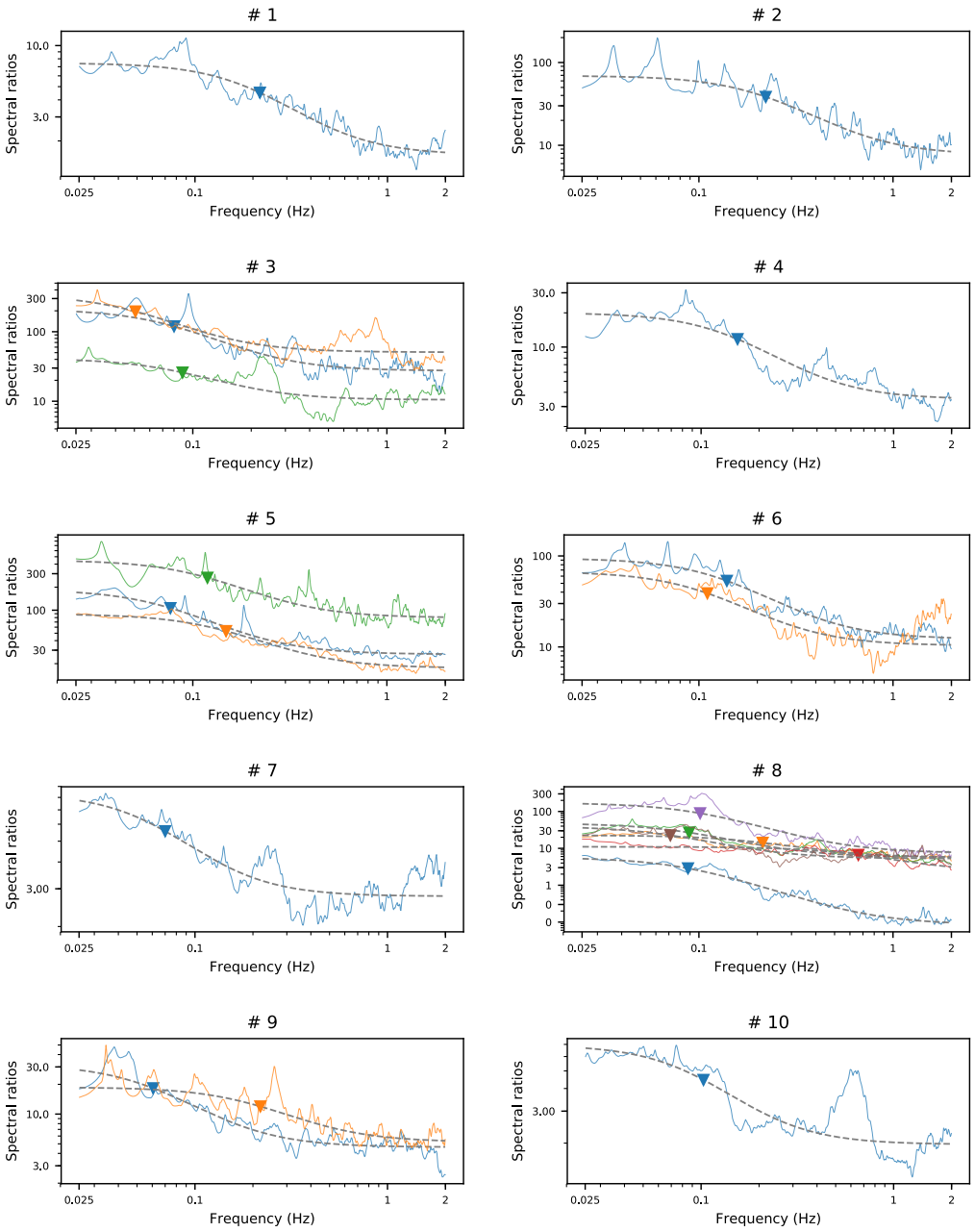

Figure 2.8: Best-fit magnitude difference as a function of catalog magnitude difference of earthquake pairs. Note that one master event can have multiple eGfs. S-wave and P-wave pairs are in blue diamonds and magenta circles, respectively. The shaded area indicates a maximum error of 0.5, out of which earthquake pairs are excluded in our analysis.

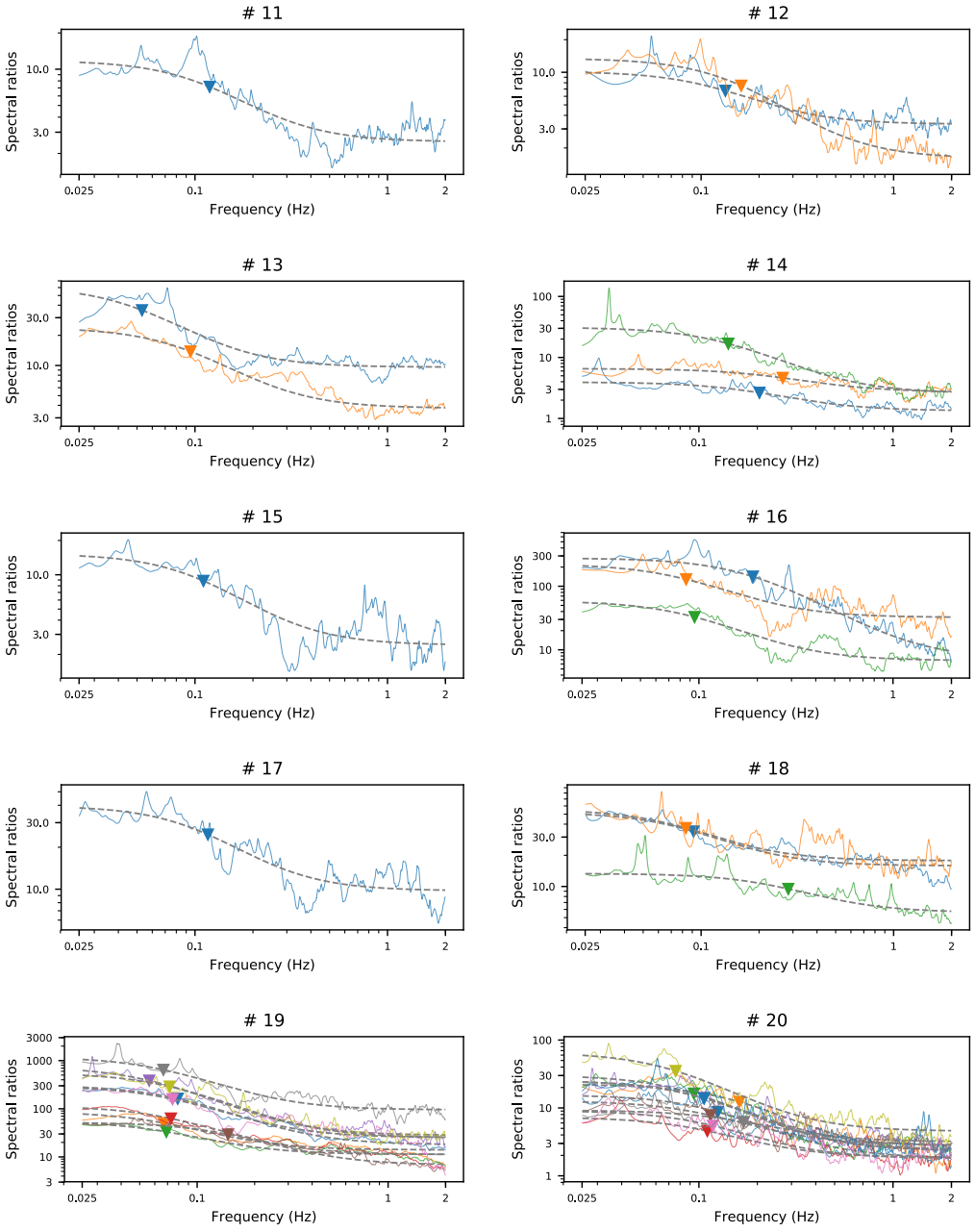
11
12
13
14
15
16
17
18
19
20
Spectral ratios
Frequency (Hz)
0.025
0.1
1
2

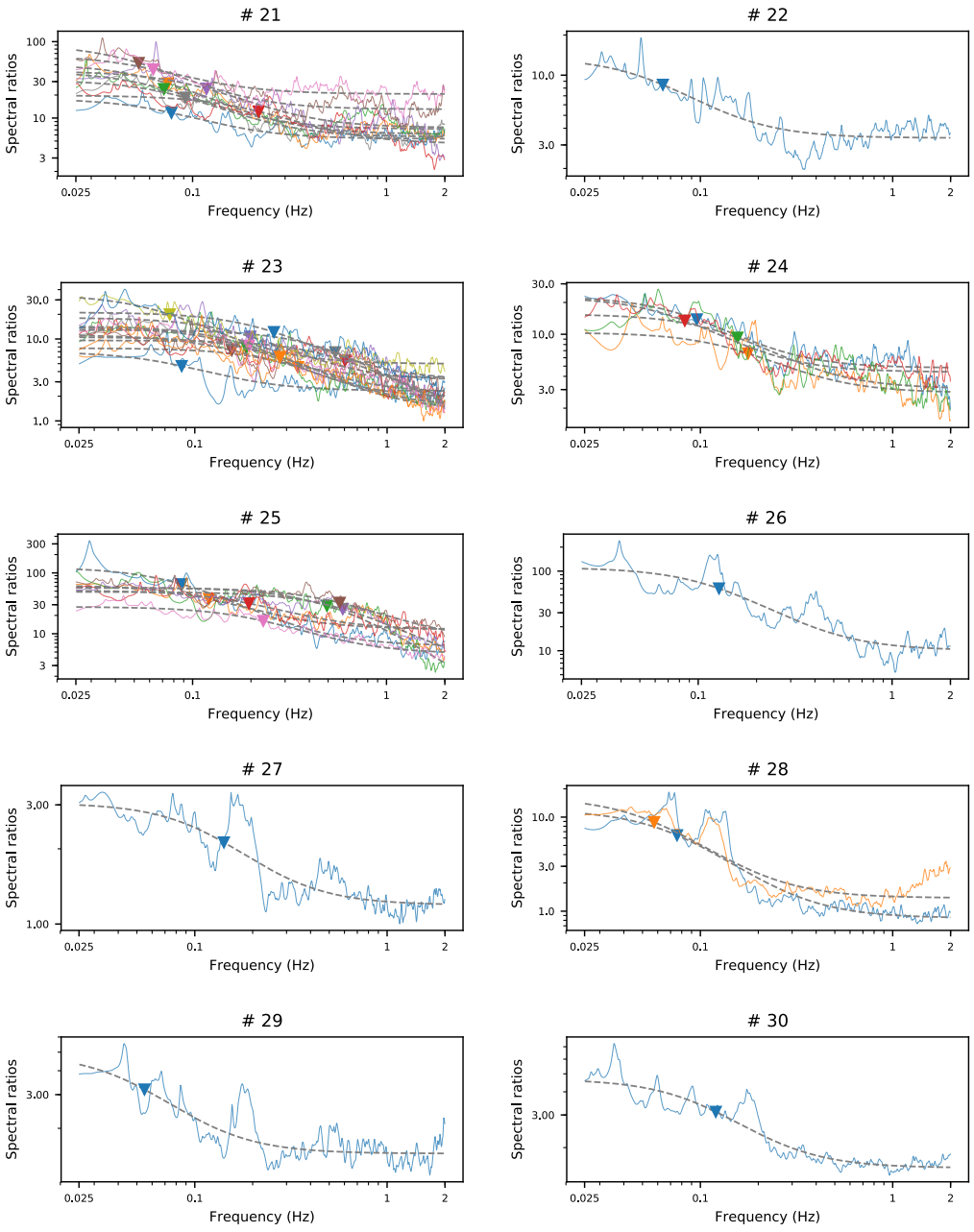
21
Spectral ratios
100
30
10
3
0.025
0.1
1
2
Frequency (Hz)
22
Spectral ratios
10.0
3.0
0.025
0.1
1
2
Frequency (Hz)
23
Spectral ratios
30.0
10.0
3.0
1.0
0.025
0.1
1
2
Frequency (Hz)
24
Spectral ratios
30.0
10.0
3.0
0.025
0.1
1
2
Frequency (Hz)
25
Spectral ratios
300
100
30
10
3
0.025
0.1
1
2
Frequency (Hz)
26
Spectral ratios
100
30
10
0.025
0.1
1
2
Frequency (Hz)
27
Spectral ratios
3.00
1.00
0.025
0.1
1
2
Frequency (Hz)
28
Spectral ratios
10.0
3.0
1.0
0.025
0.1
1
2
Frequency (Hz)
29
Spectral ratios
3.00
0.025
0.1
1
2
Frequency (Hz)
30
Spectral ratios
3.00
0.025
0.1
1
2
Frequency (Hz)

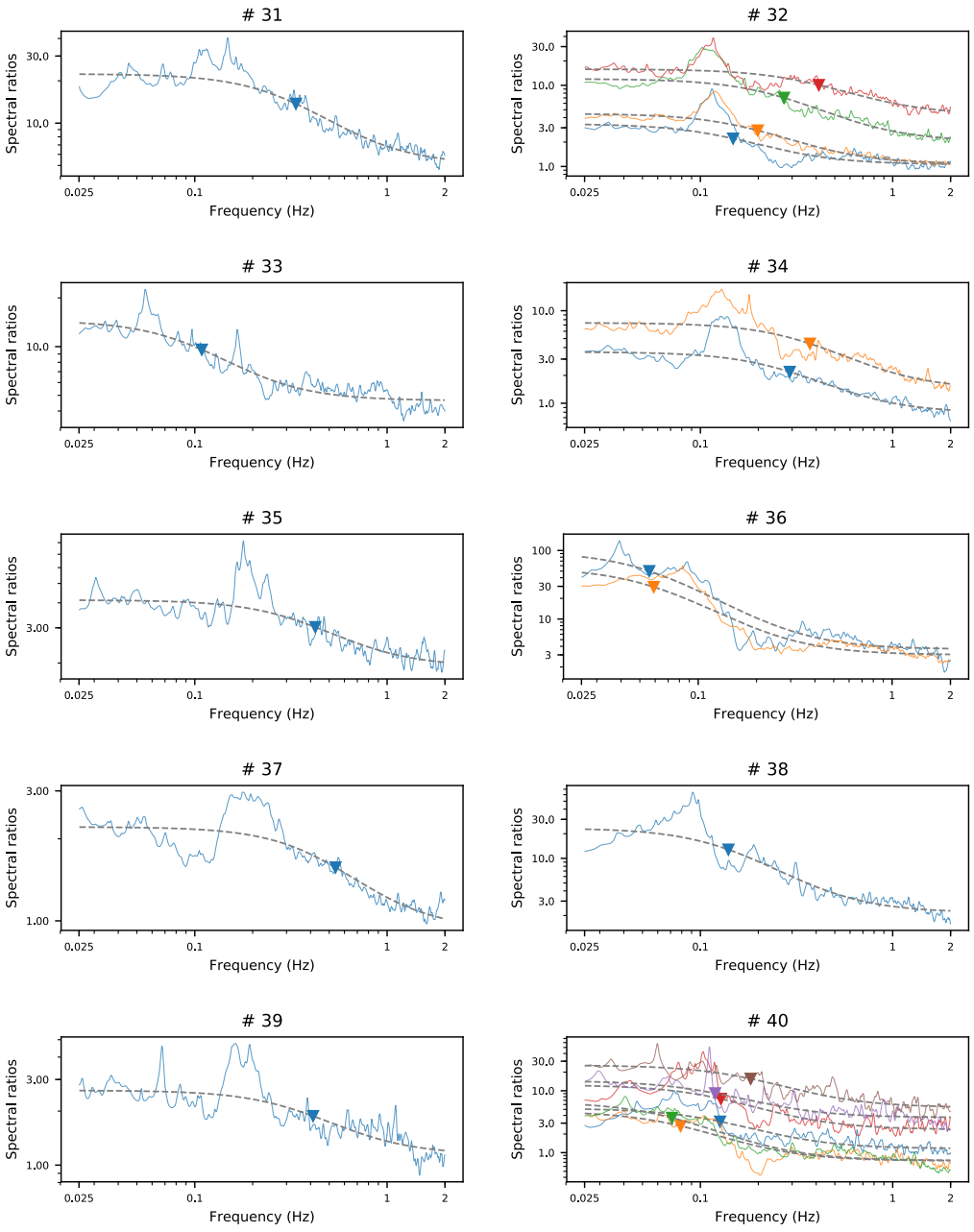
31
32
33
34
35
36
37
38
39
40
Spectral ratios
Frequency (Hz)
0.025
0.1
1
2

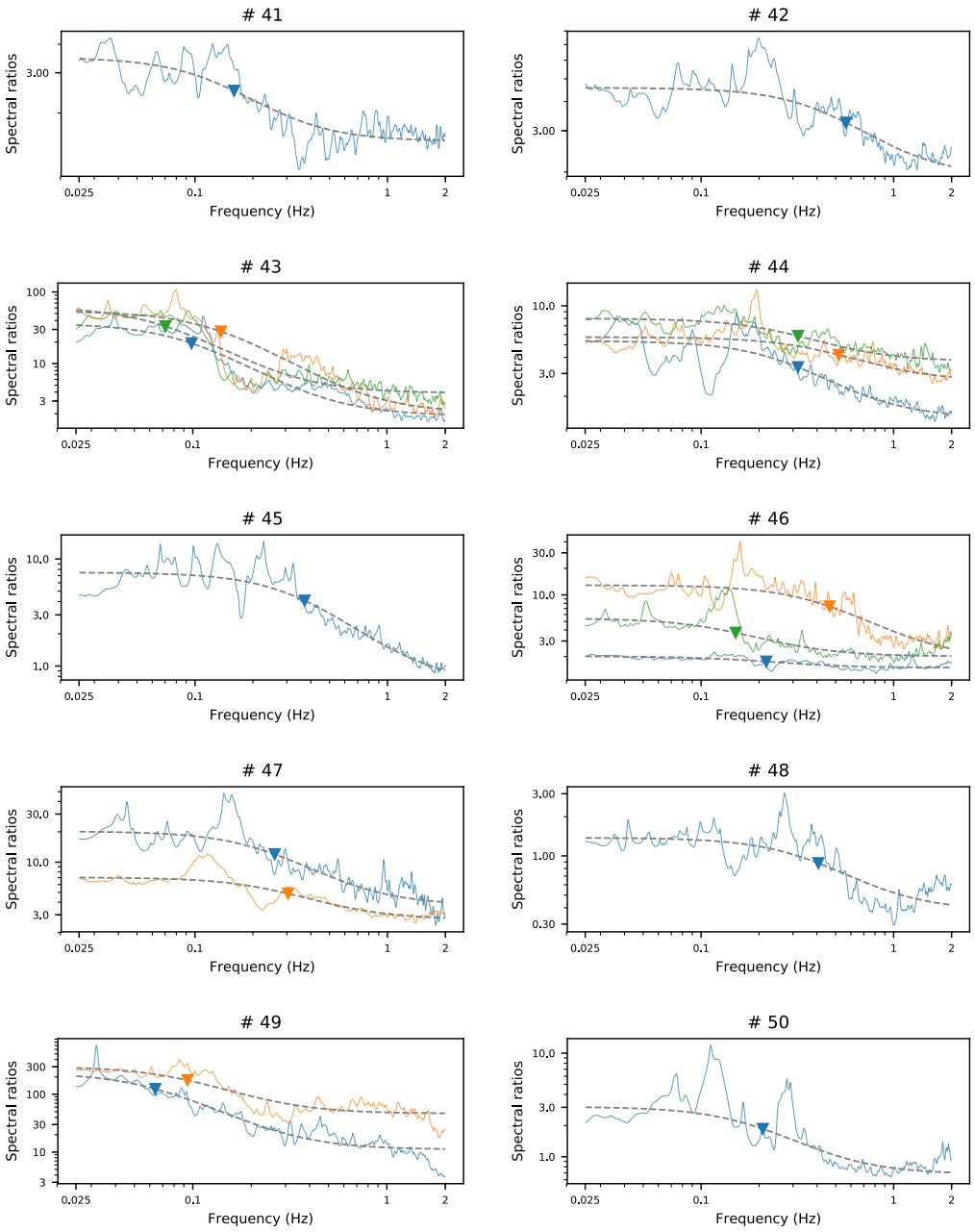
41
42
43
44
45
46
47
48
49
50
Spectral ratios
Frequency (Hz)
0.025
0.1
1
2

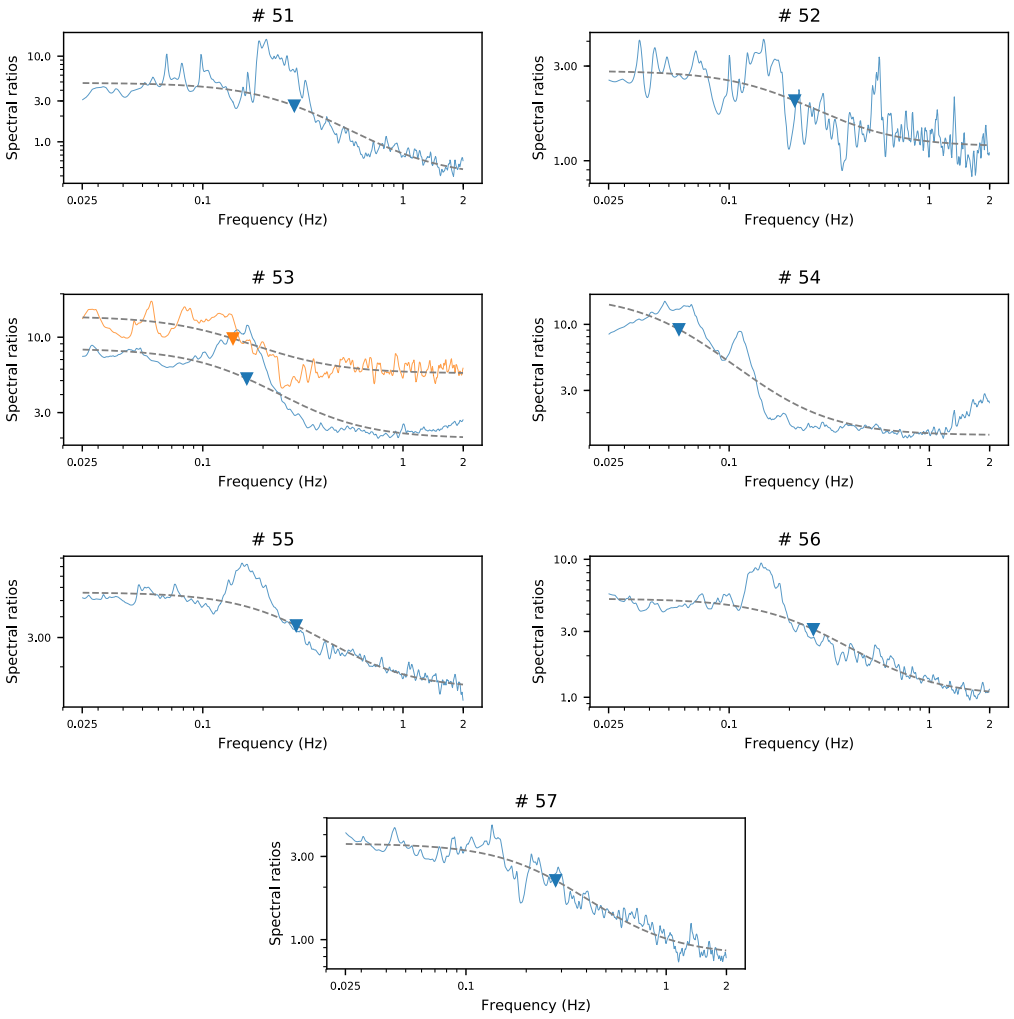
51
Spectral ratios
10.0
3.0
1.0
0.025
0.1
1
2
Frequency (Hz)
52
Spectral ratios
3.00
1.00
0.025
0.1
1
2
Frequency (Hz)
53
Spectral ratios
10.0
3.0
0.025
0.1
1
2
Frequency (Hz)
54
Spectral ratios
10.0
3.0
0.025
0.1
1
2
Frequency (Hz)
55
Spectral ratios
3.00
0.025
0.1
1
2
Frequency (Hz)
56
Spectral ratios
10.0
3.0
1.0
0.025
0.1
1
2
Frequency (Hz)
57
Spectral ratios
3.00
1.00
0.025
0.1
1
2
Frequency (Hz)

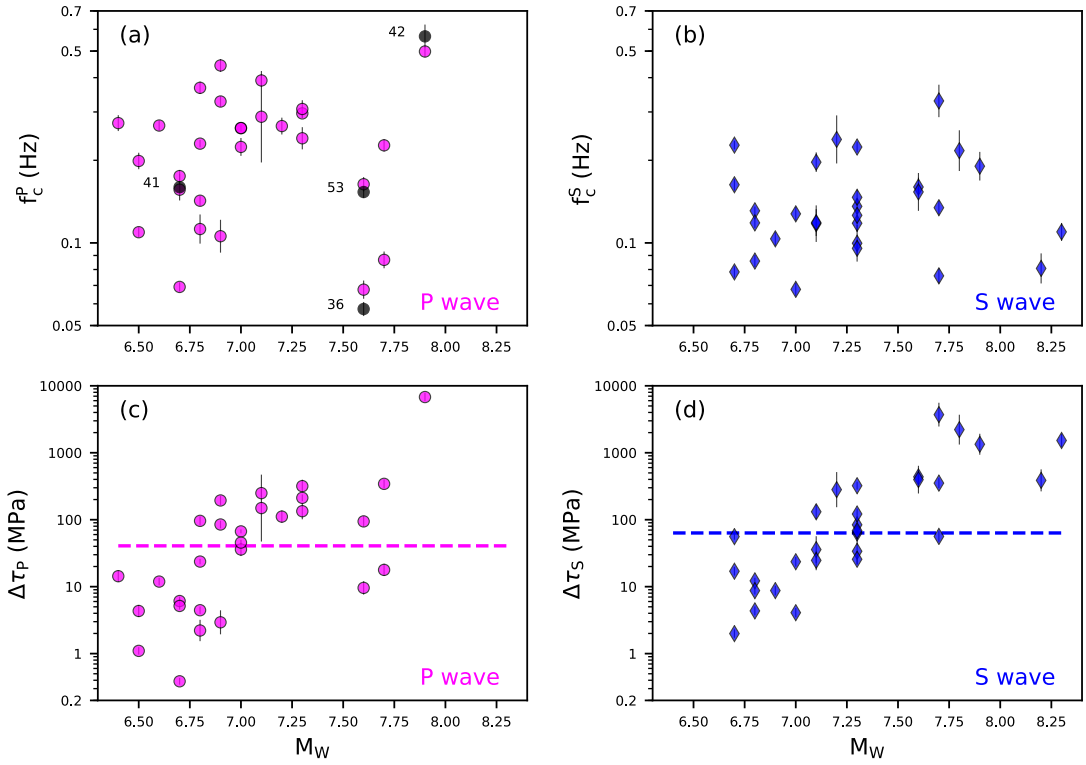

Figure 2.9: Corner frequencies ((a) and (b)) and stress drops ((c) and (d)) of master events as a function of moment magnitudes estimated from P-wave ((a) and (c)) and S-wave spectra using Boatwright's source model. Vertical lines indicate 2σ uncertainties determined by bootstrapping analysis. (a) The numbers to the left of the four data points are the associated event numbers in Table 1. Dashed lines in (c) and (d) indicate medians of P-wave (40.7 MPa) and S-wave (63.4 MPa) stress drop estimates.

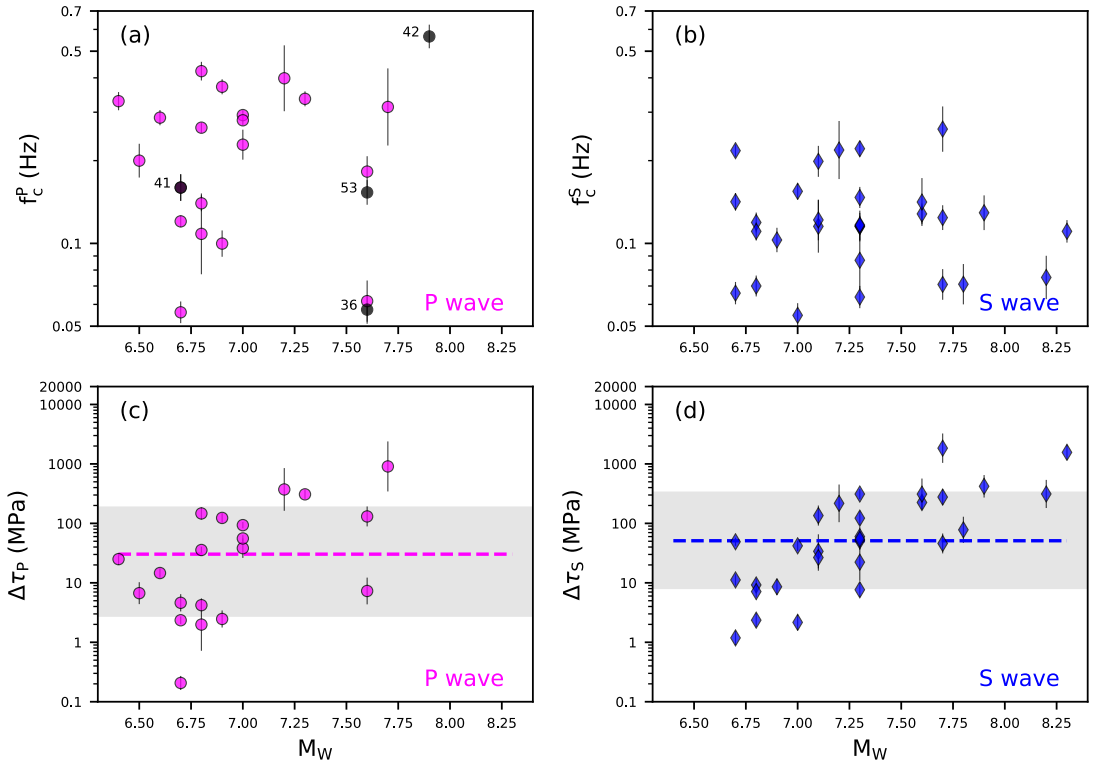

Figure 2.10: Corner frequencies ((a) and (b)) and stress drops ((c) and (d)) of master events as a function of moment magnitudes estimated from P-wave ((a) and (c)) and S-wave spectra when moment ratios are higher than 3.0. In (c) and (d), shaded areas are one-standard-deviation ranges of P-wave (2.8-184.5 MPa) and S-wave (8.2-328.9 MPa) stress drop estimates; dashed lines in (c) and (d) indicate medians of P-wave (30.0 MPa) and S-wave (51.0 MPa) estimates. Compared to Figure 3, there is no change in S-wave results, and changes in P-wave results do not affect our interpretation.

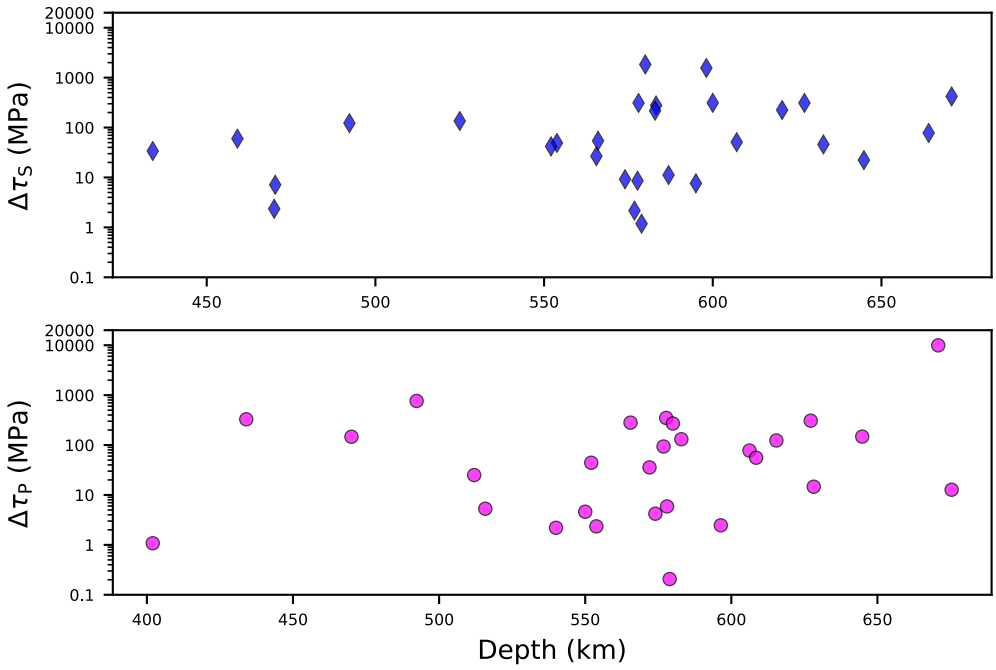

Figure 2.11: Variation of S- (top) and P-wave (bottom) stress drop estimates with depth based on Brune's source model.

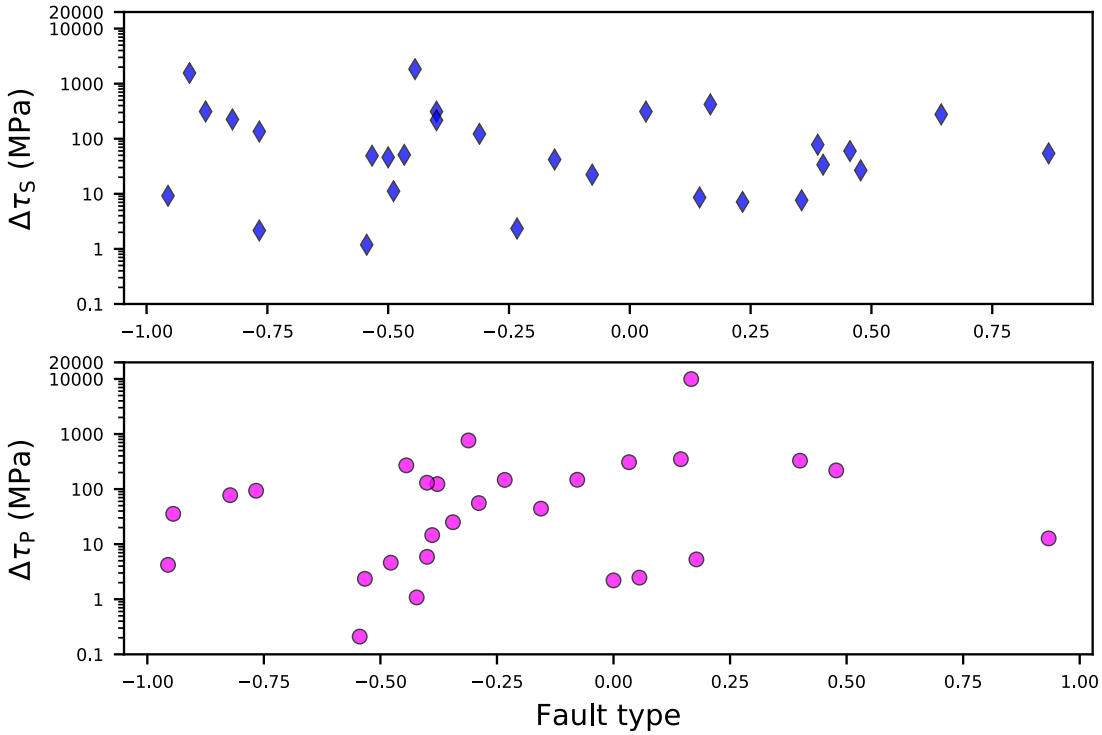

Figure 2.12: Variation of S- (top) and P-wave (bottom) stress drop estimates with focal mechanism. Fault types are parameterized by a scalar value ranging from -1 (normal faulting) to 0 (strike-slip faulting) to 1 (reverse faulting). The scalar value is calculated from the rakes of the two nodal planes.

Table 2.1: Catalog of master events based on S- (Number 1-29) and P-wave (Number 30-57) spectra. f_M and f_{eGf} are corner frequencies using different eGfs and their means. Their uncertainties are 95% intervals from bootstrapping. $\Delta\tau$ show the stress drops computed from averaged corner frequencies based on circular cracks. Locations of master events are indicated by abbreviation following Number in the first column. NP: Northwestern Pacific; FT: Fiji-Tonga; SA: South America

Event Number	Time	Latitude	Longitude	Depth (km)	Mw	f_M (Hz)	f_{eGf} (Hz)	Radius (km)	$\Delta\tau$ (MPa)
1 (NP)	2017-10-24T10:47:47	123.07	-7.22	553.81	6.7	0.217±0.012	0.217±0.012	9.97	49.06
2 (NP)	2017-01-10T06:13:47	122.62	4.48	627.71	7.3	0.221±0.015	0.221±0.015	5.38	311.4
3 (NP)	2015-05-30T11:23:02	140.49	27.84	664.0	7.8	0.071±0.013	0.080±0.008	8.54	77.95
							0.051±0.005		
							0.089±0.009		
4 (NP)	2015-02-27T13:45:05	122.53	-7.30	552.06	7.0	0.155±0.011	0.155±0.011	10.50	41.94
5 (NP)	2013-05-24T05:44:49	153.22	54.89	598.1	8.3	0.111±0.011	0.077±0.004	3.14	1564.0
							0.148±0.007		
							0.119±0.008		
6 (NP)	2012-08-14T02:59:38	145.06	49.8	583.2	7.7	0.124±0.014	0.139±0.008	5.60	277.0
							0.111±0.010		
7 (NP)	2010-11-30T03:24:41	139.19	28.35	470.0	6.8	0.070±0.006	0.070±0.006	27.43	2.35
8 (NP)	2010-07-23T22:51:13	123.48	6.50	578.0	7.6	0.141±0.032	0.088±0.003	5.39	310.8
							0.213±0.013		
							0.089±0.008		
							0.663±0.068		
							0.101±0.008		
							0.071±0.008		
9 (NP)	2010-07-23T22:08:11	123.41	6.72	607.1	7.3	0.115±0.014	0.061±0.004	9.84	51.02
							0.218±0.021		
10 (NP)	2010-02-18T01:13:18	130.70	42.59	577.7	6.9	0.103±0.011	0.103±0.011	17.81	8.59
11 (NP)	2009-10-07T21:41:14	122.37	4.08	574.0	6.8	0.119±0.010	0.119±0.010	17.41	9.21
12 (NP)	2008-11-24T09:03:00	154.32	54.20	492.3	7.3	0.147±0.004	0.134±0.008	7.35	122.5
							0.161±0.011		
13 (NP)	2008-07-05T02:12:06	152.89	53.88	632.8	7.7	0.071±0.010	0.053±0.006	10.18	45.97
							0.095±0.007		
14 (NP)	2005-02-05T12:23:18	123.34	5.30	525.0	7.1	0.199±0.028	0.205±0.020	7.11	135.3
							0.270±0.023		
							0.142±0.005		
15 (NP)	2003-07-27T06:25:31	139.29	47.15	470.3	6.8	0.111±0.009	0.111±0.009	18.96	7.13
16 (NP)	2002-11-17T04:53:55	146.21	47.82	459.1	7.3	0.116±0.016	0.190±0.008	9.33	59.79
							0.086±0.009		
							0.095±0.006		

Event Number	Time	Latitude	Longitude	Depth (km)	Mw	f_M (Hz)	f_{eGf} (Hz)	Radius (km)	$\Delta\tau$ (MPa)
17 (NP)	2002-06-28T17:19:30	130.67	43.75	566.0	7.3	0.117±0.009	0.117±0.009	9.63	54.31
18 (FT)	2018-09-06T15:49:14	179.35	-18.47	670.81	7.9	0.129±0.020	0.091±0.005	4.87	420.16
							0.083±0.010		
							0.284±0.024		
19 (FT)	2018-08-19T00:19:40	-178.15	-18.11	600.0	8.2	0.075±0.015	0.079±0.002	5.38	312.5
							0.067±0.006		
							0.069±0.005		
							0.073±0.004		
							0.056±0.004		
							0.145±0.006		
							0.074±0.006		
							0.067±0.004		
							0.072±0.004		
20 (FT)	2014-11-01T18:57:22	-177.76	-19.69	434.0	7.1	0.115±0.028	0.125±0.007	11.28	33.82
							0.162±0.011		
							0.094±0.005		
							0.110±0.010		
							0.106±0.006		
							0.115±0.008		
							0.118±0.011		
							0.170±0.017		
							0.076±0.002		
							0.107±0.005		
21 (FT)	2011-09-15T19:31:03	-179.53	-21.61	644.8	7.3	0.087±0.024	0.078±0.006	12.97	22.28
							0.075±0.005		
							0.071±0.005		
							0.219±0.021		
							0.118±0.009		
							0.053±0.006		
							0.063±0.007		
							0.092±0.008		
22 (FT)	2009-11-09T10:44:54	178.33	-17.24	595.0	7.3	0.064±0.006	0.064±0.006	18.52	7.64

Event Number	Time	Latitude	Longitude	Depth (km)	Mw	f_M (Hz)	f_{eGf} (Hz)	Radius (km)	$\Delta\tau$ (MPa)
23 (FT)	2006-01-02T22:13:40	-178.18	-19.93	582.9	7.2	0.219±0.060	0.085±0.009	6.07	217.1
							0.343±0.032		
							0.186±0.012		
							0.604±0.046		
							0.195±0.016		
							0.156±0.012		
							0.191±0.013		
							0.537±0.036		
							0.074±0.004		
							0.258±0.020		
							0.277±0.014		
24 (FT)	2004-07-15T04:27:13	-178.76	-17.66	565.5	7.1	0.122±0.023	0.096±0.006	12.21	26.66
							0.177±0.020		
							0.156±0.016		
							0.083±0.005		
25 (FT)	2002-08-19T11:01:02	-179.51	-21.70	580.0	7.7	0.260±0.054	0.088±0.005	2.98	1840.0
							0.121±0.011		
							0.493±0.027		
							0.195±0.019		
							0.595±0.038		
							0.574±0.049		
							0.231±0.011		
26 (SA)	2015-11-24T22:50:54	-71.02	-10.06	620.56	7.6	0.128±0.012	0.128±0.012	6.00	224.59
27 (SA)	2012-05-28T05:07:23	-63.09	-28.04	586.9	6.7	0.142±0.011	0.142±0.011	16.31	11.19
28 (SA)	2011-09-02T13:47:10	-63.03	-28.40	578.9	6.7	0.066±0.006	0.076±0.005	34.48	1.19
							0.057±0.004		
29 (SA)	2011-01-01T09:56:58	-63.14	-26.80	576.8	7.0	0.055±0.006	0.055±0.006	28.21	2.16
30 (NP)	2017-10-24T10:47:47	123.07	-7.22	553.81	6.7	0.120±0.006	0.120±0.006	14.15	2.35
31 (NP)	2017-01-10T06:13:47	122.62	4.48	627.17	7.3	0.336±0.022	0.336±0.022	5.22	307.8

Event Number	Time	Latitude	Longitude	Depth (km)	Mw	f_M (Hz)	f_{eGf} (Hz)	Radius (km)	$\Delta\tau$ (MPa)
32 (NP)	2015-02-27T13:45:05	122.54	-7.30	552.06	7.0	0.240±0.029	0.148±0.012	7.09	44.20
							0.200±0.008		
							0.272±0.013		
							0.413±0.026		
33 (NP)	2013-09-04T00:18:24	138.83	29.94	402.0	6.5	0.109±0.007	0.109±0.007	14.36	1.08
34 (NP)	2011-01-12T21:32:54	139.88	26.97	512.0	6.4	0.329±0.026	0.292±0.014	5.05	25.04
							0.371±0.023		
35 (NP)	2010-11-30T03:24:41	139.19	28.35	470.0	6.8	0.423±0.034	0.423±0.034	3.84	146.8
36 (NP)	2010-07-23T22:51:13	123.48	6.50	578.0	7.6	0.057±0.007	0.056±0.005	30.01	5.89
							0.059±0.005		
37 (NP)	2010-02-18T01:13:18	130.70	42.59	577.7	6.9	0.539±0.059	0.539±0.059	3.20	349.4
38 (NP)	2009-10-07T21:41:14	122.37	4.08	574.0	6.8	0.140±0.010	0.140±0.010	12.30	4.21
39 (NP)	2008-11-24T09:03:00	154.32	54.20	492.3	7.3	0.412±0.042	0.412±0.042	3.99	764.0
40 (FT)	2018-11-18T20:25:45	-178.93	-17.87	540.0	6.8	0.112±0.026	0.127±0.013	15.07	2.20
							0.079±0.006		
							0.071±0.007		
							0.128±0.012		
							0.119±0.010		
							0.183±0.014		
41 (FT)	2018-09-30T10:52:24	-178.06	-18.36	550.0	6.7	0.160±0.019	0.160±0.019	10.64	4.61
42 (FT)	2018-09-06T15:49:14	-179.35	-18.47	670.81	7.9	0.566±0.059	0.566±0.059	3.35	9945.5
43 (FT)	2016-09-24T21:28:41	-178.24	-19.78	596.4	6.9	0.100±0.012	0.099±0.006	17.44	2.47
							0.140±0.008		
							0.072±0.005		
44 (FT)	2014-11-01T18:57:22	-177.76	-19.69	434.0	7.1	0.375±0.062	0.319±0.028	4.25	328.4
							0.519±0.049		
							0.319±0.029		
45 (FT)	2014-07-21T14:54:41	-178.40	-19.80	615.42	6.9	0.371±0.024	0.371±0.024	4.71	123.48

Event Number	Time	Latitude	Longitude	Depth (km)	Mw	f_M (Hz)	f_{eGf} (Hz)	Radius (km)	$\Delta\tau$ (MPa)
46 (FT)	2011-09-15T19:31:03	-179.53	-21.61	644.8	7.3	0.249±0.043	0.218±0.023	7.06	147.8
							0.465±0.043		
							0.151±0.013		
47 (FT)	2006-01-02T22:13:40	-178.18	-19.93	582.9	7.2	0.281±0.030	0.260±0.018	6.15	130.66
							0.305±0.024		
48 (FT)	2004-07-15T04:27:13	-178.76	-17.66	565.5	7.1	0.407±0.047	0.407±0.047	4.21	281.3
49 (FT)	2002-08-19T11:08:22	178.50	-23.88	675.4	7.7	0.078±0.010	0.064±0.004	24.46	12.73
							0.094±0.011		
50 (FT)	2002-08-19T11:01:02	-179.51	-21.70	580.0	7.7	0.209±0.018	0.209±0.018	8.24	270.1
51 (FT)	2000-12-18T01:19:21	-179.12	-21.18	628.2	6.6	0.287±0.019	0.287±0.019	6.11	14.61
52 (FT)	2000-05-04T20:36:29	-178.52	-17.91	515.8	6.5	0.213±0.022	0.213±0.022	7.84	5.29
53 (SA)	2015-11-24T22:45:38	-70.94	-10.54	606.21	7.6	0.153±0.017	0.166±0.009	11.39	77.54
							0.142±0.013		
54 (SA)	2011-09-02T13:47:10	-63.03	-28.40	578.9	6.7	0.056±0.005	0.056±0.005	30.71	0.21
55 (SA)	2011-01-01T09:56:58	-63.14	-26.80	576.8	7.0	0.293±0.012	0.293±0.012	5.88	93.42
56 (SA)	2006-11-13T01:26:36	-63.28	-26.05	572.0	6.8	0.264±0.012	0.264±0.012	6.52	35.55
57 (SA)	2000-04-23T09:27:23	-62.99	-28.31	608.5	7.0	0.280±0.012	0.280±0.012	6.23	55.76

CHAPTER 3

Characterizing Multisubevent Earthquakes Using the Brune Source Model *

Abstract

Although the Brune source model describes earthquake moment release as a single pulse, it is widely used in studies of complex earthquakes with multiple episodes of high moment release (i.e., multiple subevents). In this study, we investigate how corner frequency estimates of earthquakes with multiple subevents are biased if they are based on the Brune source model. By assuming complex sources as a sum of multiple Brune sources, we analyze 1640 source time functions of Mw 5.5–8.0 earthquakes in the seismic source characteristic retrieved from deconvolving teleseismic body waves catalog to estimate the corner frequencies, onset times, and seismic moments of subevents. We identify more subevents for strike-slip earthquakes than dip-slip earthquakes, and the number of resolvable subevents increases with magnitude. We find that earthquake corner frequency correlates best with the corner frequency of the subevent with the highest moment release (i.e., the largest subsevent). This suggests that, when the Brune model is used, the estimated corner frequency and, therefore, the stress drop of a complex earthquake is determined primarily by the largest subevent rather than the total rupture area. Our results imply that, in addition to the simplified assumption of a radial rupture area with a constant rupture velocity, the stress variation of asperities, rather than the average stress change of the whole fault, contributes to the large variance of stress-drop estimates.

*Chapter 3 is published in *Bulletin of the Seismological Society of America*: Liu, Meichen, Yihe Huang, and Jeroen Ritsema. "Characterizing Multisubevent Earthquakes Using the Brune Source Model." Bulletin of the Seismological Society of America 113, no. 2 (2023): 577-591.

3.1 Introduction

The classical earthquake source model proposed by J. Brune more than five decades ago (*Brune*, 1970) is still broadly used to understand the propagation of a fault rupture and the radiation of seismic energy. In the Brune model, a circular crack instantaneously experiences a shear dislocation due to a constant stress drop (i.e., the change of stress) on the fault. The Brune model links three key elements of an earthquake: the seismic moment, corner frequency, and stress drop with simple functions in which the seismic moment and corner frequency are the two free parameters. The Brune model predicts that the source spectrum is constant at frequencies lower than the corner frequency, and decays proportional to the square of frequency at frequencies higher than the corner frequency, an important feature for the calculation of high-frequency ground motions for engineering applications (*Papageorgiou and Aki*, 1983; *Purvance and Anderson*, 2003; *Sotiriadis et al.*, 2021). Numerous studies of small and large, shallow and deep, and tectonic and induced earthquakes using regional and teleseismic data are based on the Brune source model when estimating stress drops (e.g., *Abercrombie*, 1995; *García et al.*, 2004; *Allmann and Shearer*, 2009; *Baltay et al.*, 2011; *Oth*, 2013; *Chen and Shearer*, 2011; *Huang et al.*, 2016; *Prieto et al.*, 2017; *Ruhl et al.*, 2017; *Trugman et al.*, 2017; *Wu et al.*, 2018; *Shearer et al.*, 2019; *Liu et al.*, 2020; *Yu et al.*, 2020).

Nevertheless, it is well recognized that earthquakes are complex on a wide variety of spatial and temporal scales. The barrier (*Das and Aki*, 1977) and asperity (*Lay and Kanamori*, 1981; *Lay et al.*, 1982) models describe stress and frictional differences on the fault plane. The rupture velocity and the moment rate during rupture expansion can change due to dynamic waves in fault damage zones (e.g., *Huang and Ampuero*, 2011) as well as fault curvature and segmentation (e.g., *Ando and Kaneko*, 2018; *Ulrich et al.*, 2019). The complexity of rupture processes is not only evident for Mw >7 earthquakes (e.g., *Ye et al.*, 2016; *Hayes*, 2017), but also for smaller earthquakes (e.g., *Boatwright*, 1984). Using local seismic arrays, moment rate fluctuations have been observed for Mw <3.5 earthquakes in the Charlevoix, Quebec, seismic zone (*Li et al.*, 1995; *Fischer*, 2005), on the San Andreas fault (*Abercrombie*, 2014; *Wang et al.*, 2014; *Abercrombie et al.*, 2020), and in the 2008 Mogul, Nevada, swarm (*Ruhl et al.*, 2017). *Danré et al.* (2019) used the Gaussian source model to systematically analyze the source complexity for seismic source characteristics retrieved from deconvolving teleseismic body waves (SCARDEC) source time function (STFs; *Vallée and Douet* (2016). They observed increasing source complexity with earthquake magnitude and an important scaling of the moment of subevent with the earthquake moment by a factor of 0.8. For the Brune source model, the source complexity may cause

earthquake source spectra to deviate from the frequency-squared spectral decay for moderate to large (e.g., *Luco*, 1985; *Atkinson*, 1993; *Beresnev and Atkinson*, 2001; *Denolle*, 2019; *Yin et al.*, 2021) and small earthquakes (e.g., *Uchide and Imanishi*, 2016). The Brune source model has also been modified to include two corner frequencies to explain the deviation (*Archuleta and Ji*, 2016; *Denolle and Shearer*, 2016; *Uchide and Imanishi*, 2016; *Ji and Archuleta*, 2021).

For many earthquakes, however, there are insufficient data to model source complexity. It is also not a common practice to use complex source models to predict earthquake ground motions. Therefore, the Brune source model is still frequently used to estimate source parameters and ground motions regardless of earthquake source complexity. This poses a fundamental question: What is measured by the Brune source model when it is applied to complex earthquakes?

Here, we investigate what kind of source properties are represented by the Brune source model for earthquakes with multiple episodes of high moment release (i.e., multiple subevents). We first quantify earthquake source complexity by analyzing the number and source properties of subevents in STFs of hundreds of Mw 5.5–8.0 earthquakes in the SCARDEC catalog (*Vallée and Douet*, 2016). We describe and decompose the STF as a sum of Brune sources, and estimate corner frequencies and seismic moments of subevents. By comparing measured source complexity to that observed by *Danré et al.* (2019), we further understand the scaling relationship between the source complexity and the subevent moment. We also derive the theoretical source spectrum of a complex earthquake with two Brune subevents. Using both SCARDEC analysis and theoretical derivation, we compare the earthquake's overall corner frequency to the corner frequencies of individual subevents and show how earthquake corner frequency and stress drop depend on the temporal spacing and relative moments of subevents.

3.2 STF Decomposition

In the time domain, the Brune source is defined as

$$\Omega(t, t_0, f_c, M_0) = M_0(2\pi f_c)^2(t - t_0)\exp -2\pi f_c(t - t_0)H(t - t_0) \tag{3.1}$$

in which $H(t - t_0)$ is the Heaviside function, t_0 is the onset time of the rupture, M_0 is the seismic moment, and f_c is the corner frequency that is scaled to a characteristic rupture

time $1/f_c$. The Brune model predicts a far-field spectrum:

$$\Omega(f, f_c, M_0) = \frac{M_0}{1 + \frac{f^2}{f_c^2}} \tag{3.2}$$

which has a plateau at frequencies much lower than f_c and decreases proportional to f^2 at frequencies higher than f_c. The stress drop $\Delta\tau$ is proportional to f_c^3 (*Madariaga*, 1976).

We call the Brune source that best matches the STF of an earthquake Ω_{STF}. The seismic moment and corner frequency of Ω_{STF} are M_{STF} and f_{STF}, respectively. To determine M_{STF} and f_{STF} we transform the SCARDEC STF to the frequency domain using a fast Fourier transform algorithm (*Cooley and Tukey*, 1965) and estimate f_{STF} in the frequency range of 0.01–2.0 Hz using the trust-region-reflective least-squares algorithm (*Branch et al.*, 1999). For a complex STF with multiple maxima, M_{STF} approximates the earthquake's integratedmoment rate, and f_{STF} represents an average value of the rupture duration.

To model a complex STF with multiple episodes of high moment rate (i.e., multiple subevents), we write the STF as a sum of Brune pulses:

$$\Omega_{sum}(t) = \sum_{N=1}^{N_{ev}} \Omega_N(t, t_N, f_N, M_N) \tag{3.3}$$

To determine the number of resolvable Brune pulses in Ω_{sum}, we follow the iterative approach by *Danré et al.* (2019) with some modifications (Fig. 3.1). There are three essential steps: (1) To determine subevent N, find the time t_{MAX} of the N local maximum in the STF that is larger than 10% of the STF's maximum value to avoid overfitting small oscillations as individual subevents. Then we find the time t_{MIN} of the first local minimum in the STF more than 0.5 s after t_{MAX}, to avoid overfitting oscillations close to each other as individual subevents. This requirement should not affect the number of subevents because 0.5 s is only about 10% and 1% of the rupture duration of Mw 5.5 and 8 earthquakes. (2) Find the seismic moment M_N and corner frequency f_N of subevent N that minimize the least-squares difference between the STF and $\Omega_{sum} = \sum_{k=1}^{N} \Omega_k(t, t_k, f_k, M_k)$ in the time range $[0, t_{MIN}]$. (3) Repeat steps (1) and (2) gradually adding subevents to Ω_{sum} until the last subevent N_{ev}. We normalized the STFs such that the total integrated area is 1.0 and calculated the residual curve between the STF and Ω_{sum}. We then calculated the integrated area of the residual curve to obtain the misfit. We discard STFs if the misfit is larger than 0.5. Analogous to the estimate of M_{STF} and f_{STF}, we define M_{sum} and f_{sum} as the seismic moment and corner frequency of a single Brune pulse that best matches Ω_{sum} in a least-

squares sense.

3.3 Method: Deriving STF Using Two Brune Pulses

We derive for the first time the STFs and source spectra of earthquakes with multiple subevents whose spectra are described by the Brune model. We focus on earthquakes with two subevents. As shown in the Analysis of SCARDEC STFs section, two-subevents earthquakes account for 43% of the SCARDEC data set. The expression of STFs can also be extended to earthquakes with three or more subevents. We write the STF of an earthquake with two subevents as

$$\Omega_{sum}(t) = \Omega_L(t, t_L, f_L, M_L) + \Omega_S(t, t_S, f_S, M_S) \tag{3.4}$$

in which the parameters t_L, f_L, and M_L and the parameters t_S, f_S, and M_S are the onset times, corner frequencies, and seismic moments of the large and small subevents Ω_L and Ω_S, respectively. The power spectrum of Ω_{sum} for two pulses is

$$\Omega^2_{sum}(f) = \frac{M_L^2}{k_L^2} + \frac{M_S^2}{k_S^2} + \frac{2M_S M_L}{k_S k_L} cos2\pi f(t_L - t_S) + \alpha_L - \alpha_S \tag{3.5}$$

in which $k_L = 1 + f^2/f_L^2$, $k_S = 1 + f^2/f_S^2$, $sin^2\alpha_L = (k_L - 1)/k_L$, and $sin^2\alpha_S = (k_S - 1)/k_S$. The first and second terms in equation (5) are Brune spectra with different low-frequency plateaus and corner frequencies that determine the onset of the spectral fall-off. The third term represents oscillations in the spectrum with periods determined by T and the phase shifts determined by f_L and f_S. We reduce the number of free parameters to four by considering the moment ratio $M = M_L/M_S$ and the onset time difference $T =_L - t_S$ of the largest and smallest subevents instead of M_L, M_S, t_L, and t_S individually.

Fig. 3.2 illustrates the typical form of Ω_{sum} in the time (Fig. 2a) and frequency (Fig. 2b) domains. Ω_{sum} has two subevents with corner frequencies $f_L = 0.15$ Hz and $f_S = 0.40$ Hz and a moment ratio $M = 3$. We consider $T = -2$ s and $T = +2$ s for which the large subevent precedes and succeeds the small subevent by two seconds,

respectively (Fig. 2a). The order of the small and the large subevent can significantly change the shape of the STF and its peak values. For example, when $T = -2$ s, the two maxima in the STF are similar, but for $T = +2$ s, the second maximum is 60% higher than the first one. The spectra for $T = -2$ s and $T = +2$ s have local minima at different frequencies, and they converge and decay approximately proportional to f^2 at frequencies higher than about 0.5 Hz (Fig. 2b). The Brune pulse that optimally fits Ω_{sum} has a corner

frequency $f_{sum} = 0.19$ Hz for both $T = -2$ s and $T = +2$ s, about two times lower than f_S. The location of the first spectral minimum and the spectral decay at high frequencies depend on the values of f_L, f_S, M, and T.

Fig. 3.3a shows how f_{sum} varies as a function of T and M for ranges we resolve for the majority of STFs in the SCARDEC catalog with two subevents. As in Fig 3.2, f_L is 0.15 Hz and f_S is 0.40 Hz. For high values of M, f_{sum} approaches f_L because the largest of the two subevents dominates Ω_{sum}. For values of M near 1 and for T near 0, f_{sum} is intermediate between f_L and f_S. The asymmetry of f_{sum} about $T = 0$ indicates that f_{sum} depends on the order of the large and small subevents in the STF, especially when the onset time difference between the subevents is small. The asymmetry originates from a phase shift of $2(\alpha_L - \alpha_S)$ when the sign of T changes (see equation 5), which is the strongest when M is high. Fig. 3.3b shows how f_{sum} varies with subevent corner frequencies f L and f_S. We find that f_{sum} is more related to f_L than f_S when $M = 3$ and $T = 2$. f_{sum} is closer to the smaller one of f_L and f_S and increases with either of them.

3.4 Analysis of SCARDEC STFs

The SCARDEC catalog with source information of hundreds of earthquakes facilitates our exploration. Although it does not include constraints on fault slip distribution such as the finite-fault modeling databases developed by *Ye et al.* (2016) and *Hayes* (2017), it is an order of magnitude larger. The SCARDEC analysis is based on the analysis of the waveforms of the teleseismic body-wave phases P, PcP, PP, ScS, and SH and their surface reflected phases to maximize the range of wave take-off angles in the analysis and thus resolution. There are no simplifications regarding the spatial–temporal complexity of the rupture process, so differences of the STFs at different stations may capture rupture directivity. However, we use the average of the STFs from all stations as an estimate of the overall time dependence of moment rate. The SCARDEC catalog has been used in determining the variations of strain drop, stress drop, and radiated energy with depth, magnitude, and tectonic settings (*Vallée*, 2013; *Courboulex et al.*, 2016; *Chounet et al.*, 2018; *Denolle*, 2019; *Yin et al.*, 2021), as well as inversions for rupture velocity and rupture direction (*Chounet et al.*, 2018).

We decompose STFs of Mw 5.5–8.0 earthquakes between 1992 and 2017 in the SCARDEC catalog. Out of 3348 earthquakes, 1640 earthquakes (49%) have two or more subevents. *Danré et al.* (2019) identified a higher percentage of earthquakes with multiple subevents (81%) most likely because the Gaussian model describes the source with three free parameters in contrast to the two free parameters in the Brune model. Nevertheless, both studies

indicate that at least half of moderate-to-large earthquakes are complex.

As an example, Fig. 3.4a and 3.4c shows the reconstructed STFs (i.e., Ω_{sum}) and the original STFs of the 8 December 2017 Mw 6.2 earthquake in Caroline Islands and of the 25 December 2016 Mw 7.6 earthquake in southern Chile. Fig. 3.4b and 3.4d shows their spectra Ω_{STF} and Ω_{sum}. For the Caroline Islands earthquake, we determine that Ω_{sum} is a sum of two Brune sources with a moment ratio of 5.75 and with corner frequencies of 0.13 Hz (f_L) and 0.30 Hz (f_S). The large subevent occurred 2.3 s after the small subevent. The misfit between the normalized STF and Ω_{sum} is 32.8%. The corner frequency is inferred to be 0.11 Hz, slightly lower than f_L, because the largest subevent represents more than 85% of the total moment. The observed and synthetic STFs release 90% of the total moment at 6.6 and 7.8 s. The southern Chile earthquake is also decomposed into two Brune sources although it has a longer source duration. For this event, the onset time difference $T = +6.82$ s, and the moment ratio $M = 1.08$ with a misfit of 18.7%. The corner frequencies f_L and f_S are both 0.048 Hz and much larger than the inferred earthquake corner frequency (0.028 Hz) because the two subevents have similar moments. The observed and synthetic STFs release 90% of the total moment at 17.0 and 19.3 s, respectively. The synthetic source duration is larger than the observed source duration because the fixed Brune STF decreases more slowly than the observed STF. Compared to Fig. 3.4d, spectra in Fig. 3.4b have an extra plateau at 0.2–0.3 Hz because of the large difference between f_L and f_S.

Fig. 3.5 summarizes how the number of subevents varies with moment magnitude, focal mechanism, and source depth. It suggests that the number of subevents increases with moment magnitude in the range of 5.5–8.0 (Fig. 5a) and that strike-slip earthquakes are more complex than dip-slip earthquakes (Fig. 5b). Earthquakes that have eight or more subevents are all strike-slip earthquakes. This is in agreement with the previous study by *Danré et al.* (2019), indicating that the correlation of source complexity with magnitude and faulting type, as quantified by the number of subevents, is a robust characteristic of the SCARDEC catalog and weakly influenced by the assumed source model for the subevent. We also find that shallow (<50 km) and very deep (>600 km) earthquakes have more subevents than earthquakes between 50 and 600 km depth (Fig. 5c). Patterns in Fig. 3.5b and 3.5c are also observed in *Yin et al.* (2021).

3.5 SCARDEC STFs With Two Subevents

From the 1640 multisubevent STFs in the SCARDEC catalog, 714 STFs (43%) have two subevents, more than the sum of the number of earthquakes with three (361), four (198), and five (104) subevents. Because two-subevent earthquakes are most common and the

simplest scenario of complex earthquakes, our analysis focuses on earthquakes with two subevents.

The magnitude range of two-subevent earthquakes is Mw 5.7–8.0. The ratio M is lower than 8 for about 75% of the STFs (Fig. 6a) and the absolute onset time difference T is between 2.0 and 8.0 s for about 80% of the STFs (Fig. 6b). T is negative for 521 STFs, suggesting that if small subevents before and after larger ones are equally detectable the largest subevent precedes the smallest subevent more often. The corner frequency f_L of the large subevent has a median value of 0.14 Hz, higher than the corner frequency f_S of the small subevent that has a median of 0.21 Hz (Fig. 6c), consistent with the common observation that smaller events have higher corner frequencies. $f_L = f_S$ has a median of 0.65 (Fig. 6d), with 76% of values smaller than 1.0, which is consistent with the common observation that smaller events tend to have higher corner frequencies.

In Fig. 3.7, we evaluate the significance of the corner frequency f_{STF} of the 714 SCARDEC STFs that are decomposed to have two subevents. The correlation between f_{STF} and f_L (Fig. 7b,d) is higher than the correlation between f_{STF} and f_S (Fig. 7a,c) with cross-correlation coefficients of about 0.90 and 0.57, respectively. This indicates that the large subevent determines f_{STF} the most, which agrees with the theoretical results shown in Fig. 3.2b. We find that the corner frequencies of subevents f_S and f_L are overall higher than the earthquake corner frequency f_{STF}. The correlations between f_{STF} and subevent corner frequencies further support the finding of *Danré et al.* (2019) that the moment of subevents is correlated to the moment of the main event for self-similar earthquakes.

The color coding in Fig. 3.7a and 3.7b indicates that with increasing moment ratio M, the difference between f_{STF} and f_S tends to increase, whereas the difference between f_{STF} and f_L tends to decrease, which is also observed in Fig. 3.2a. The plot of the f_S/f_{STF} and f_L/f_{STF} ratios in Fig. 3.8a further illustrate this. The limitation in frequency bandwidth could result in increasing f_S/f_{STF} with M if f_S is high enough, but here most corner frequency estimates are within 0.7 Hz, which should be resolvable given a time step of 0.005 s. Beginning with a similar spread at $M = 1$, the scatter in f_S/f_{STF} increases with increasing M, whereas f_L/f_{STF} tends to cluster to a value of about 1.2. Although f_L/f_{STF} is expected to approach 1 theoretically for the highest values of M, we suspect that the misfit of the decomposition of STF renders Ω_{sum} to have a slightly different frequency content than Ω_{STF}. Fig. 3.7c and 3.7d show that for an increasing absolute onset time difference $|T|$ between subevents, f_{STF} and f_L decreases. This is consistent with the fact that $|T|$ controls the total source duration, which is inversely proportional to the corner frequency of the Brune pulse. Therefore, f_{STF} and the closely correlated f_L are inversely proportional to $|T|$, whereas the change of f_S with $|T|$ is less obvious due to high scatter.

Fig. 3.8b shows an asymmetry in the ratios f_S/f_{STF} and f_L/f_{STF} with reference to $T = 0$, implying that the order of the large and small subevents of subevent (i.e., $T >0$ and $T <0$) has an influence on the corner frequency estimates. The variation in f_S/f_{STF} for $T < 0$ is two times higher than for $T > 0$, suggesting that f_S is similar to f_{STF} and better constrained if the small subevent precedes that large subevent. The variation in ratio f_L/f_{STF} does not change with T, but the mean value of f_L/f_{STF} for $T < 0$ is slightly smaller than f_L/f_{STF} for $T > 0$ (1.60 versus 1.79). Because the absolute value of T is higher than 1 for most STFs in the SCARDEC catalog (see Fig. 6b), the relatively small influence of T on f_L/f_{STF} is consistent with Fig. 3.2a, where we found that f_{STF} depends strongly on T only when $|T| < 1$.

The Brune model relates the corner frequency f_c to stress drop $\Delta\tau$ assuming a circular crack model:

$$\Delta\tau = \frac{7M_0 f_c^3}{16\beta^3 k^3} \tag{3.6}$$

Here k is a constant and β is the shear-wave velocity (Madariaga, 1976). In equation (6), $\Delta\tau$ represents the average stress change on the fault plane. Analogous to our definitions for f_{STF}, we define Δ_{STF} as the average stress drop determined for the SCARDEC STF. Further, we define Δ_L and Δ_S and M_L and M_S as the stress drops and seismic moments of the large and small subevents, respectively. The shear-wave velocity is referred from PREM (*Dziewonski and Anderson*, 1981) model. We assume the rupture velocity is about 0.7β (*Ye et al.*, 2016; *Hayes*, 2017; *Chounet et al.*, 2018). The value of k is related to the spherical average of the corner frequency and is different for P and S waves (*Sato and Hirasawa*, 1973; *Madariaga*, 1976; *Kaneko and Shearer*, 2014, 2015; *Wang and Day*, 2017). Because SCARDEC STFs are obtained by averaging P and S waves after removal of Green's functions, we set k as 0.32 according to *Sato and Hirasawa* (1973) and *Kaneko and Shearer* (2015). $\Delta\tau_{STF}$, $\Delta\tau_L$, and $\Delta\tau_S$ are proportional to the cube of f_{STF}, f_L, and f_S. Therefore, as for f_L, f_S, and f_{STF}, the correlation between $\Delta\tau_{STF}$ and $\Delta\tau_L$ is higher than the correlation between $\Delta\tau_{STF}$ and $\Delta\tau_S$ (Fig. 9a). The correlation of Brune stress-drop estimates with the largest asperity supports the usage of the moment-weighted stress drop and the energy-based stress drop (*Noda et al.*, 2013). $\Delta\tau_L$ and $\Delta\tau_S$ are also larger than $\Delta\tau_{STF}$ (Fig. 9b). For 50% of the STFs $\Delta\tau_L$ and $\Delta\tau_S$ are larger than $\Delta\tau_{STF}$ by a factor of 4, and stress drops of the small subevents is an order of magnitude higher than the overall stress drop for 20% of the earthquakes in the SCARDEC catalog (see also Fig. 6c).

3.6 Comparison With Finite-fault Inversion Results

Through the STFs decomposition, we find that the corner frequency of the master event is more related to the largest subevent. STFs show temporal behavior of the rupture moment release, but, however, provide no spatial information of the rupture process. Thus, we compare subevent corner frequencies measured from STFs with rupture dimensions of subevents estimated from finite-fault inversion data sets. *Ye et al.* (2016) applied finite-fault inversion to teleseismic P waveforms of 114 earthquakes larger than Mw 7.0. We fit the source spectra of STFs from finite-fault inversion to the Brune source model to estimate the corner frequency of the earthquake f_{STF} and convert it to rupture radius following $r_{STF} = k\beta/f_{STF}$, in which k is a constant and β the shear-wave velocity. Assuming an average crustal shear-wave velocity ($\beta = 3.5$ km/s), the rupture velocity used by *Ye et al.* (2016) (2.5 km/s) is 70% of the shear-wave velocity. We use corresponding k values of P waves from *Sato and Hirasawa* (1973) and *Kaneko and Shearer* (2015). We then decompose STFs to estimate the moment of the largest subevent. Assuming that the largest subevent with the highest slip can be approximated by a circle, we use the moment release distribution to find the radius r_{FNT} when the total moment release within the circle is equal to the largest subevent. As an example, Fig. 3.10a and 3.10b display the STF for the 18 April 2014 Guerrero earthquake and its slip map where the circle with a radius of $r_{FNT} = 24$ km outlines the region of slip of the largest subevent.

Fig. 3.10c and 3.10d shows that r_{STF} is positively correlated with r_{FNT}. The radius r_{STF} depends linearly on k. For $k = 0.23$ (*Sato and Hirasawa*, 1973) r_{STF} is about 30% higher than for k =0.32 (Kaneko and Shearer, 2015), but k has no influence on the correlation between r_{STF} and r_{FNT}. A change of 10% moment would result in approximate 10% change of the radius. The estimation of r_{FNT} is rough because the rupture areas of subevents may not be circles. Nevertheless, the proportionality of r_{STF} and r_{FNT} supports our conclusion that the largest subevent strongly influences estimates of the earthquake corner frequency and rupture dimension and estimates of earthquake corner frequency to represent rupture dimensions of the largest subevent.

3.7 Indication On Stress-drop Variability

Stress drops estimated from the SCARDEC STFs data set (i.e., $\Delta\tau_{STF}$ in Fig. 9a) have a standard deviation of about a factor of 3.5. This standard deviation is close to the factor-of-three variability of stress drop estimated from the SCARDEC STFs of nonstrike-slip earthquakes by *Courboulex et al.* (2016) and is similar to the variability of stress drop

estimated from the moment rate functions of earthquakes in dynamic rupture simulations (*Gallovič and Valentová*, 2020). *Allmann and Shearer* (2009) obtained a stress-drop variability of about a factor of 4.5 using a spectral fitting method based on global numerical Green's functions. Our results show that the stress-drop variability may be a consequence of earthquake complexity. Whereas for a simple source, the stress drop inferred from the Brune source corner frequency represents the average stress drop on the fault plane, the stress drop of a complex rupture with multiple subevents is influenced strongly by the largest subevent. Therefore, earthquakes with the same magnitudes can have varying stress drops depending on the source complexity and the largest subevent dimension. This could explain the significant higher variability of stress drop estimated from STFs of simulated ruptures than the variability of stress drop prescribed in dynamic rupture models (*Cotton et al.*, 2013; *Lin and Lapusta*, 2018; *Gallovič and Valentová*, 2020). A better understanding of the source of stress-drop variability helps to predict ground velocity and acceleration after major earthquakes, which are essential for the seismic hazard assessment.

In addition to the source complexity, the simplicity of the Brune source model itself can also lead to a systematic deviation of the stress-drop estimation. The Brune source model is widely applied due to its simplicity, but also suffers from inaccurate representation for complex earthquake sources. Although we obtain similar distributions of subevent numbers using the Brune source model as Danré et al. (2019) who used the Gaussian source model, the variation of stress-drop estimates is cubed when stress drop is converted from corner frequency estimates. Apart from the model choice, the quality of data set (Green's function removal in SCARDEC STFs), the frequency bandwidth, and the spectral fit method all contribute to the corner frequency and stress-drop variation.

3.8 Appication To Spectral Ratios

Because the spectral ratio method is frequently used to estimate corner frequencies (e.g., *Abercrombie*, 2015; *Huang et al.*, 2016; *Uchide and Imanishi*, 2016; *Liu et al.*, 2020), we explore the resolution of the corner frequencies of a large earthquake (referred to as the master event hereafter) after dividing its spectrum Ω_M by the spectrum ω_E of a collocated but smaller earthquake. The spectral ratio method isolates the source term of the master event, because for the same station the propagation and receiver effects are the same in Ω_M and Ω_E. Therefore, the smaller earthquake can be regarded as the empirical Green's function (referred to as eGf hereafter).

Assuming Brune sources as in equation (1), the spectral ratio is $\Omega_ratio(f, f_{ratio}, M_{ratio}) = \Omega_M(f, f_M, M_M)/\Omega_E(f, f_E, M_E)$, in which, M_M, M_E, f_M, f_E are seismic moments and

corner frequencies of the master event and the eGf. The spectral ratio Ω_{ratio} has a seismic moment ratio M_{ratio} and a first corner frequency f_{ratio} (i.e., master event corner frequency inferred from the spectral ratio method). The spectral ratio also has a second corner frequency that corresponds to the eGf corner frequency. If f_E is much higher than f_M, Ω_{ratio} is equivalent to Ω_M and f_M is equivalent to f_{ratio}. If f_E is similar to f_M, Ω_{ratio} decays more slowly at high frequencies than Ω_M. There are two approaches to get the source spectral information M_M and f_M: (1) removing the Green's function and performing spectral fitting (e.g., *Allmann and Shearer*, 2007; *Shearer et al.*, 2006, 2019)(e.g., and (2) fitting the spectral ratio of two Brune models based on empirical Green's function (e.g., *Abercrombie*, 1995, 2014, 2015), with two approaches benchmarked in *Shearer et al.* (2019).

We show the spectra and the spectral ratio of the second spectral ratio approach in Fig. 3.11a. Fig. 3.11c and 3.11d demonstrate this for the master events used in Fig. 3.2 (i.e., events composed of two subevents with onset time difference of $T = -2$ s and $T = +2$ s) that have a corner frequency $f_M = 0.19$ Hz for both cases of T. The eGfs used to compute Ω_{ratio} are single-pulse Brune sources with corner frequencies of 0.5 Hz (Fig. 11c) and 1.5 Hz (Fig. 11d). In both cases, f_{ratio} is inferred to be lower than f_M because the first oscillation in the spectral ratios causes an earlier and faster decay near f_M (Fig. 2b). This decreasing effect on f_{ratio} is stronger when the eGf has a corner frequency closer to f_M. For f_E higher than 1 Hz, f_{ratio} approaches f_M asymptotically (Fig. 11b). In addition, the sequence of the large and small subevents affects f_{ratio}. The master event corner frequency is inferred to be larger when large subevent precedes small subevent ($T = -2$ s).

There is an upper bound of the frequencies (2 Hz in our case) in the source spectrum used for the fitting of the Brune source spectrum. Because Ω_M and Ω_E decay identically above f_E, the first corner of a spectral ratio is primarily determined by signals at frequencies lower than f_E that is usually smaller than the upper frequency range. For multisubevent earthquakes, oscillations at frequencies smaller than f_E dominate the modeling of spectral ratios. Theoretically, if the eGf has the form of a single-pulse Brune spectrum, its corner frequency does not strongly influence the estimate of the corner frequency of the master event. For complex master events, however, oscillations at frequencies smaller than f_E, rather than the overall fall-off, control the fitting. As f_E decreases, we are more likely to fit the first oscillation, which has a corner frequency smaller than the master event. Therefore, the spectral ratio method yields a larger variance in the estimated corner frequency than the direct fitting of earthquake source spectra when the master event consists of multiple subevents.

3.9 Discussion

It is necessary to differentiate two subevent corner frequencies in our analysis from the double corner-frequency model (*Archuleta and Ji*, 2016; *Denolle and Shearer*, 2016; *Uchide and Imanishi*, 2016; *Wang and Day*, 2017). The double corner-frequency model has an additional corner compared to the Brune source model and variable fall-off rates, so it can better model complex source spectra at high frequency. The underlying physics of an additional corner is an extra time scale relating to one of the following source properties: the slip rise time (*Brune*, 1970), the time between the starting and stopping phases (*Luco*, 1985), the spacing of barriers and asperities (*Denolle and Shearer*, 2016), and the superposition of two subevents (*Atkinson*, 1993). *Ji and Archuleta* (2021) has systematically proposed two empirical double corner-frequency models that reproduce the mean peak ground acceleration, the mean peak ground velocity, and the breakdown of self-similarity around magnitude Mw 5.3 using a stochastic ground motion model. Recently, *Ji and Archuleta* (2022) further showed that their models can be explained by fault geometry scaling relations and the high-frequency radiation is related to the fault plane aspect ratio. In comparison, our analysis assumes that each subevent is a Brune source model, and the complete earthquake is a superposition of several Brune sources. Most studies estimated a single corner frequency from the spectra of complete earthquakes, and our study aims to understand the best interpretation of these corner frequencies. Our model and double-frequency models are based on different source models, but both try to characterize the corner frequency that is critical for stress drop and ground-motion predictions. Our results also indicate that measuring stress drops of subevents can be important for constraining stress drop for ground-motion simulations. *Courboulex et al.* (2022) found that the stress drop estimated from the total duration of the SCARDEC STF can be applied to groundmotion prediction for subduction zone earthquakes, implying that using multiple subevents to constrain stress drops may significantly improve simulation performance.

Our decomposition approach is the same as *Danré et al.* (2019), but we assume the Brune source instead of the Gaussian source used in their analysis. The Gaussian source model is described by three source parameters and is thus more adaptable than the Brune source model with two parameters. Though *Danré et al.* (2019) resolved more subevents than found in this study, the relative number of subevents per faulting type are consistent in two studies, indicating that source models have little effect on the analysis. We also plot the subevent moment as a function of the earthquake moment (Fig. 3.12, available in the supplemental material to this article) and observe a positive correlation pattern, in agreement with their result. Furthermore, our finding that larger subevents tend to pre-

cede smaller subevents supports the conclusion in *Danré et al.* (2019) that the main event magnitude can be estimated after observing only the first few subevents, which can have significant impact on earthquake early warning. Both *Danré et al.* (2019) and our study showed that the smallest earthquakes have the fewest subevents, but both studies are limited by the decomposition method and the resolvable frequency bandwidth of SCARDEC STFs, which are obtained from teleseismic body-wave phases. Because teleseismic waveforms above 0.5 Hz have relatively low signal-to-noise ratios and STFs are averaged over stations, high-frequency contents are deficient in SCARDEC STFs. In addition, the decomposition method requires subevents to have moments that are at least 10% of the total moment. Therefore, it is likely that smaller subevents were missed by our analysis. The spectral analysis of regional and local seismograms would enable a study of the relationships of corner frequencies and rupture dimensions of subevents of Mw 3–4 earthquakes to test whether small earthquakes are as complex as large earthquakes (e.g., *Fischer*, 2005; *Abercrombie*, 2014; *Ruhl et al.*, 2017).

SCARDEC STFs above 0.5 Hz are inaccurate due to the wave attenuation and wave propagation complexities as well as averaging of spectra from global stations. This inherent lack of high frequency of SCARDEC STFs reduces our resolution of subevents for smaller earthquakes. Fig. 3.12 shows that the moment magnitude of the smallest subevent is constantly 1.3 smaller than the earthquake magnitude, which is also observed in *Danré et al.* (2019). The reason could either be that it is the smallest resolvable subevent magnitude due to limited frequency bandwidth or that it is truly the smallest subevent magnitude. Considering the available frequency bandwidth of SCARDEC STFs, subevents larger than Mw 5.5 should be resolvable, suggesting that at least the decomposition of earthquakes larger than Mw 6.9 should be accurate. In other words, earthquakes smaller than Mw 6.9 could be found to have more subevents given a higher frequency range.

One thing to be noted is that our analysis is from the teleseismic perspective. The results might be different from the regional perspective, because high-frequency energy of small subevents would be less attenuated and contribute more to the earthquake spectra. Stress-drop estimates of the same event using teleseismic and regional data have also been found to be disparate (e.g., *Hartzell et al.*, 2013). Therefore, additional tests using regional data are worth doing in the future, which, however, is out of the scope of this article.

3.10 Conclusions

We use SCARDEC source time functions to investigate how estimates of the corner frequency of earthquakes with multiple subevents are biased by assuming a simple Brune

source. By decomposing SCARDEC STFs using the Brune source model, we find more than half of Mw 5.5–8.0 earthquakes have multiple subevents. We derive theoretical solutions of the source spectrum for an earthquake with two Brune-type subevents. The theoretical derivation demonstrates that the earthquake corner frequency correlates better with the corner frequency of the large subevent than the small subevent. In both synthetic tests and the analysis of the SCARDEC catalog, earthquake corner frequency approaches the largest subevent corner frequency as the moment ratio between subevents increases, whereas the onset time difference between subevents has a minor effect with slight asymmetry. The positive correlation is also observed for earthquake rupture dimension estimated from its corner frequency and rupture dimension of the largest subevent estimated from finite-fault inversion. Our findings suggest that for the Brune source model, the corner frequency estimates may reflect the stress change of the largest asperity instead of the average stress drop on the whole rupture area, which helps to explain the commonly observed large variance of stress-drop estimates.

3.11 Figures - Chapter 3

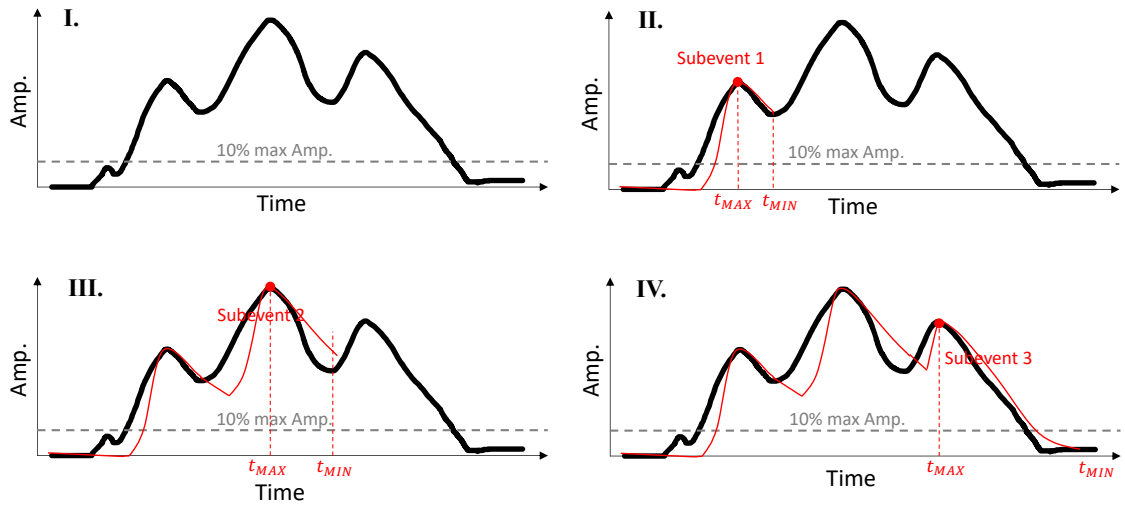

Figure 3.1: Flowchart of STF decomposition. (a) Set 10% of the maximum amplitude as the water level, below which pulses would not be fitted. (b) Fit the first pulse to subevent 1. The time of the maximum amplitude (t_{MAX}) is also the peak time of subevent 1. The time of minimum amplitude (t_{MIN}) after the pulse is the end boundary of calculating misfit. (c) Fit the second pulse to subevent 2. t_{MAX} and t_{MIN} are updated accordingly. (d) Fit the last pulse to subevent 3. t_{MIN} is updated as the end of time. The color version of this figure is available only in the electronic edition.

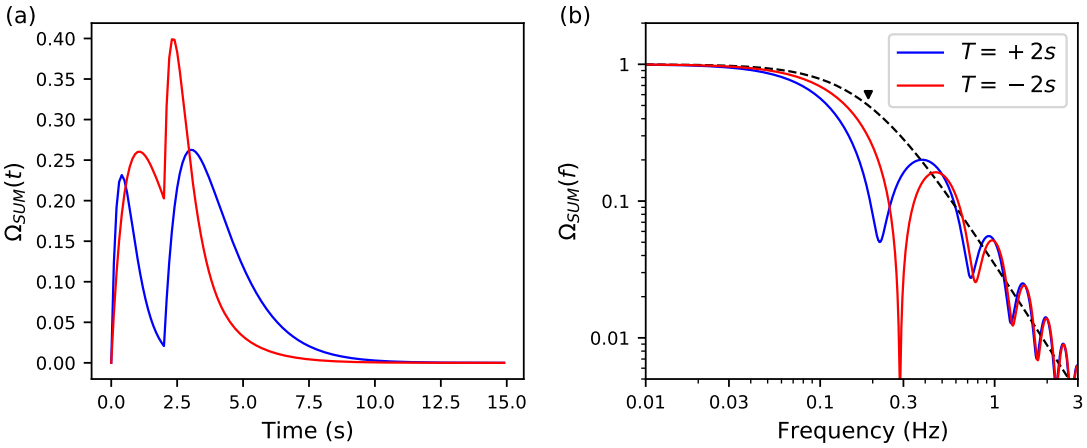

Figure 3.2: (a) Ω_{sum} for a sum of two Brune pulses. The large and small subevents have corner frequencies of 0.15 and 0.40 Hz, respectively. The moment ratio $M = M_L/M_S = 3$. In cases 1 (red) and 2 (blue), the largest pulse is the first and second in the sequence so $T = -2$ s and $T = +2$ s, respectively. (b) Amplitude spectra (solid lines) of the STFs with corresponding colors shown in panel (a). The dashed line is the spectrum of a single-pulse Brune source that best matches Ω_{sum} in a least-squares sense. They are virtually the same for $T = -2$ s and $T = +2$ s. The corner frequency of this Brune source is $f_{sum} = 0.19$ Hz. The color version of this figure is available only in the electronic edition.

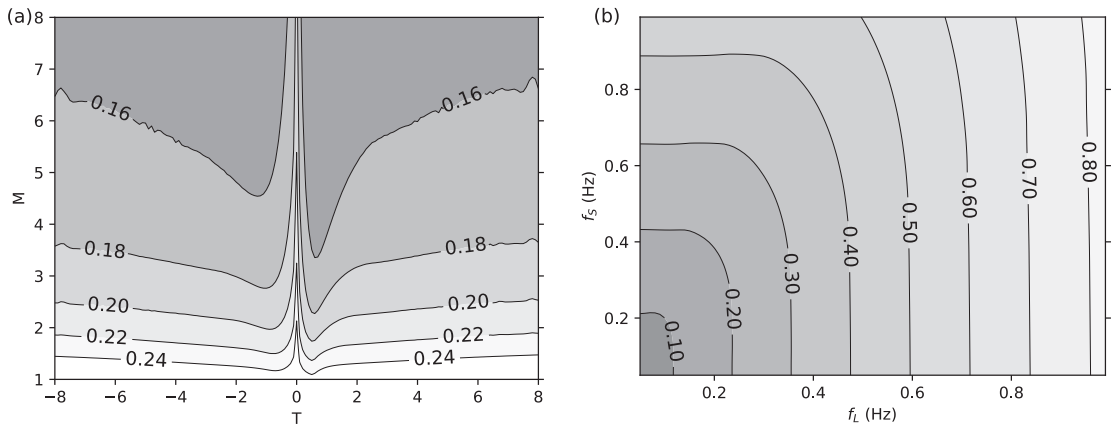

Figure 3.3: (a) Contour plot of the corner frequency f_{sum} as a function of T and M. The subevent corner frequencies are $f_L = 0.15$ Hz and $f_S = 0.40$ Hz. (b) Contour plot of f_{sum} as a function of f_L and f_S. The moment ratio and onset time difference of the two subevents are $T = 2$ s and $M = 3$.

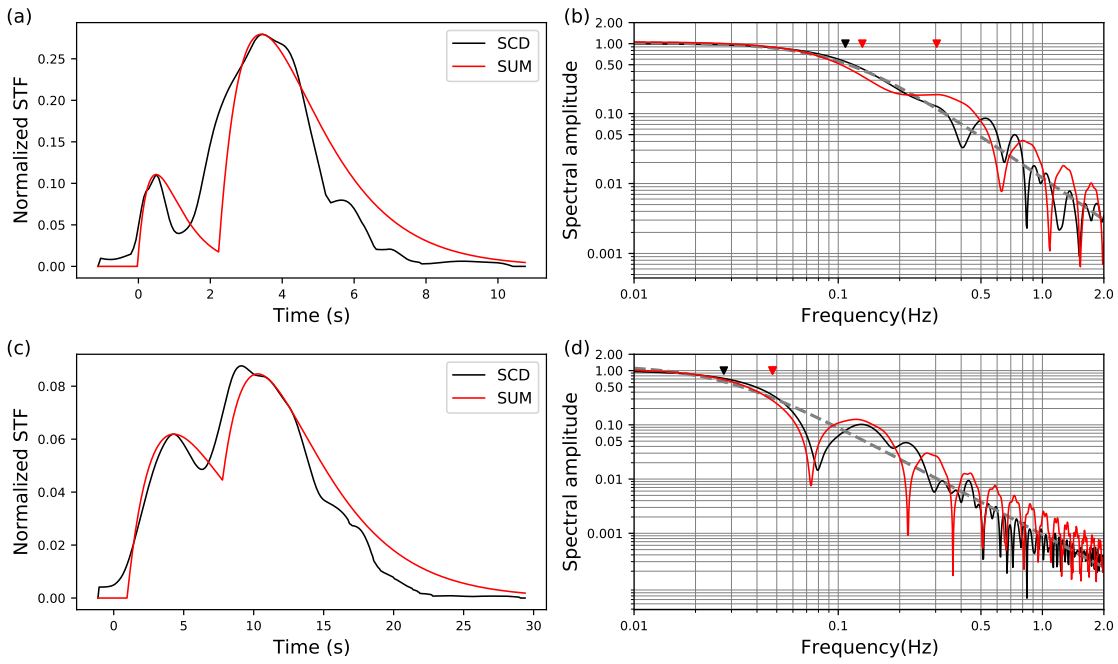

Figure 3.4: (a) Normalized STFs of the Caroline Islands Mw 6.2 earthquake on 8 December 2017 from the seismic source characteristic retrieved from deconvolving teleseismic body waves (SCARDEC) data set (black line) and the best-fitting sum sum of two Brune subevents (red line). (b) The spectra of the STF (black line), STF (dashed line), and sum (red line). The corner frequency $f_{STF} = 0.11$ Hz is marked by a black reversed triangle. The corner frequencies $f_L = 0.13$ Hz and $f_S = 0.30$ Hz are marked by red reversed triangles. (c,d) same as panels (a) and (b), but for the Mw 7.6 southern Chile earthquake of 25 December 2016, with corner frequencies $f_{STF} = 0.028$ Hz, $f_L = 0.048$ Hz, and $f_S = 0.048$ Hz and $M = 1.08$. The color version of this figure is available only in the electronic edition.

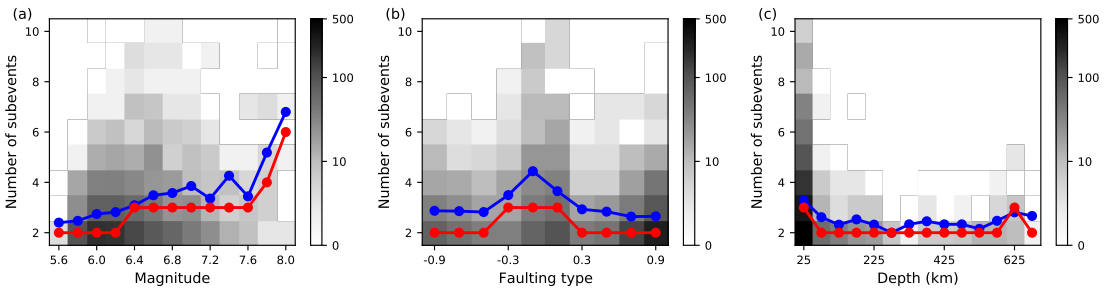

Figure 3.5: Contour plot of the number of earthquakes. The y-axis shows the number of subevents in the STF up to 10. The x-axis indicates the earthquake's (a) moment magnitude, (b) faulting type, and (c) focal depth. The values of faulting type range from -1 (normal faulting) to 0 (strike-slip faulting) to $+1$ (reverse faulting) following the quantification by Shearer et al. (2006). The blue and red circles signify means and medians determined for bins of ± 0.1 (moment magnitude), ± 0.1 (faulting type), and ± 25 km (focal depth). The color version of this figure is available only in the electronic edition.

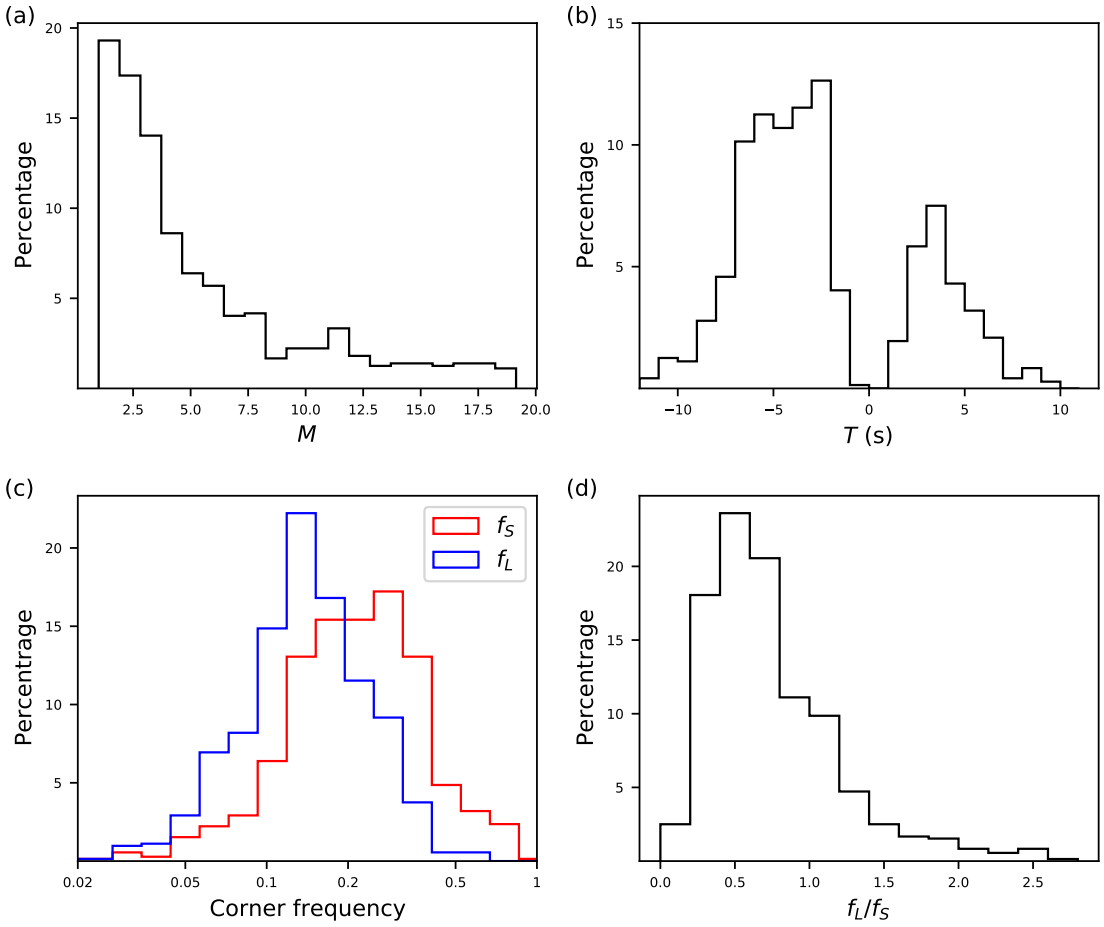

Figure 3.6: Histograms of (a) moment ratio $= M_L/M_S$, (b) onset time difference $T = t_L - t_S$, (c) corner frequency of the largest subevent f_L and of the smallest subevent f_S, and (d) ratio of f_L to f_S for 714 STFs with two subevents in the SCARDEC catalog. The color version of this figure is available only in the electronic edition.

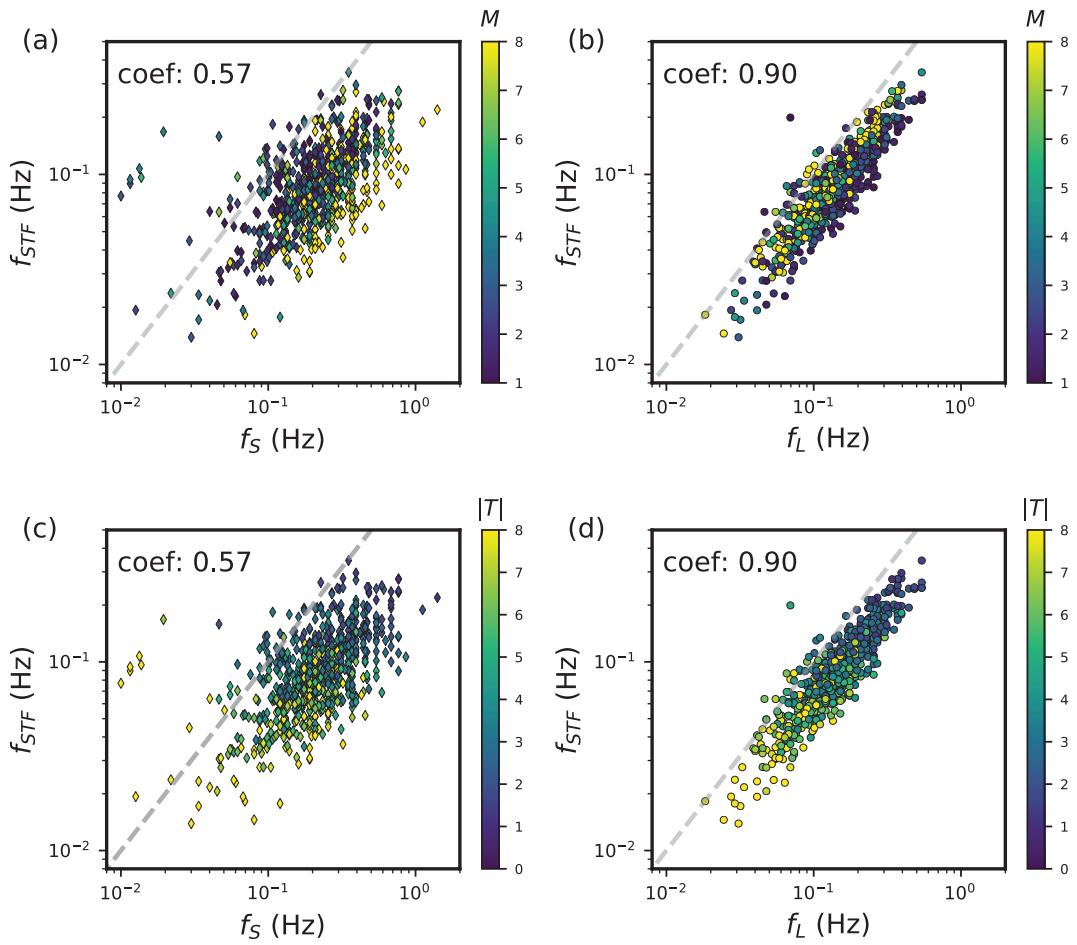

Figure 3.7: (a,b) The corner frequency f_{STF} as a function of the corner frequency f_S and f_L color coded by moment ratio M. (c,d) The corner frequency f_{STF} as a function of the corner frequency f_S and f_L color coded by absolute onset time difference $|T|$. The dashed lines indicate a 1:1 correlation. The color version of this figure is available only in the electronic edition.

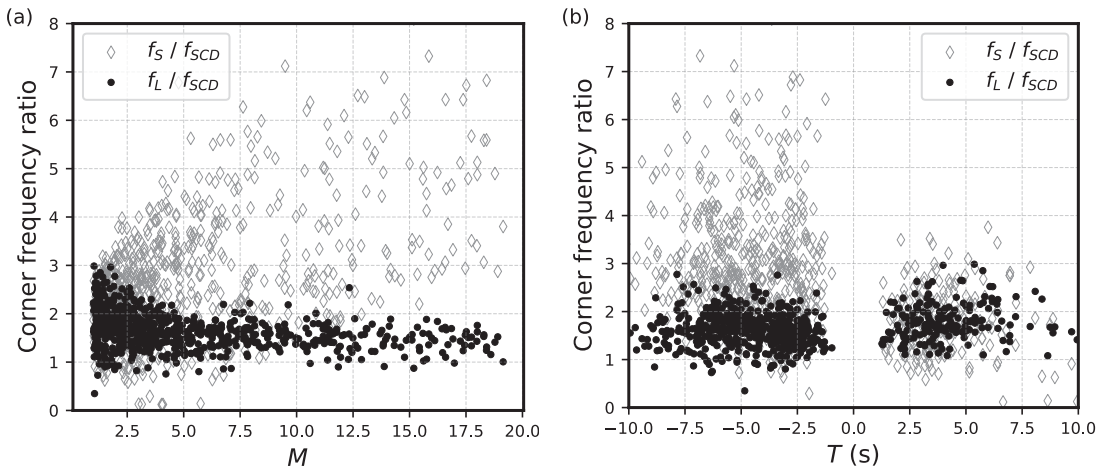

Figure 3.8: The ratio between corner frequencies f_L (solid black circles) and f_S (gray open diamonds) to f_{STF} as a (a) function of moment ratio M (b) and onset time difference T.

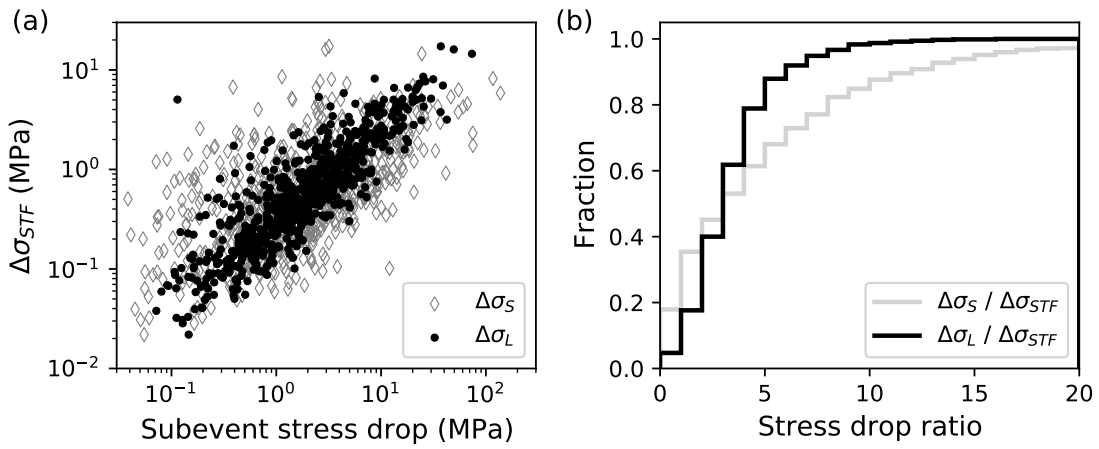

Figure 3.9: (a) Average stress drop $\Delta\tau_{STF}$ as a function of the stress drop $\Delta\tau_L$ (circles) and $\Delta\tau_S$ (diamonds) of the large and small subevents, respectively. (b) Cumulative fraction of the ratios $\Delta\tau_L/\Delta\tau_{STF}$ (black line) and $\Delta\tau_S/\Delta\tau_{STF}$ (gray line).

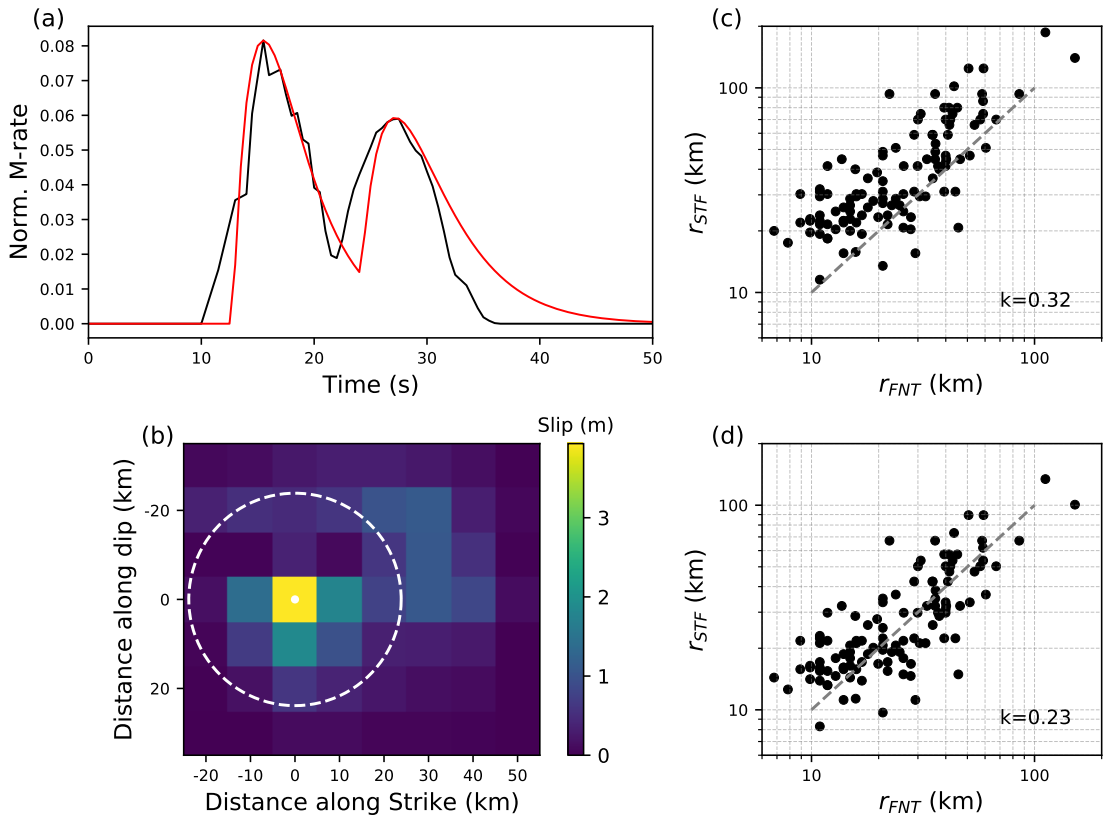

Figure 3.10: (a) The normalized source time function and (b) slip distribution in Ye et al. (2016) for the 18 April 2014 Mw 7.3 Guerrero earthquake. The black curve in panel (a) is the STF from finite-fault inversion and the red curve is its decomposition into two Brune sources. The white dashed circle in panel (b) with a radius $r_{FNT} = 24$ km signifies the rupture area of the largest subevent. The best-fit Brune corner frequency is $f_{STF} = 0{:}04$ Hz. (c) Radius r_{STF} converting from f_{STF} using $k = 0.32$ as a function of the largest subevent radius r_{FNT} measured from finite-fault inversion. The gray dashed line signifies a 1:1 relation. (d) Same as panel (c), but with $k = 0.23$. The color version of this figure is available only in the electronic edition.

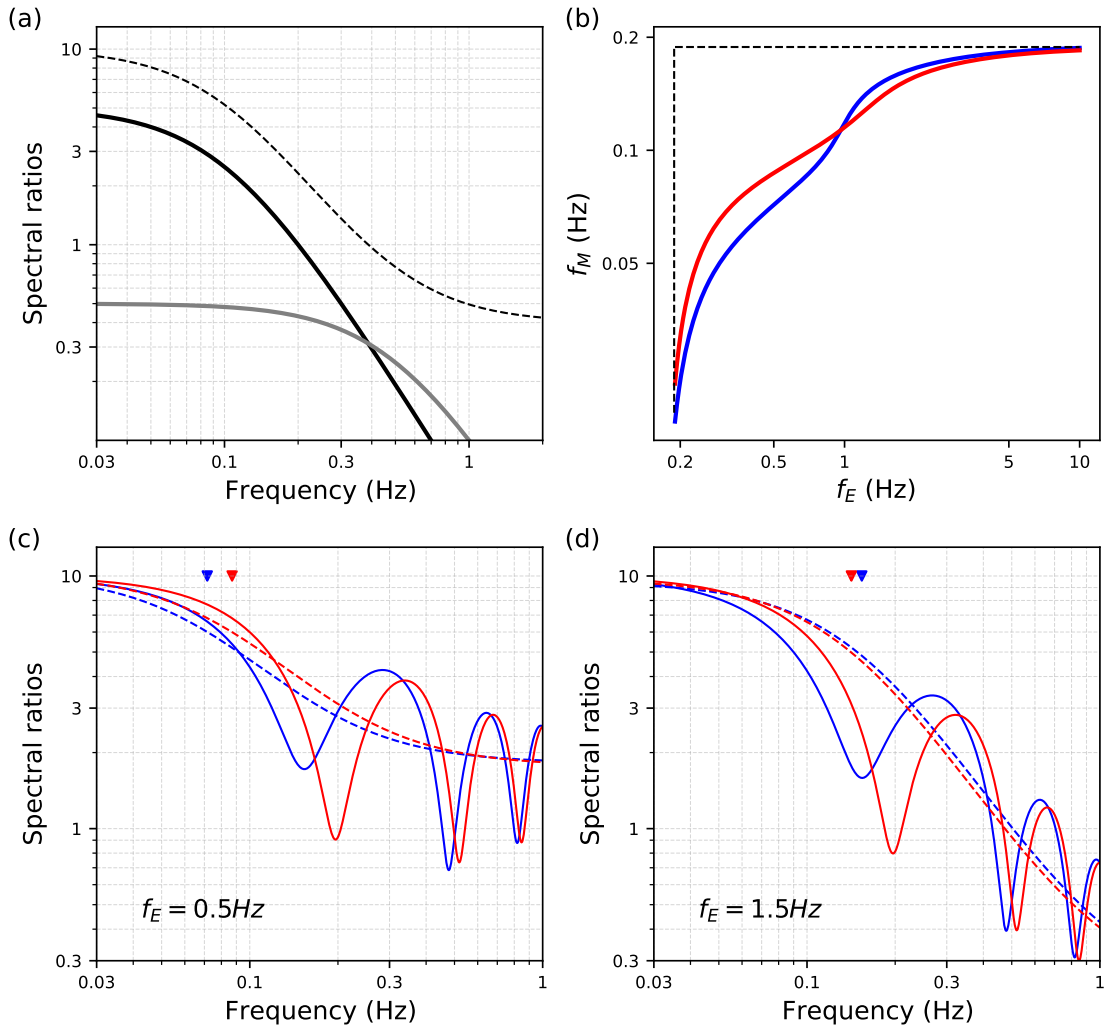

Figure 3.11: (a) Spectra of the master event (black solid) with $f_M = 0.1$ Hz, $M_M = 5$ and the eGf (gray solid) with $f_E = 0.5$ Hz, $M_E = 0.5$ Hz as well as their spectral ratio (dashed line). (b) f_M as a function of f_E for $T = +2$ s (blue) and $T = -2$ s (red). The horizontal and vertical black dashed lines indicate the corner frequency $f_M = 0.19$ Hz of the master event. (c) Spectral ratios for $T = +2$ s (blue) and $T = -2$ s (red) when $f_E = 0.5$ Hz. The master event has the same spectra as the spectra shown in Figure 2. The corners f_M of the spectral ratio Ω_M are indicated by reversed triangles for the cases where the large subevent precedes (in red) or succeeds (in blue) the small subevent by 2 s. (d) Same as panel (a) for $f_E = 1.5$ Hz. The color version of this figure is available only in the electronic edition.

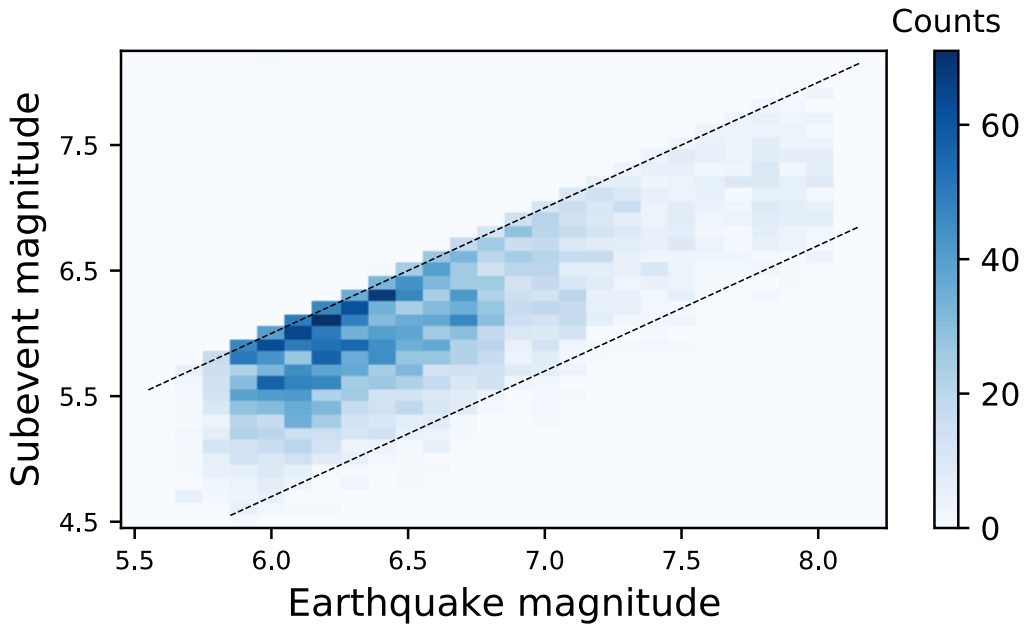

Figure 3.12: Count map of subevents against the subevent magnitude and the earthquake magnitude. The top dashed line represents that the earthquake's moment magnitude equals the subevent moment magnitude, and the bottom dashed line represents that the moment magnitude of the earthquake is 1.3 larger than that of the subevent.

CHAPTER 4

Stress Drop Estimation using a Point-Wise Stacking Method *

4.1 Introduction

Stress drop quantifies the change in shear stress on a fault before and after a rupture, and the energy released during an earthquake. It controls the amplitude and frequency content of ground motions which are used to assess seismic hazard, and offers insight into the fault strength and other physical properties of the fault zone such as the presence of fluids.

The spectral ratio method based on empirical Green's function is the prevailing technique for stress drop estimation. Yet, it is plagued by three orders of magnitude stress drop estimate variation. So it is often necessary to exclude data due to stringent signal-to-noise ratio requirements. Here we explore the stress drop estimation robustness, introducing a novel point-wise spectral ratio stacking approach resulting in more precise and consistent stress drop estimates. We apply this approach to shallow and deep earthquakes to understand stress drops.

A complete depth profile from 0 to down to 700 km depth of stress drop estimation is lacking. Most studies on depth dependence of stress drop are focused within the crust or shallower than 50 km (e.g., *Hardebeck and Aron*, 2009; *Trugman et al.*, 2017; *Trugman and Shearer*, 2017; *Trugman*, 2020). One of the reasons is that earthquakes deeper than 50 km are of a different faulting nature. The other reason is the lack of data due to the decreasing earthquake occurrence as depth increases. Even for shallow earthquakes, the depth dependence of stress drop is still controversial. *Allmann and Shearer* (2007) found that the increasing stress drops could be attributed to the increasing shear wave velocity. *Bilek and Lay* (1998) use the variation of rigidity in the subduction zone to explain the depth variation of stress drop. *Abercrombie et al.* (2021) found the depth dependence of

*Chapter 4 is to be submitted to *Geophysical Research Letters*: Liu, Meichen, Yihe Huang, and Jeroen Ritsema. "Stress Drop Estimation using a Point-Wise Stacking Method"

stress drop becomes negligible after depth-dependent attenuation correction. Considering regional tectonic variations and the correlation between depth and focal mechanism, stress drop is generally not proven to pronouncedly increase with depth. For intermediate-depth (50-350 km) and deep-focus (>350 km) earthquakes, *Poli and Prieto* (2016) generally observed depth-independent stress drop globally while *Tian et al.* (2022) observed decreasing median stress drop for intermediate and deep-focus earthquakes in Tonga Slab respectively. As shown in Chapter 2, our stress drop estimates display a slightly increasing trend with depth. However, the lack of data is a common problem for deep earthquakes, therefore the resulting estimates could easily be biased. With the new stacking method maximizing the utilization of seismic waveforms, we will have much more data to use for stress drop estimation. We can recalculate the stress drop of shallow earthquakes and potentially reduce the variation, though, our goal is to further create a complete depth profile of stress drop.

4.2 Methods

In the conventional stress drop estimation technique utilizing spectral ratio stacking based on empirical Green's functions (eGf), rigorous quality control procedures are imposed on seismic recordings. Specifically, both the windowed waveforms of the master event and the eGf from the same station must have a mean signal-to-noise ratio within specific frequency ranges that exceed a minimum signal-to-noise ratio threshold.

However, this approach discards potentially useful information and introduces biases into the stacked spectral ratios. For instance, at frequencies where the signal spectral amplitude is high and the noise spectral amplitude is low, it may be excluded if the average signal-to-noise ratio does not meet the required threshold, and vice versa. If an average signal-to-noise ratio is used, including high noise spectral amplitude and excluding large signal spectra amplitude at certain frequencies are inevitable. This drawback may significantly influence the final spectral ratio if the high noise spectral amplitude appears at consistent frequency ranges at different stations.

To maximize the utilization of spectra information and minimize bias, we propose a point-wise spectral stacking method compared to the conventional trace-wise approach. The mathematical framework for point-wise stacking is shown below.
(1) Given a spectral signal amplitude $A_{signal}(f)$ and the corresponding noise amplitude $A_{noise}(f)$, calculate the the signal-to-noise ratio at each frequency.

$$A_{ratio}(f) = A_{signal}(f)/A_{noise}(f) \tag{4.1}$$

(2) Set a minimum signal-to-noise ratio R_{min}, compare $A_{ratio}(f)$ against R_{min}.
(3) Stack spectral ratio $A_{stack}(f)$ and the number of stacks at this frequency $Num(f)$.
If $A_{ratio}(f_i) \geq R_{min}$, we include it into stacking.

$$A_{stack}(f_i) = A_{stack}(f_i) + A_{ratio}(f_i) \tag{4.2}$$

$$N_{stack}(f_i) = N_{stack}(f_i) + 1 \tag{4.3}$$

If $A_{ratio}(f_i) < R_{min}$, we skip it.
(4) Average the stacked spectral ratio, yielding the final point-wise stacked spectral ratio.

$$A_{final}(f_i) = A_{stack}(f_i)/N_{stack}(f_i) \tag{4.4}$$

Fig. 4.1 compares the conventional trace-based stacking method and the point-based stacking method. The points-based method selectively incorporates frequencies where both the master event and eGf event exhibit high signal-to-noise ratios.

4.3 Synthetic tests

To systematically determine whether the point-based stacking method is better than the trace-based stacking method and how the point-based stacking method improves the accuracy of stress drop estimates, we performed pseudo synthetic tests using seismic recordings.

We use the Brune source model

$$S(f) = \frac{M_0}{1 + f^2/f_c^2} \tag{4.5}$$

where f_c is the corner frequency. We set the corner frequencies for master and eGf events to $f_M = 0.2$ Hz and $f_{eGf} = 1.0$ Hz, respectively. To accurately simulate the signal and noise spectra, we conducted the following steps.
(1) Select 20 shallow earthquakes in each magnitude range: Mw 5.0-5.5, Mw 5.5-6.0, Mw 6.0-6.5, Mw 6.5-7.0, Mw 7.0-7.5, and Mw 7.5-8.0. Use only teleseismic stations with epicentral distances falling within the range of 30 to 110 degrees.
(2) Calculate spectra using time windows of -5 to 35 seconds for signal and -45 to -5 seconds for noise relative to the theoretical arrival time (PREM) for P-wave arrivals.
(3) Take the logarithmic average of the signal spectra within each magnitude range as the

reference signal spectra and then compute the residual signal spectra by subtracting the reference signal spectra.
(4) The residual signal spectra are added to the model spectra to create synthetic signal spectra. Corresponding synthetic noise spectra were paired with the signal spectra for signal-to-noise ratio computation.

With synthetic signal and noise spectra on hand, we can test the performance of the conventional trace-based and point-based stacking methods. We randomly selected 500 synthetic spectra in a certain magnitude range and varied the level of noise spectra from 0.1 to 10 times the original noise spectral amplitude. We then applied both the conventional trace-based and point-based stacking methods to these spectra.

Our criteria for spectrum selection are as follows: For the point-based stacking method, frequencies are included only if their signal-to-noise ratio exceeds 3.0. For the conventional trace-based stacking, we consider spectra with a minimum of 70% of all frequency points to exhibit a signal-to-noise ratio greater than 3.0. As previously mentioned, the corner frequencies for the master and eGf events were kept fixed, with values of $f_M = 0.2$ Hz and $f_{eGf} = 1.0$ Hz, respectively. However, we introduced variations in the magnitude difference, ranging from Mw 0.5 to 2.5, to assess the effects of different magnitudes on our analysis. We fit the trace-based and point-based spectral ratios to the Brune source model to estimate magnitude difference, master event corner frequency, and eGf event corner frequency.

Fig. 4.2 illustrates the estimated magnitude difference between master events and eGf events using the conventional trace-based stacking method (in blue) and the point-based stacking method (in red). When employing the point-based stacking method, we observe that under low noise levels, indicative of high signal-to-noise ratios, the magnitude difference estimates closely align with the model magnitude difference. As the noise level increases, the estimated magnitude difference gradually decreases and increasingly underestimates the true value as the model magnitude grows larger. Overall, the trend indicates that estimated magnitude differences decrease as noise levels rise, with the deviation amplifying alongside higher model magnitude differences. The overall trend is that the estimated magnitude difference decreases as the noise level increases, and the deviation increases as the model magnitude difference increases. When employing the trace-based stacking method, we also observe a larger deviation from the model magnitude difference with increasing noise levels. However, these deviations may either be larger or smaller than the model magnitude difference, in contrast to the predominantly smaller magnitude differences produced by the point-based stacking method. Furthermore, estimates derived via the point-based stacking method exhibit greater stability with a reduced variance com-

pared to the trace-based method, signifying its superior performance under varying noise conditions.

Fig. 4.3 presents the estimated corner frequencies of both master events and eGf events utilizing the two stacking methods. In both (a) and (b), we observe that as noise levels increase, the estimated corner frequencies gradually diverge from the model corner frequencies. Nevertheless, the corner frequencies estimated with the point-based stacking method consistently display significantly lower variance compared to those obtained with the trace-based stacking method, especially under high noise levels. This observation underscores the point-based stacking method's resilience in the face of limited dataset sizes, making it an effective strategy for accurately estimating corner frequencies for both master events and eGf events when data availability is constrained.

4.4 Application to shallow earthquakes

We used shallow earthquakes for our comparative analysis of the conventional trace-based stacking method and the point-based stacking method. Our dataset comprises 8,522 earthquakes that occurred between 2000 and 2021, with depths less than 50 km and magnitudes falling within the range of Mw 5.5 to 7.5. To qualify as empirical Green's function events, the hypocentral distance to master events should be within one source dimension. We set maximum hypocentral distances for eGf events at 30 km, 100 km, and 500 km for master events with magnitudes within the ranges of Mw 5-6, Mw 6-7, and Mw 7-8. The magnitude of eGf events should be Mw 0.2 to 2.0 smaller than the corresponding master event. To categorize focal mechanisms, we utilized the methodology outlined in *Shearer et al.* (2006), assigning reverse, strike-slip, and normal faults for values of -1, 0, and 1, respectively. For consistency, we require that the focal mechanism of eGf events did not deviate from that of the master events by more than 0.25.

We collected global teleseismic P waveforms from (the Incorporated Research Institutions for Seismology (IRIS) with epicentral distances larger than 30 degrees. In the spectrum calculation, we employed a moving-window approach to obtain stable spectra. Starting five seconds before the P-wave arrival, we computed spectra of five 40-second windows, each overlapping with the previous by 20 seconds.

For the trace-based stacking method, we require that the signal-to-noise ratios for frequency ranges 0.025$\sim$0.1 Hz, 0.1$\sim$0.4 Hz, 0.4$\sim$0.9 Hz, and 0.9$\sim$2.0 Hz exceeded 2 for both master and eGf spectra. We further required the stacking of spectral ratios from at least five stations for each pair of master and eGf events to ensure reliable results.

For the point-based stacking method, we mandated the signal-to-noise ratio at a given

frequency exceeded 3 for both master and eGf spectra before calculating spectral ratios. Frequency points were evenly distributed in the logarithmic range of 0.025$\sim$2.0 Hz. When selecting spectral ratios, we set a criterion that a minimum of 70% of frequency points must have more than 10 stacks, and any continuous frequency points with less than 10 stacks should span less than 10% of the frequency bandwidth.

After the fitting of spectral ratios to the Brune source model, we excluded estimated master event corner frequencies below 0.05 Hz or above 1.0 Hz, considering the potential inaccuracies associated with corner frequencies estimated within an order of 2 from the frequency boundary. Ultimately, our analysis successfully yielded spectral ratios for 1,753 pairs of master events and eGf events using the trace-based stacking method, and 3,352 pairs using the point-based stacking method.

In Fig. 4.4, we compare the estimated magnitude differences to catalog magnitude differences for both stacking methods. Notably, we observe a consistent pattern of underestimated magnitude differences in both stacking methods. However, the point-based stacking method displays a significantly smaller degree of deviation compared to the conventional trace-based stacking method. A shared characteristic between both methods is that the deviation from the true values increases as the catalog magnitude difference grows, aligning with the findings of our synthetic tests. However, the estimated magnitude difference is most accurate when the catalog magnitude difference approaches zero when using the trace-based method, whereas the point-based method achieves peak accuracy when the catalog magnitude difference is approximately 0.5. In summary, the comparison between the two methods clearly demonstrated that the point-based method provides superior estimates of magnitude differences.

To ensure robust estimates for master events, we imposed an additional requirement that each master event should have estimates derived from a minimum of two eGf events. Subsequently, we calculated the geometrical mean of the corner frequencies and stress drops for master events. This process yielded estimates for 116 master events using the trace-based stacking method and 349 master events using the point-based stacking method. In Fig. 4.5, we present the master corner frequency as a function of the depth of master events. While a slight decrease in corner frequency with increasing depth is observable, the trend remains relatively subtle.

Fig. 4.6 offers a systematic comparison of estimated corner frequencies and stress drops using both methods relative to the magnitude of master events. Notably, the geometrical mean values exhibit similar trends for both stacking methods. Stress drops exhibit an increase with magnitude, while corner frequencies decrease as magnitude rises. These trends are more pronounced and discernible in the results obtained through the point-based

stacking method. The most significant difference between the two stacking methods lies in the absolute values of stress drops. Given the proportional relationship between stress drop and the cube of corner frequencies, even minor differences in corner frequency result in substantial disparities in stress drops. Specifically, the variation in stress drop using the trace-baed stacking method is approximately one magnitude larger than the stress drop estimated from the point-based stacking method. For instance, the geometric mean stress drop at Mw7.5 measures approximately 100 MPa with the trace-based stacking method, whereas it stands at around 10 MPa with the point-based stacking method. This observation aligns with the findings from synthetic tests, reinforcing the notion that the point-based stacking methods yield more stable results. Nevertheless, the increasing stress drop with magnitude raises questions about the self-similarity of stress drop. In Fig. 4.7, we delve into the relationship between stress drop and focal mechanism, demonstrating consistent patterns that normal and strike-slip earthquakes have higher stress drop than reverse fault earthquakes.

4.5 Preliminary conclusions & Future works

In conclusion, the results from both synthetic tests and the application on shallow earthquakes affirm the superior performance of the point-based stacking method over the conventional trace-based approach. Synthetic tests demonstrate that point-based stacking yields estimates with smaller variance, particularly when the number of source spectra is limited or noise levels are elevated. In contrast, the trace-based method heavily relies on a large number of spectral ratios to mitigate biases, making it sensitive to the availability of source spectra for reliable stacking.

The application of the point-based stacking method to shallow earthquakes echoes the findings from our synthetic tests. Specifically, the striking reduction in the variance of stress drop estimates, approximately one order of magnitude smaller when compared to the trace-based method, offers valuable insights for the stress drop community. This reduction implies that advancements in analysis techniques, as exemplified by the point-based stacking method, can potentially decrease the stress drop variation in seismic research teams by a significant order of magnitude.

Drawing a connection to Chapter 2, where we employed the conventional stacking method to calculate stress drops for deep-focus earthquakes, revealing values approximately one order of magnitude higher than those of shallow earthquakes, we propose the application of the new point-based stacking method to revisit deep-focus earthquakes and compare the results to previous findings. Given the inherent data limitations associated with

deep-focus events, the point-based stacking method stands as a promising avenue to yield more accurate stress drop estimates. Therefore, our future work entails the implementation of this novel stacking approach for deep-focus earthquakes, offering a crucial step toward a deeper understanding of the underlying physical mechanisms driving such seismic events.

4.6 Figures - Chapter 4

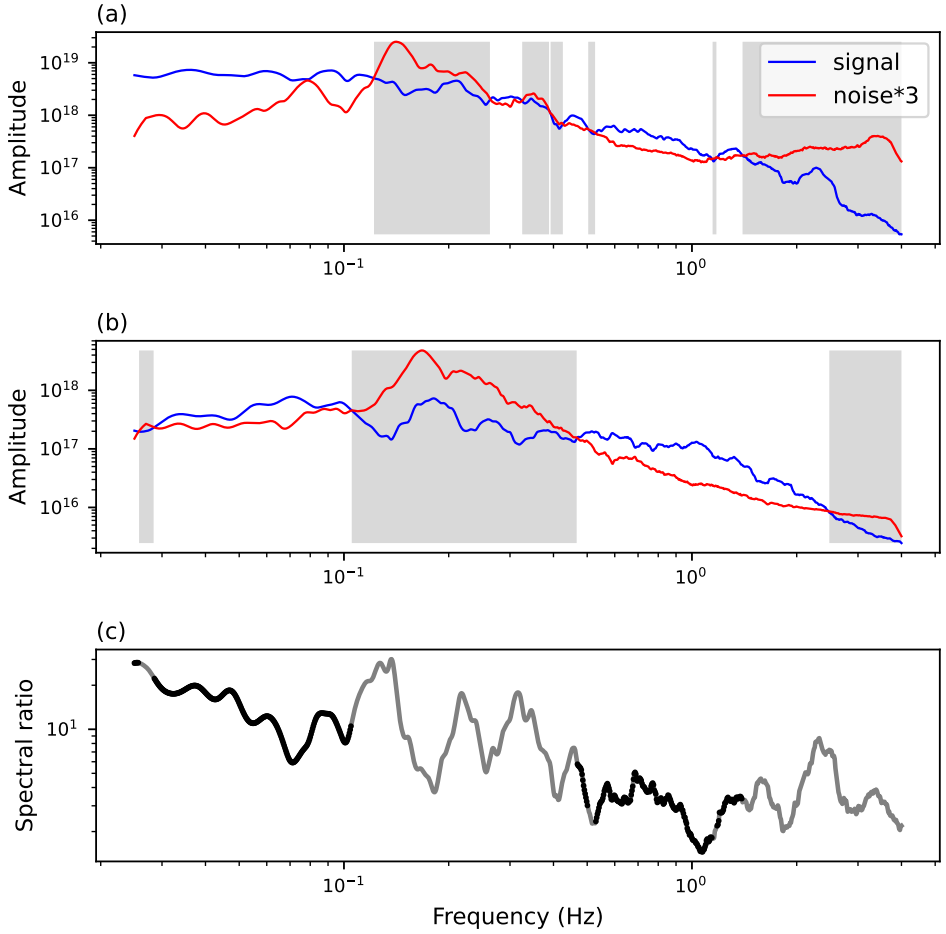

Figure 4.1: (a) Signal (blue) and noise (red) spectra for the master event. Shaded regions represent frequencies where the signal amplitude is less than three times the noise. (b) Signal (blue) and noise (red) for the eGf event. (c) Signal spectral ratio. The grey line represents the entire frequency range used in the conventional trace-based stacking method, while the black points indicate frequencies where the signal-to-noise ratio exceeds 3 for both the master event and the eGf event, used in the point-based stacking method.

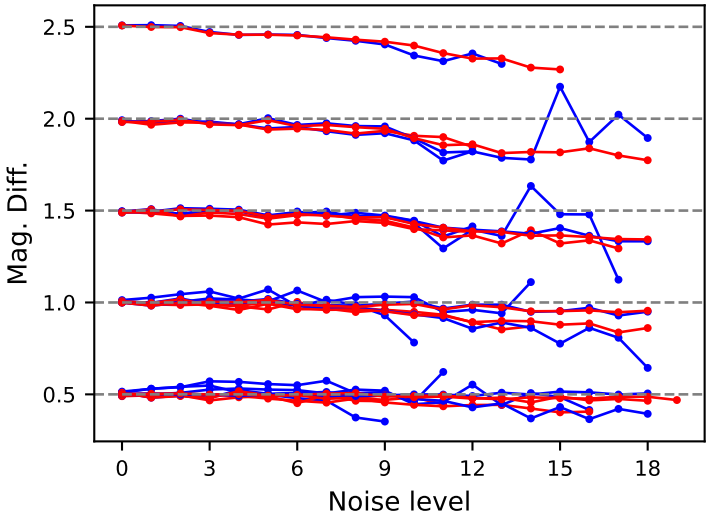

Figure 4.2: Estimates of magnitude difference between master events and eGf events using the conventional trace-based stacking method (blue lines) and point-based stacking method (red lines). The range of model magnitude difference spans from 0.5 to 2.5 in increments of 0.5, indicated by horizontal gray dashed lines. Note that the number of high-quality spectra meeting the criteria decreases as the noise level increases, so estimating results is unavailable at some higher noise levels due to a scarcity of spectra ratios.

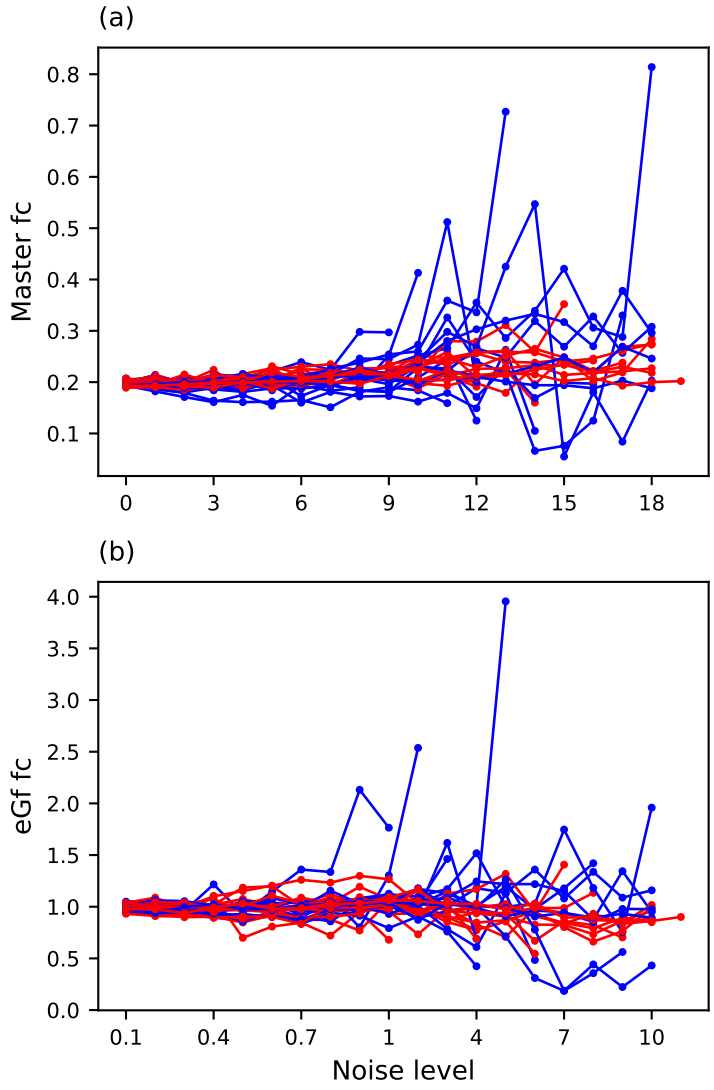

Figure 4.3: Estimates of master event corner frequency (a), and eGf event corner frequency (b) using the conventional trace-based stacking method (blue lines) and point-based stacking method (red lines). The master event corner frequency is consistently set at $f_M = 0.2$ Hz. The eGf corner frequency is set to $f_{eGf} = 1.0$ Hz. Note that the number of high-quality spectra meeting the criteria decreases as the noise level increases. Estimating results are unavailable at some higher noise levels due to a scarcity of spectra ratios.

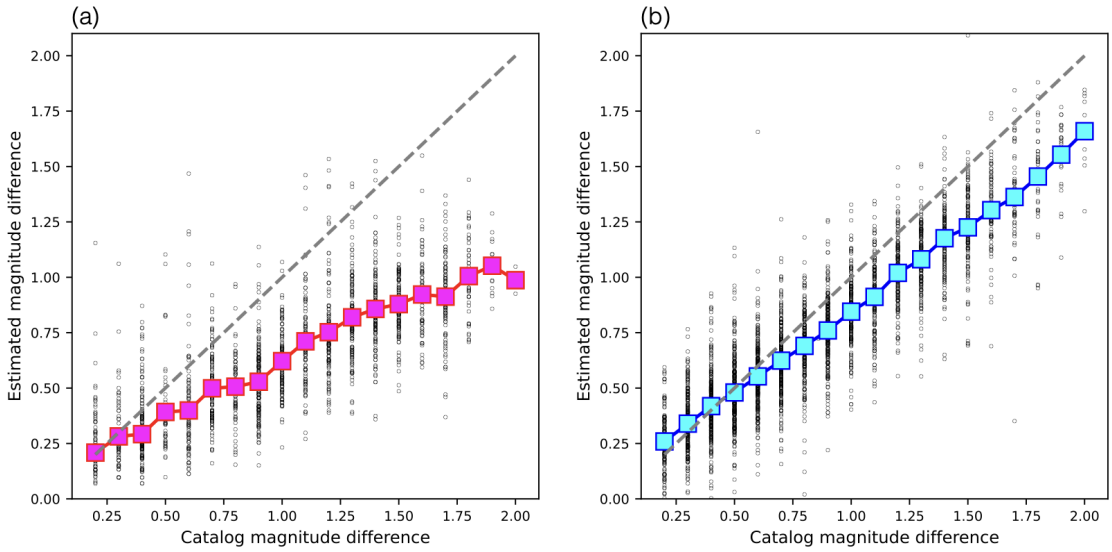

Figure 4.4: Estimated magnitude differences between master events and eGf events in relation to catalog magnitude differences, using the trace-based stacking method (a) and the point-based stacking method (b). The background gray circles represent individual estimations, while magenta and cyan squares denote the respective means at each 0.1 bin catalog magnitude difference. Dashed gray lines indicate instances where the estimated magnitude difference equals the catalog magnitude difference.

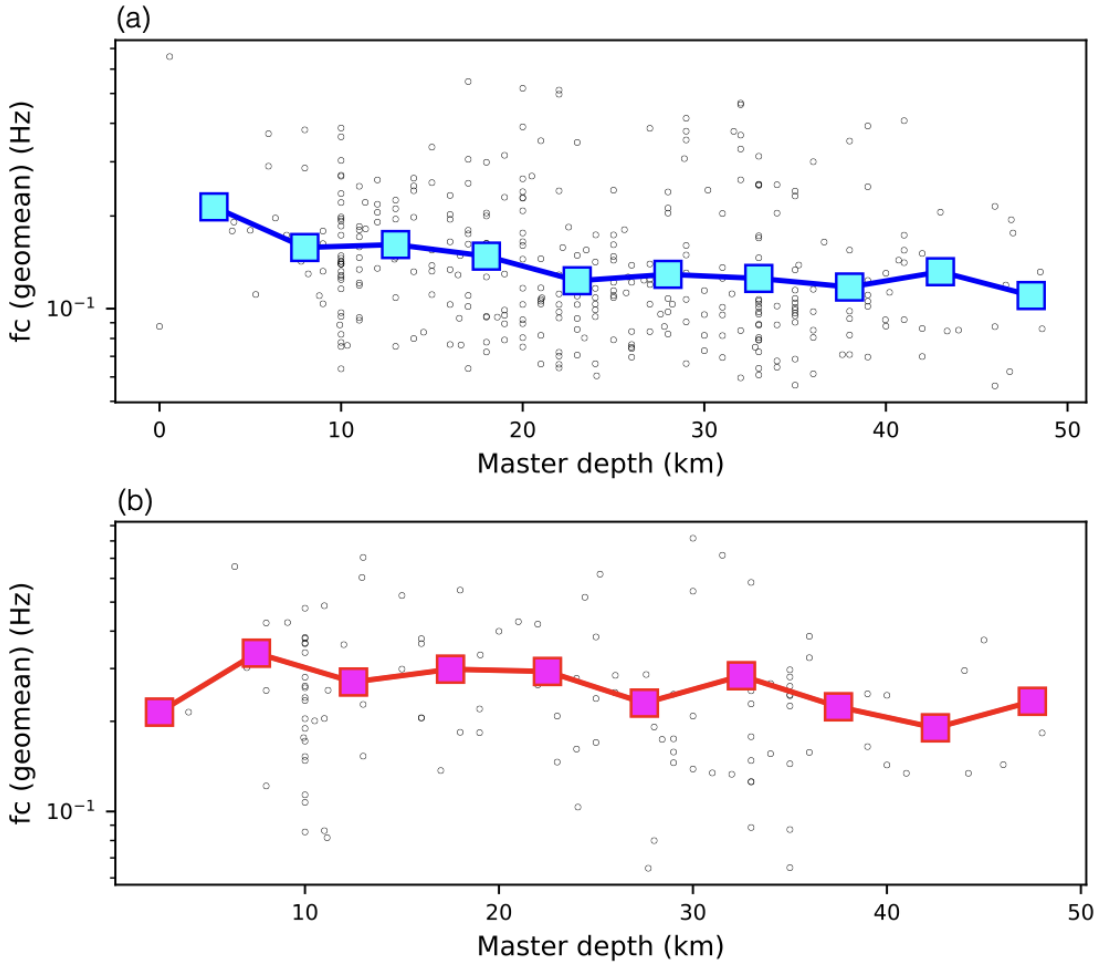

Figure 4.5: Estimated corner frequencies of master events in relation to depths of master events, using the trace-based stacking method (b) and the point-based stacking method (a). The background gray circles represent individual estimations, while magenta and cyan squares denote the respective means at each 5-km bin.

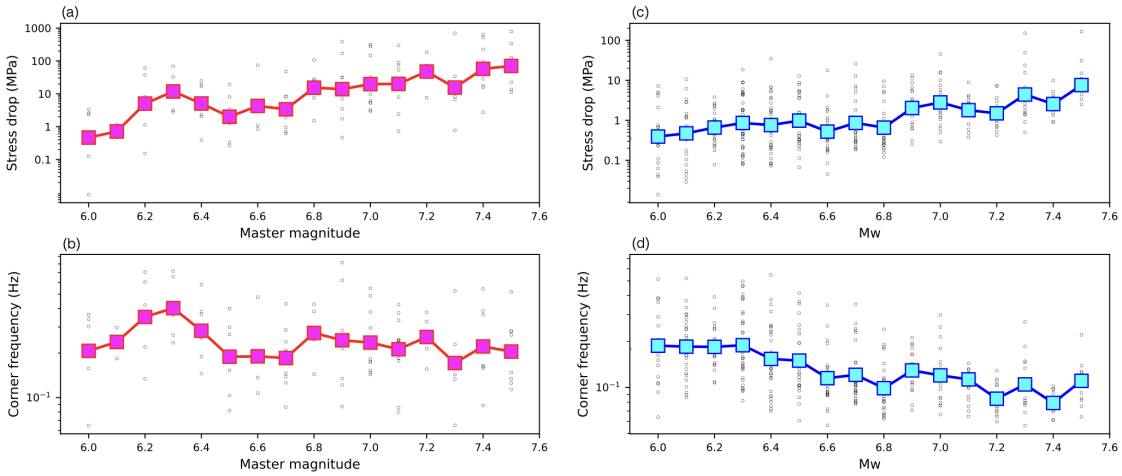

Figure 4.6: Estimated corner frequencies and stress drops of master events in relation to magnitudes of master events, using the trace-based stacking method (a, b) and the point-based stacking method (c, d). The background gray circles represent individual estimations, while magenta and cyan squares denote the respective means at each 0.1 magnitude bin.

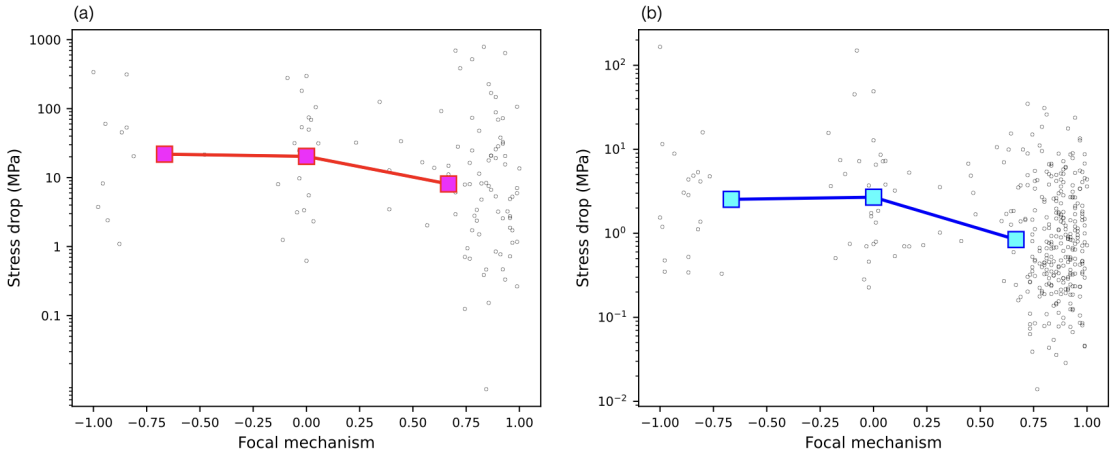

Figure 4.7: Estimated stress drops of master events in relation to focal mechanisms of master events, using the trace-based stacking method (a) and the point-based stacking method (b). The background gray circles represent individual estimations, while magenta and cyan squares denote the respective means.

CHAPTER 5

Influence of Shear Wave Velocity Heterogeneity on SH-wave Reverberation Imaging of the Mantle Transition Zone *

Abstract

Long-period ($T > 10$ s) shear wave reflections between the surface and reflecting boundaries below seismic stations are useful for studying phase transitions in the mantle transition zone (MTZ) but shear-velocity heterogeneity and finite-frequency effects complicate the interpretation of waveform stacks. We follow up on a recent study by *Shearer and Buehler* (2019) (hereafter SB19) of the top-side shear wave reflection Ssds as a probe for mapping the depths of the 410-km and 660-km discontinuities beneath the USArray. Like SB19, we observe that the recorded Ss410s-S and Ss660s-S traveltime differences are longer at stations in the western United States than in the central-eastern United States. The 410-km and 660-km discontinuities are about 40–50 km deeper beneath the western United States than the central-eastern United States if Ss410s-S and Ss660s-S traveltime differences are transformed to depth using a common-reflection point (CRP) mapping approach based on a 1-D seismic model (PREM in our case). However, the east-to-west deepening of the MTZ disappears in the CRP image if we account for 3-D shear wave velocity variations in the mantle according to global tomography. In addition, from spectral-element method synthetics, we find that ray theory overpredicts the traveltime delays of the reverberations. Undulations of the 410-km and 660-km discontinuities are underestimated when their wavelengths are smaller than the Fresnel zones of the wave reverberations in the MTZ. Therefore, modelling of layering in the upper mantle must be based on 3-D reference struc-

*Chapter 5 is published in *Geophysical Journal International*: Liu, Meichen, Jeroen Ritsema, and Carlos AM Chaves. "Influence of Shear Wave Velocity Heterogeneity on SH-wave Reverberation Imaging of the Mantle Transition Zone." Geophysical Journal International 231, no. 3 (2022): 2144-2155..

tures and accurate calculations of reverberation traveltimes.

5.1 Introduction

Recordings of long-period ($T > 10$ s) shear waves are useful data to map seismic discontinuities and velocity gradients in the mantle transition zone (MTZ, *Shearer* (e.g., 1990)). The mineral-phase transitions near depths of 410 and 660 km produce the highest amplitude shear wave reflections from the mantle after the ScS wave arrival (e.g., *Shearer*, 1990), before the SS arrival (e.g., *Flanagan and Shearer*, 1998), and between multiple ScS reflections (e.g., *Revenaugh and Jordan*, 1991) in stacks of transverse-component seismograms. We call these boundaries the '410-km discontinuity' and '660-km discontinuity' in this paper and define the MTZ as the layer of the mantle between the 410-km and 660-km discontinuities. The depths of the 410-km and the 660-km discontinuities and the thickness of the MTZ constrain the temperature and composition of the mantle (e.g., *Bina and Helffrich*, 1994; *Xu et al.*, 2008) and heat and mass transfer between the upper and lower mantle.

Most seismological studies of hundreds to thousands of waveforms are based on 1-D seismic reference profiles and ray theory to facilitate the analysis and computations. However, long-period shear waves are sensitive to seismic inhomogeneities in the mantle beyond the geometric ray so ray-theoretical calculations of traveltimes and waveform shifts may be inaccurate (e.g., *Tromp et al.*, 2005). Modelling inaccuracies have been discussed thoroughly for the SS wave and its precursors (e.g., *Neele et al.*, 1997; *Zhao and Chevrot*, 2003; *Bai et al.*, 2012; *Koroni and Trampert*, 2016, 2021; *Guo and Zhou*, 2020), but they exist for all long-period seismic wave reflections and conversions in the MTZ, including the multiple ScS reverberations (e.g., *Haugland et al.*, 2020) and receiver functions (e.g., *Deng and Zhou*, 2015).

The receiver-side shear wave reverberation in the upper mantle is the phase of interest in this paper. It has been introduced by *Shearer and Buehler* (2019), a study we abbreviate as SB19 from hereon, as a new wave type for probing the upper mantle and the MTZ. Using USArray waveforms and a common-reflection-point (CRP) imaging method, SB19 estimated the depths of the 410-km and 660-km discontinuities to be 40–50 km deeper beneath the western United States than beneath the central and eastern United The receiver-side shear wave reverberation in the upper mantle is the phase of interest in this paper. It has been introduced by SB19 as a new wave type for probing the upper mantle and the MTZ. Using USArray waveforms and a common-reflection-point (CRP) imaging method, SB19 estimated the depths of the 410-km and 660-km discontinuities to be 40–50 km deeper

beneath the western United States than beneath the central and eastern United States. This is an important study outcome as it implies that the seismic contrast in the upper mantle beneath the tectonically active western United States and tectonically stable central and eastern United States extends into the MTZ.

SB19 used ray theory and the 1-D iasp91 velocity model to relate traveltimes to reflector depths. They acknowledged that 3-D seismic velocity heterogeneity may have a significant effect on the amplitude, coherence, and depths of the 410-km and the 660-km discontinuities in the CRP images. In this paper, we follow up on their recommendation to investigate how 3-D velocity structure changes the interpretation of CRP imaging results and to test the hypothesis that the 410-km and 660-km discontinuities beneath the UNITED STATES are unperturbed. In Section 2, we confirm that the 410-km and 660-km discontinuities are 40–50 km deeper beneath the western United States than the central-eastern United States if the traveltime analysis is based on a 1-D reference structure. In Section 3, we explore how strongly 3-D shear-velocity inhomogeneities, as constrained by shear wave velocity tomography, perturb reverberation traveltimes and how ray-theoretical traveltime corrections change the CRP images. In Section 4, we use spectral-element method seismograms to evaluate the accuracy of ray theory in predicting the reverberation traveltimes and whether undulations on the 410-km and 660-km discontinuities are resolvable by long-period shear wave reflections (section 4). In section 5, we discuss our key findings.

5.2 Mapping the 410-km and 660-km Discontinuities by 1-D Common Reflection Point Imaging

5.2.1 The Ssds phase

A shear wave reverberation beneath the receiver is abbreviated here as 'Ssds', following the notation of SB19. Ssds is a shear wave that follows a similar path in the mantle as the direct S wave and reflects off the free surface and off the top of a reflector at depth d before it is recorded by a seismometer on the surface (Fig. 5.1). The arrival time of Ssds after S depends primarily on d and the shear wave speed above the reflecting layer. For PREM (*Dziewonski and Anderson*, 1981), an earthquake at the surface, and an epicentral distance of 80°, Ss410s and Ss660s arrive 159.6 and 242.2 s after S, respectively. Ssds can interfere with SS precursors but the two phases have different slownesses and are distinguishable in waveforms recorded over a wide epicentral distance range. The top-side reflection sdsS near the source has the same traveltime as Ssds at any distance for a 1-D velocity structure (Fig. 5.1). For stations at similar azimuths, source-side reflection points

are virtually identical whereas the Ssds reflection points are separated beneath the arrays of stations. Therefore, variations in the Ssds traveltime are primarily due to seismic structure in the uppermantle beneath the seismic stations. There is no source-side and receiver-side ambiguity if the analysis is limited to earthquakes deeper than the reflecting boundaries of interest (*Liu and Shearer*, 2021) but the data set would be significantly smaller.

5.2.2 USArray waveforms

To confirm SB19's imaging results, we analyse 59,517 transversecomponent displacement waveforms from 337 global earthquakes (Fig. 5.2) recorded by stations from the USArray and other regional networks in the 48 conterminous United States. The earthquakes are shallower than 35 km, so the direct S wave and the depth phase sS form a single pulse at long periods. The earthquakes have moment magnitudes smaller than 7.0 so rupture complexity does not affect long-period waveforms strongly. The epicentral distances are between 60° and 110° and waveforms have been filtered using a bandpass Butterworth filter with corner frequencies of 20 and 80 mHz. We align the waveforms on the peak S-wave displacement and normalize them, so the S waves have the same polarities and maximum displacements of $+1$. In all waveforms, the S-wave displacement is at least six times larger than the signal in the 100-s windowprior to the Swave onset. The maximum and the root-meansquare displacement in the window [30 s, 220 s] after the S-wave arrival time are more than six times and three times smaller than the peak S-wave displacement, respectively. We remove earthquakes with fewer than 20 seismograms left after these quality control steps.

A record section of the sum of thesewaveforms brings out Ss410s and Ss660s as the strongest mantle reflections (Fig. 5.3). The Ss410s and Ss660s have mean amplitudes of about 0.05 and are recorded without interference with ScS and SS at distances larger than 60° and 75°, respectively. The SS precursors S410S and S660S are weaker than Ss410s and Ss660s at distances smaller than 110° (e.g., *Shearer*, 1991). Although we cannot rule out that signals labeled 'A' and 'B' in Fig. 5.3(a) are side lobes due to the applied Butterworth filter, signal 'A' may be a SS-precursor reflection at a depth of about 125 km and signal 'B' may be a Ssds reflection from the lithosphere–asthenosphere boundary (LAB), a boundary that has also been studied with P-wave and S-wave receiver functions (*Rychert et al.*, 2007; *Abt et al.*, 2010; *Hopper and Fischer*, 2018) and multiple S-wave reflection (*Liu and Shearer*, 2021).

Ssds reflections from the uppermost lower mantle below the 660 arrive more than 250 s after S and do not interfere with SS and the S410S precursor at distances larger than 95° in region 'C' of Fig. 5.3(a). However, it is difficult to differentiate reflections below the

660 from shallower SS precursors because S waves are attenuated by diffraction around the core and the slowness resolution is poor. The high-amplitude signal about 330 s after S waves has a slowness of roughly 1.0 s deg^{-1} which is smaller than the slowness of any SS precursor. Its traveltime is similar to that of the phase Ss410s410s (i.e. the shear wave reverberation with two up and down shear wave segments between the surface and the 410-km discontinuity) and the phase PSs660s (i.e. the PS phase with an additional top-side reflection off the 660-km discontinuity). However, it is unlikely that these phases can be recorded with high amplitudes on transverse component records.

5.2.3 Common reflection point imaging

By 1-D common reflection point (CRP) mapping, we convert the Ssds-S difference times to the locations of the Ssds reflecting points in the upper 800 km of the mantle beneath the USArray. We use the TauP software (*Crotwell et al.*, 1999) and the PREM velocity structure to calculate Ssds reflection points and traveltimes. At a depth d, 1716 reflection points are uniformly distributed on a $1^\circ \times 1^\circ$ horizontal grid between 25°N and 50°N and between 130°E and 65°E. The horizontal grids are separated by 5 km from 10 to 1000 km, for a total of 199 depths. For a gridpoint X, we select waveforms for which the Ssds reflection points are within the $1^\circ \times 1^\circ$ bin around X and for which the theoretical Ssds arrival time differs more than 15 s from the theoretical arrival times of sS, ScS and sScS, and more than 50 s from the arrival time of SS to avoid wave interference. If fewer than five waveforms are available, we deem the mean displacement of Ssds to be inaccurately determined.

Since we use shallow focus earthquakes, the source-side and the receiver-side reflections have identical traveltimes. From synthetic seismograms for PREM, we have verified that they are equally strong so we attribute half of the mean Ssds amplitude to a source-side reflection. To construct the CRP images, we estimate sourceside reflections of the 337 earthquakes and receiver-side reflections for the 1716 gridpoints sequentially following two steps. First, we determine the mean of the Ssds displacement for each earthquake at the theoretical arrival time of Ssds. We assume that the mean displacement source-side reflection has been amplified and that receiver-side structures do not contribute coherent signals. Secondly, we subtract this mean value from the Ssds displacement of each waveform, assuming that the residual displacement to be due to coherent reflections beneath the USArray. We exclude events with fewer than 20 seismograms. After mapping the Ssds signals onto the grid ray theoretically, we average the receiver-side reflection amplitudes with $1^\circ \times 1^\circ$ bins, which are narrower than the Fresnel zones of 10-s period Ssds reflections

in the mantle transition zone, as shown by SB19. We have also implemented the approach by SB19, who estimates the source-side and receiver-side contributions to Ssds in one step using a sparse-matrix inversion solver. This approach yields smaller amplitudes of the Ssds reflections but the overall character of the CRP image, including the depths of the 410-km and 660-km discontinuities, are similar (Fig. 5.12).

Fig. 5.4(a) shows a vertical section of the CRP image along the 40°N parallel. As expected from Fig. 5.3, the 410-km and 660-km discontinuities are the clearest reflectors. Variations of the Ss410s-S and Ss660s-S difference times project as spatial variations in the depth of 410-km and 660-km discontinuities. The 410-km and 660-km discontinuities are deeper and more complex beneath the western United States (west of -100°E) than beneath the central and eastern United States. This is also apparent in other sections through the CRP images shown in Fig. 5.15. The 410-km discontinuity is strongest between longitudes -100°E and -75°E. The 520-km discontinuity may be responsible for a relatively weak Ssds reflection between the 410-km and 660-km discontinuities. The CRP images near the 410-km and 660-km discontinuities west of -100°E are complex, which was also noted by SB19. Strong reflectors corresponding to the Ssds signals in region B of the record section of Fig. 5.3 are mapped at about 100 and 150 km depth, but their depths and strengths vary. The incoherent structures at depths larger than 800 km are most likely imaging artifacts because these structures correspond to the amplified signals in region C of Fig. 5.3, where S are diffracting waves and the slowness resolution is relatively poor.

Fig. 5.4(b) shows maps of the depth of the 410-km discontinuity and the thickness of the MTZ. These are estimated from the absolute minimum values of the mean displacements in the CRP image in the depth ranges of 350–470 km (for the 410-km discontinuity) and 620–730 km (for the 660-km discontinuity) by cubic spline interpolation. We do not estimate the depth of the 410-km and 660-km discontinuities where a secondary absolute minimum is stronger than 40 percent of the absolute minimum in these depth ranges. The depth of the 410-km discontinuity varies by 40–50 km. The 410-km discontinuity is deepest beneath the southern Basin and Range and the Colorado Plateau and shallowest beneath the central plains and the Atlantic coast. The thickness of the MTZ varies less than 10 km because the 410-km and 660-km discontinuities depth variations are similar. The MTZ is thinnest beneath California and thickest beneath the Southern Rocky Mountains and the Colorado plateau. The MTZ thickness is anomalous in small regions near the margins of our model domain. This includes the extremely thin (210 km) MTZ beneath the west coast of central California which was also resolved by SB19. However, the CRP images have low resolution here because the data coverage is poor.

SB19 resolved similar maps as Fig. 5.4(b), indicating that our and SB19's data sets

contain consistent variations of the Ss410s-S and Ss660s-S difference times and that estimates of the depths of the 410-km and 660-km discontinuity do not strongly depend on the applied mapping method.

The S410S and S660S precursors interfere with the reverberations (Fig. 5.3). To test their influence, we compare CRP images with and without seismograms for which the reflecting time falls within 50 s of either of the precursors (Fig. 5.16). The maps of the depth of the 410-km discontinuity and the MTZ thickness are similar so interference with precursors has a minor effect on the imaging results. The large difference near the Pacific coast is due to lack of data coverage.

5.3 Influence of 3-D Seismic Heterogeneity on the CRP Images

The map of the depth of the 410-km discontinuity shown in Fig. 5.4(b) is reminiscent of the estimated shear wave velocity variations in the upper mantle beneath the United States from the modelling of regional S waves (e.g., *Grand and Helmberger*, 1984), surface waves (e.g., *Van der Lee and Nolet*, 1997) and, more recently, ambient noise (e.g., *Bensen et al.*, 2008), P-wave polarization (*Park et al.*, 2019) and surface wave amplification (*Eddy and Ekström*, 2014; *Bowden and Tsai*, 2017). This indicates strongly that shear-velocity variations in the mantle affect Ss410s-S and Ss660s-S difference times and that a mapping method based on a 1-D velocity structure would overestimate undulations of the 410-km and 660-km discontinuities.

5.3.1 S-wave traveltime variations

Fig. 5.5(a) shows how shear wave velocity variations in the crust using CRUST1.0 (*Laske et al.*, 2013) and in the upper mantle affect the traveltimes of S waves. Plotted are the average S-wave delay with respect to the PREM velocity model of at least five S waves recorded at seismic stations from the USArray. The delay times have been corrected for 'source terms', representing the effects of a potential mislocation of the earthquake location and origin time on the absolute S-wave traveltime. S waves recorded by USArray stations in the western United States (the tectonically active region) arrive on average 5–6 s later than at stations in the central and eastern United States (the stable platform). The global-scale mantle models S40RTS (*Ritsema et al.*, 2011), SEMUCB-WM1 (*French and Romanowicz*, 2014) and TX2015 (*Lu and Grand*, 2016) predict a similar traveltime pattern (Fig. 5.5b–d) but the range is slightly smaller than in the data (Fig. 5.5e). Our calculations indicate

that the crustal structure from CRUST1.0 enhances the east–west contrast only slightly, so wave speed variations in the mantle are primarily responsible for the S-wave traveltime differences.

The imperfect match between the recorded and the predicted S-wave traveltime is expected because tomographic models do not perfectly explain the recorded traveltime variation of any shear wave (e.g. *Ritsema et al.*, 2004). Nevertheless, it is obvious that shear-velocity heterogeneity affects teleseismic S-wave traveltimes across the USArray. Since Ssds has two additional propagation legs through the upper mantle, the Ss410s-S and Ss660s-S difference times are likely to be double the variation shown in Fig. 5.5(a) due to shear velocity heterogeneity only. If shear wave speed variations in the upper mantle beneath North America are ignored in the modelling, a variation of the Ss410s-S and Ss660s-S difference times of more than 10 s would imply that the depths of the 410-km and 660-km discontinuities vary by about 18 and 20 km or more. This is of the same magnitude as resolved in Fig. 5.4.

5.3.2 Ray-theoretical corrections

Since the tomographically predicted S-wave traveltime variation of 5–6 s across the USArray is a significant fraction of the recorded traveltime variation, we suspect that shear-velocity variations in the upper mantle influence the CRP imaging and our estimate of the depth of the 410-km discontinuity. To quantify this, we determine the CRP image for 'corrected' Ssds-S difference times. From the measured Ssds-S difference time, we subtract the predicted difference time anomaly (positive or negative) by shifting the waveform around the theoretical Ssds arrival time. We predict the Ssds-S difference time by ray tracing through tomographic model S40RTS for the mantle and CRUST1.0 for the crust. The Ssds-S difference time predictions are similar for SEMUCB-WM1 and TX2015, as expected from Fig. 5.5.

Fig. 5.6(a) shows the CRP image along the 40°N parallel after traveltime corrections. The character of the corrected (Fig. 5.6) and uncorrected (Fig. 5.4) CRP images are the same, but the 410-km and 660-km discontinuities are flatter boundaries across the USArray. This is especially clear for the region between -100°E and -80° where the 410-km and 660-km discontinuities are relatively simple. Fig. 5.6(b) emphasizes that the depth variation of the 410-km discontinuity is much smaller when the CRP image is based on tomographically corrected Ssds-S difference times. The 410-km discontinuity is not deeper in the west than in the east. The thickness of the MTZ in the corrected and uncorrected images are similar because shear velocity variations are relatively weak in the MTZ compared to the

uppermost mantle. The histograms shown in Fig. 5.6(c) illustrate that the depth variation of the 410-km discontinuity is about a factor of two smaller when traveltime corrections have been applied to the data and that the corrections do not change the range in MTZ thickness values. The traveltime corrections change the mean depth of the 410-km and 660-km discontinuities by about 10 km, which is similar to the change obtained by SB19 using ray-theoretical corrections computed for a regional 3-D velocity model.

The ray-theoretically corrected images may not reflect the actual depth variations of the 410-km discontinuity. Since S40RTS and any other tomographic model does not perfectly explain the recorded S-wave traveltime variation (Fig. 5.3), it is unlikely that the traveltime corrections have completely removed the effects of the shear-velocity structure on the CRP image. Furthermore, we show in the next section that ray-theoretical predictions of long-period Ssds-S traveltimes are inaccurate and that corrections can project as spurious signals in the CRP images.

5.4 Resolution Tests Using Spectral-Element-Method Waveforms

We analyse synthetic waveforms to test the robustness of our CRP imaging approach, the resolution of 410-km and 660-km discontinuities undulations from long-period Ssds waveform data, and the accuracy of ray-theoretical corrections. The waveforms are computed using the SPECFEM3D-Globe software (e.g., *Komatitsch and Tromp*, 2002; *Komatitsch et al.*, 2016) modified by us to allow for undulations of the 410-km and 660-km discontinuities. The eight test structures are PREM, S40RTS (Fig. 5.7a), SEMUCB-WM1, TX2015 and structures T2, T5, T8 (Fig. 5.7b) and T5-410-S40. The simulations account for Earth's ellipticity and anelasticity using the Q structure of PREM. In each structure, the density and velocities in the uppermost mantle extend to the surface. We remove the crust from seismic models to suppress reverberations in the crust that complicate the waveforms following the S wave (Fig. 5.16).

The 1-D PREM structure with discontinuities at 220, 400 and 670 km depth serves as a baseline model for determining artefacts in the CRP images unrelated to 3-D structure in the uppermantle. In our calculations, S40RTS, SEMUCB-WM1 and TX2015 represent models of the 3-D shear velocity structure in the mantle. We do not include the crustal structure, adopt PREM as the reference mantle structure for each of the three models, and assume the Voigt average shear-velocity variations in the anisotropic SEMUCB-WM1 model. The 220-km, 410-km and 660-km discontinuities are horizontal boundaries at the same depths

as in the PREM model. Models T2, T5 and T8 have the same layered velocity structure as PREM but the 410-km and the 660-km discontinuities are sinusoidal boundaries with amplitudes of 15 km and wavelengths of 2°, 5° and 8°, respectively. The undulations of the 410-km and 660-km discontinuities are oppositely directed so the thickness of the MTZ varies up to 30 km with respect to the average of 270 km. The model T5-410- S40 has the 3-D shear velocity structure of S40RTS and sinusoidal undulations of the 410-km discontinuity with a wavelength of 5°. The 660-km discontinuity is a horizontal boundary in T5-410-S40.

For each of the eight structures, we compute waveforms at periods longer than 10 s for 462 stations in a rectangular $2° \times 2°$ grid between longitudes 130○–65°W and latitudes 25°–50°N (Fig. 5.7c). We calculate waveforms for 12 earthquakes uniformly distributed at a distance of 75° from [-100°E, 40°N]. We use 48 earthquakes distributed in a spiral for structure T2. All earthquakes have the same dip-slip source mechanism (source parameters for event 08 0596 G in the Global CMT catalogue) to ensure strong radiation of SH waves to teleseismic stations. The uniform data coverage is sufficient to investigate the effects of velocity heterogeneity on Ssds-S traveltimes and the resolution of undulations of the 410-km and 660-km discontinuities using long-period Ssds reflections. Because of the high computational cost, we cannot afford to reproduce the source-station combinations in the data and, therefore, we cannot estimate CRP mapping artefacts due to inhomogeneous slowness and azimuthal sampling.

5.4.1 Testing ray-theoretical traveltime corrections

Fig. 5.8 shows the CRP images along the 35°N parallel in the central region of the model domain determined for the PREM and S40RTS models. Fig. 5.13 shows similar CRP images for SEMUCB-WM1 and TX2015. The CRP image for PREM in Fig. 5.8(a) is the ideal case as the assumed velocity structure of the mantle is identical to the structure used to calculate traveltimes and ray paths. Artefacts are entirely due to the implementation of the CRP mapping procedure, the limited frequency band of the waveforms, and wave interference. PREM's velocity discontinuities at 220, 400 and 670 km depth are resolved about 10 km shallower in the mantle because the crust is not included in the waveform computations. Since the waveforms are computed for periods longer than 10 s and since shear wave speed increases with depth, reflectors at larger depths are more stretched than at shallower depths. The imaged 660-km discontinuity is therefore only about 60 percent stronger than the imaged 410-km discontinuity even though the impedance contrast at the 660 is a factor of two stronger than at the 410-km discontinuity. The CRP image derived

from PREM waveforms is mostly free of artificial layering between 150 and 750 km depth. The side lobes of the 660 near -65°E are artefacts near the boundaries of the station grid. Layering near 100 km depth, which is especially strong near the centre of the CRP image, shows that the Ssds reverberation is not an ideal wave type for imaging the uppermost mantle. The arch-shaped structure below 750 km depth is likely the projection of shallow SS precursors misinterpreted as Ssds reflections deep in the transition zone as discussed in Section 2.1.

The CRP image derived from S40RTS waveforms is more complex (Fig. 5.8b). The 410-km and 660-km discontinuities deepen from east to west because S40RTS predicts that Ssds traveltimes through the upper mantle are shorter beneath the central and eastern United States than beneath the western United States and we use the PREM velocity structure to convert traveltimes to reflector depths. The velocity heterogeneity in S40RTS causes misalignments of Ssds signals and therefore fluctuations in the strength of the 410-km and the 660-km discontinuities from west to east by up to a factor of two. For example, the 660 appears as a relatively weak reflecting boundary between longitudes -120°E and -110°E, near the transition between the low-velocity upper mantle of the western United States and the high-velocity upper mantle beneath the central United States. In addition, spurious reflectors are particularly strong between -120°E and -100°E, where horizontal gradients in the uppermost mantle are strongest. It is difficult to identify how complex wave propagation produced the complexity in the CRP image, but the CRP image based on USArray waveforms is also most complex for the western United States, and a tilted reflective structure in the upper mantle has been observed by SB19 in their data image, albeit with an eastward dip and a greater depth extent.

Fig. 5.8(c) shows the CRP image based on the S40RTS synthetics after applying ray-theoretical traveltime corrections following the procedure outlined in Section 4.3. The traveltime corrections do not remove, and may even amplify the CRP image artefacts for depths shallower than 100 km and deeper than 750 km. More significantly, the ray-theoretical calculations appear to overpredict the contribution of shear-velocity heterogeneity to the Ss410s-S and Ss660s-S traveltime differences. After traveltime corrections, the 410-km and 660-km discontinuities are projected shallower beneath the western United States than the central United States, opposite to the imaged depths of the 410-km and 660-km discontinuities prior to corrections.

The inaccuracy of ray theory in predicting the shear wave traveltime perturbations is illustrated further in Fig. 5.9. It shows the estimated depths of the 410-km discontinuity and the thickness of the MTZ based on the 1-D CRP method applied to synthetic waveforms computed for S40RTS. Fig. 5.14 shows that we obtain similar results for SEMUCB-WM1

and TX2015. The total variation in the depths of the 410-km discontinuity is about 15–20 km. As expected, the depth of the 410-km discontinuity (Fig. 5.9a) mimics the shear velocity variations in the upper mantle of S40RTS (Fig. 5.7a) and the S-wave traveltime delay map shown in Fig. 5.5. Variations in the thickness of the MTZ (Fig. 5.9b) of about 10 km are small compared to the depth variations of the 410-km and 660-km discontinuities because shear velocity variations in the MTZ are much weaker than in the uppermost mantle.

If ray-theoretical traveltime corrections are precise, we must expect that the CRP images of the ray-theoretical corrected S40RTS, SEMUCB-WM1 and TX2015 waveforms are similar to the CRP image for the PREM model because the 410-km and 660-km discontinuities are horizontal boundaries in all models. However, we find this not to be the case. While the elevation of the 410-km and 660-km discontinuities beneath the western United States (by 10 and 11 km, respectively) and their depressions beneath the central-eastern United States (by 11 and 12 km, respectively) have the expected trends, the corrections are larger than expected ray-theoretically. In the corrected image, the 410-km discontinuity is shallower in the western United States than in the eastern United States (Fig. 5.9c) opposite to the uncorrected CRP image (Fig. 5.9a). In the western United States, the inferred and predicted depth correction differ by a factor of 1.7. The MTZ thickness has a smaller variation than the depth of the 410-km discontinuity (Fig. 5.9c and d). After corrections, a larger area has a thickness within 265–275 km. The corrected Pacific coast changes from thicker to slightly thinner than the surrounding area, and the central United States has the largest thickening by about 15 km.

5.4.2 The resolution of undulations on the 410-km and 660-km discontinuities

Fig. 5.10 shows the depths of the 410-km and the 660-km discontinuities and the thickness of the MTZ resolved for models T2, T5, and T8. The checkerboard pattern of the undulations on the 410-km and 660-km discontinuities are resolved for T5 and T8 but the amplitude of the undulations is underestimated. The resolved thickness of the MTZ varies, on average, 12 km and 6 km less than in the original T8 and T5 models. The resolution of the undulations in T2 is poor despite using a larger set of waveforms for 48 earthquakes. From experiments, we have found that the resolution does not improve if we densify the grid of stations to a 1° spacing. Therefore, fluctuations of the depth of the 410-km or 660-km discontinuities with a wavelength of about 200 km are intrinsically unresolvable from long-period Ssds waveforms because the Fresnel zone of Ss410s and Ss660s in the upper

mantle at the dominant frequency of about 0.05 Hz is about 500 km, much wider than the undulations of the 410-km and 660-km discontinuities in T2.

Fig. 5.11 explores how undulations on the 410-km discontinuity would be resolved if they are embedded in 3-D velocity heterogeneity. We analyse waveform simulations for model T5-410-S40, described above. Fig. 5.11 shows the resolved depth variation of the 410-km and the 660-km discontinuities and the MTZ thickness before (in a, c and e) and after (in b, d and f) ray-theoretical traveltime corrections have been applied to remove the effects of shear-velocity heterogeneity on the traveltimes. Fig. 5.11(a) and (b) show that without traveltime corrections for 3-D heterogeneity, the resolved harmonic undulations of the 410 are overprinted by an east-to-west deepening. The ray-theoretical traveltime corrections remove the regional trend but the traveltime corrections do not accurately remove the effects of shear-velocity heterogeneity because the depth variations of the 410-km discontinuity are not perfectly resolved (compare Fig. 5.11b and 10d). The 660-km discontinuity. a horizontal boundary in T5-410-S40, is resolved with the same east-to-west deepening without traveltime correction. After traveltime corrections, the 660-km discontinuity does not have a distinct harmonic or tectonic structure but the topography indicates that the corrections are imperfect or that the effects of the 410-km discontinuity on the traveltimes may be projected as spurious 660-km discontinuity structures. As shown also in Fig. 5.9, the ray-theoretical corrections are too strong, but smaller than a factor of two (Fig. 5.9). The map of MTZ thickness, with a distorted checkerboard pattern, remains largely unchanged before and after the traveltime correction, though the checkerboard depth ranges become larger. The synthetic test of the joint effect of 3-D mantle structure and undulations on the 410-km discontinuity suggests that the MTZ thickness can be determined more robustly than the absolute depths of 410-km and 660-km discontinuities using the CRP imaging approach.

5.5 Discussion and Conclusions

The receiver-side S-wave reverberation, denoted as Ssds, is a useful data type to map the shear velocity structure in the upper mantle, including undulations of the 410-km and 660-km discontinuities of mineral phase transitions. Ssds complements SS precursor and P-to-S wave conversion (i.e. receiver function) imaging of the mantle because of its unique wave path geometry. In agreement with the analysis by SB19, we observe in record sections of waveform stacks that the Ss410s-S and Ss660s traveltime differences vary by up to 10 s across stations from the USArray. If the traveltime differences are attributed entirely to undulations on the 410-km and 660-km discontinuities, it implies that the 410-km and

660-km discontinuities are 40–50 km deeper beneath the western United States than the central and eastern United States. In turn, this would mean that the contrast between the tectonically active western United States and the stable central and eastern United States persists as a temperature or compositional contrast in the mantle transition zone and that there is a link between uppermost mantle and mantle transition zone dynamics.

However, the correlation between the resolved depth of the 410-km discontinuity (and the 660-km discontinuity) and tomographic maps of the shear-velocity structure in the upper mantle is high. This indicates that velocity heterogeneity in the uppermost mantle contributes significantly to the Ss410s-S and Ss660s-S traveltimes and the spatial variations of the depth of the 410-km discontinuity inferred from CRP imaging. Ray-theoretical corrections of traveltimes for velocity heterogeneity by shifting segments of the waveforms containing Ss410s and Ss660s prior to CRP stacking reduce the variation in the depth of the 410-km discontinuity by a factor of two.

For at least two reasons we find ray-theoretical corrections imprecise. First, seismic tomography has uncertainties. Global models S40RTS, SEMUCB-WM1 and TX2015 agree on the east–west contrast but disagree on the magnitude of the traveltime perturbations (Fig. 5.4). Each model underestimates the S-wave traveltime delay at USArray stations (Fig. 5.5) which is consistent with the fact that tomographic models underestimate the magnitude of traveltime and waveform perturbations. Hence, the effect on the estimated depths of the 410-km and 660-km discontinuities depends on the chosen tomographic model. SB19 notes that the traveltime corrections may introduce incoherence in the CRP images and use that as a factor in determining the value of traveltime corrections.

Second, our experiments with spectral-element method synthetics demonstrate that ray-theoretical predictions of the Ss410s-S and Ss660s traveltime differences are inaccurate. CRP images derived from waveforms computed for a mantle with 3-D velocity heterogeneity and horizontal phase boundaries show the expected deepening of the 410-km and 660-km discontinuities below the western United States and shallowing beneath the central and eastern United States where the shear velocities are relatively low and high, respectively. After applying traveltime corrections for the 3-D wave speed structure, the 410 and 660 remain undulating boundaries. In fact, the 410-km and the 660-km discontinuities in the corrected CRP image are deeper beneath the central-eastern United States than beneath the western United States, opposite to the uncorrected CRP image. This indicates that ray theory overpredicts the Ssds-S difference time by about a factor of two. This is the case for S40RTS, SEMUCB-WM1 and TX2015 and presumably also finer-scale regional tomographic models when finite-frequency effects are stronger. The inaccuracy of ray-theoretical predictions of the traveltime perturbations of long-period waves has been

studied previously. For example, *Neele et al.* (1997) and *Zhao and Chevrot* (2003) have pointed out that for the broad SS sensitivity kernels at the reflection points on the surface or the mantle discontinuities. *Bai et al.* (2012) and *Koroni and Trampert* (2016) illustrate how the finite wave effects affect CRP images built from SS precursors similarly to the study here.

Finally,we note that the resolution of the depths of the 410-km and 660-km discontinuities depends on spatial scales of the undulations. Our experiments with spectral element method synthetics indicate that the Ssds-S traveltime difference is sensitive to $5^\circ \times 5^\circ$ and $8^\circ \times 8^\circ$ sinusoidal variations of the depths of the 410-km and 660-km discontinuities albeit that the height of the undulations is underestimated. Spatial variations of the 410-km and 660-km discontinuities on a $2^\circ \times 2^\circ$ scale are not resolvable because such variations are smaller than the width of the Fresnel zone of Ssds at a period of 10 s.

Although it is beyond the scope of this work, it is better to simultaneously estimate the topography of the 410-km and 660-km discontinuities and shear velocity heterogeneity in the mantle of multiple data sets (e.g., *Gu et al.*, 2003; *Moulik and Ekström*, 2014) using finite-frequency kernels that relate waveform perturbations to velocity heterogeneity and phase boundary topography (e.g., *Guo and Zhou*, 2020) or, preferably, using an adjoint tomography approach (*Koroni and Trampert*, 2021). Based on our experiments, the evidence for large-scale variations of the depth of the 410-km discontinuity beneath the USArray is weak. As is well established, estimates of the thickness of the MTZ are not affected strongly by shear velocity heterogeneity. We find the thickness of the MTZ to vary by about 10 km, which is consistent with the receiver-function study of USArray data by *Gao and Liu* (2014) and much smaller than global variations of the MTZ observed in SS precursors studies (e.g., *Flanagan and Shearer*, 1998; *Chambers et al.*, 2005).

5.6 Figures - Chapter 5

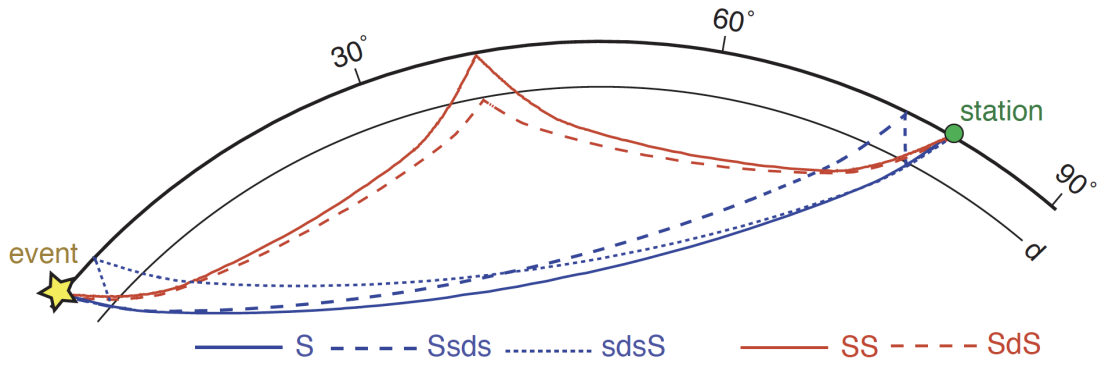

Figure 5.1: Ray diagram of the phases S (solid blue line), Ssds (dashed blue line), sdsS (dotted blue line), SS (solid red line) and the SS precursor SdS (dashed red line) for an epicentral distance of 80°.

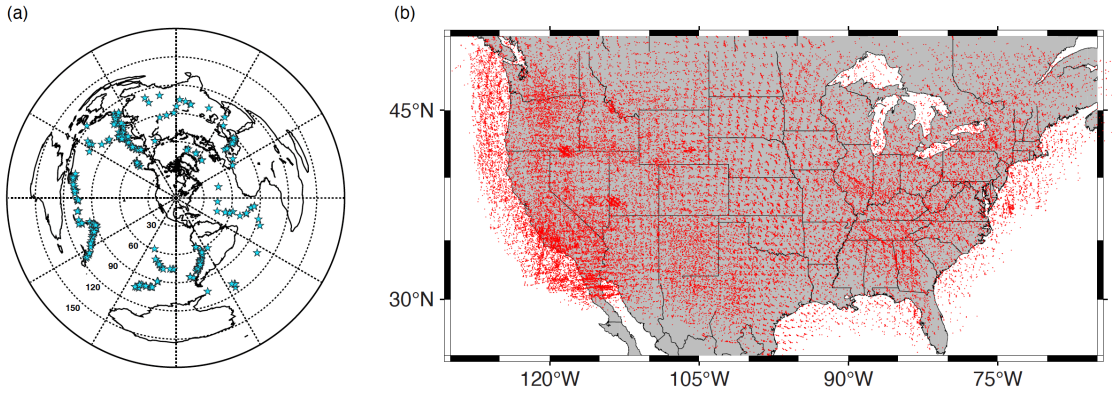

Figure 5.2: (a) Epicentres of earthquakes (stars) used in this study. The dashed circles have a common centre of [40°N, -95°E] and radii of 30°, 60°, 90°, 120° and 150°. (b) Red dots show reflecting points of Ss410s at the 410-km discontinuity for the 59 517 seismograms in our data set.

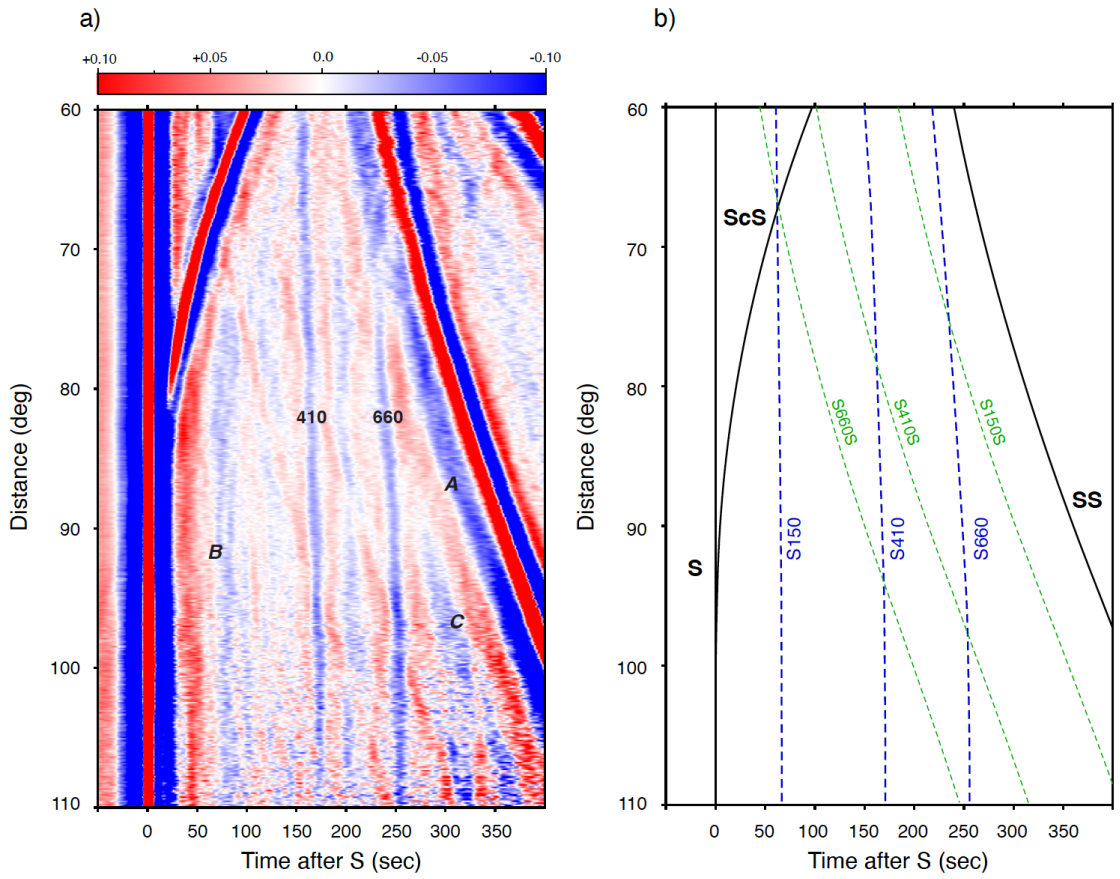

Figure 5.3: (a) Record section of transverse component seismograms used in this study. Shown is the amplitude of ground displacement in red and blue for positive and negative polarities, respectively, with a colour intensity proportional to the absolute value. The seismograms have been aligned to the S wave at time 0. (b) The arrival times of S, ScS and SS (black lines), S150, S410 and S660 (blue dashed lines), and the SS-precursors S150S, S410S and S660S (green dashed lines) have been computed for PREM for a source depth of 20 km.

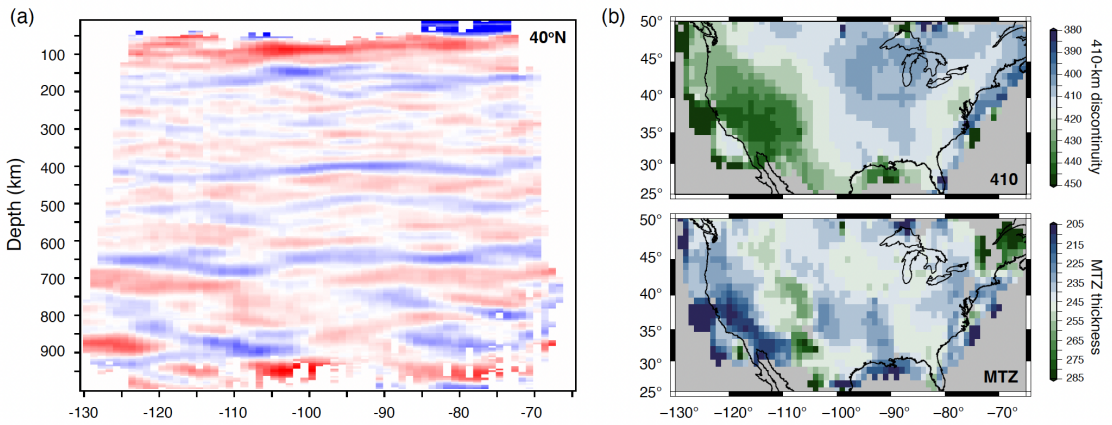

Figure 5.4: (a)Vertical section of the CRP image along 40°N. Blue and red colors indicate reflectors with positive and negative impedance contrasts, respectively. The color intensity is highest when the impedance contrast is strongest. All record section profiles use this color scale. (b) Depth of the 410-km discontinuity (top panel) and the thickness of the mantle transition zone (bottom panel).

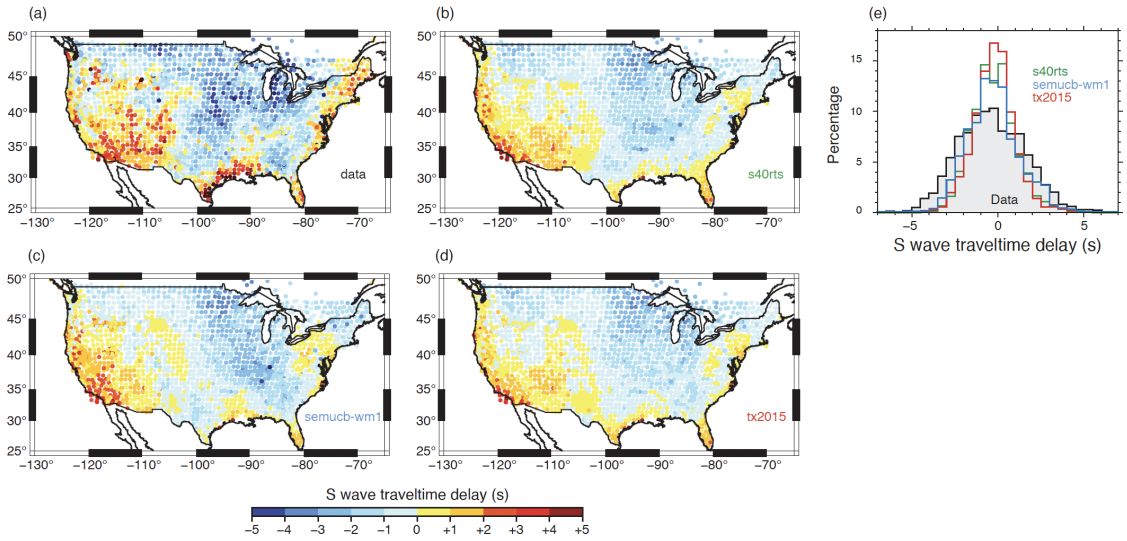

Figure 5.5: The recorded (a) and predicted (b, c, d) travel time delays of S waves by tomographic mantle models S40RTS (in b), SEMUCB-WM1 (in c), and TX2015 (in d) with crustal model CRUST1.0. Each circle indicates the location of a seismic station. Its color indicates the mean of the S-wave traveltime delays to the PREM model for at least five S waves. (e) Histograms of the S-wave traveltime delay in the data (grey fill) and predictions by S40RTS (green line), SEMUCB-WM1 (blue line), and TX2015 (red line) for the stations in panels (a)–(d).

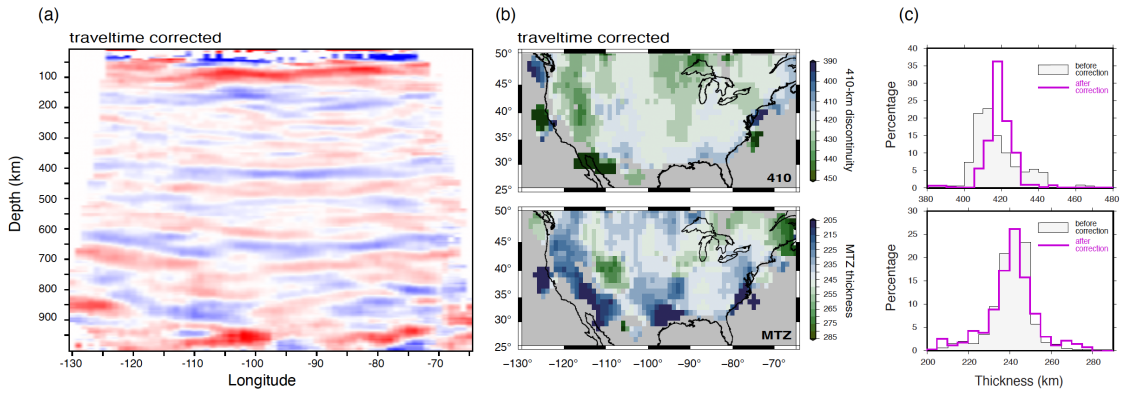

Figure 5.6: Depth of the 410-km discontinuity (in a) and the thickness of the transition zone (in b) estimated after ray-theoretical traveltime corrections have been applied. The color scale in a is the same as in Fig. 4(a). Panels (c) and (d) show histograms of the resolved depth of the 410-km discontinuity and the thickness of the MTZ beneath the USArray with (black line) and without (purple line) traveltime corrections. Compare with Fig. 4(b).

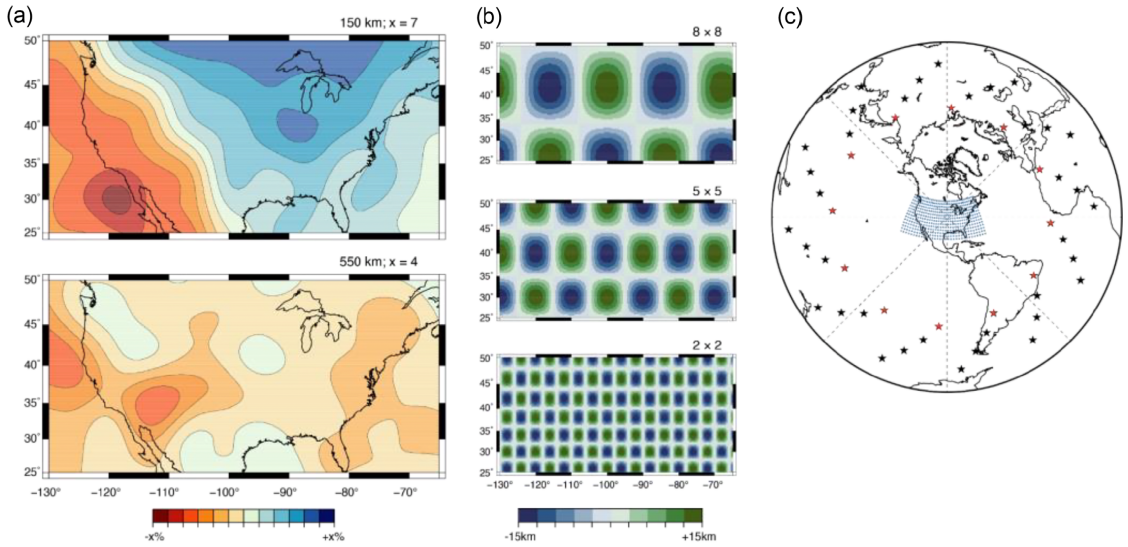

Figure 5.7: (a) Maps of the shear-velocity variation at (top) 150 km and (bottom) 500 km depth according to S40RTS. The east–west contrast across the United States is similar for SEMUCB-WM1 and TX2015. (b) Harmonic undulations of the 410-km and 660-km discontinuities for (from top to bottom) models T8, T5, and T2 with spatial wavelengths of 8°, 5°, and 2°. (c) Distribution of hypothetical earthquakes (stars) and stations (circles). For models PREM, S40RTS, T8, and T5 we compute waveforms for the twelve earthquakes indicated by red stars. For T2, we compute waveforms for these earthquakes and the additional 36 earthquakes indicated by black stars.

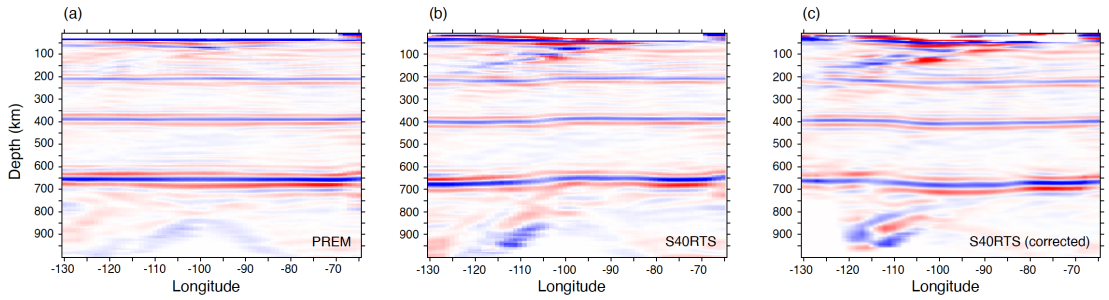

Figure 5.8: CRP images along the 35°N parallel determined for (a) PREM synthetics, (b) S40RTS synthetics and (c) S40RTS synthetics after ray-theoretical corrections have been applied. The color scale is the same as Fig. 4(a).

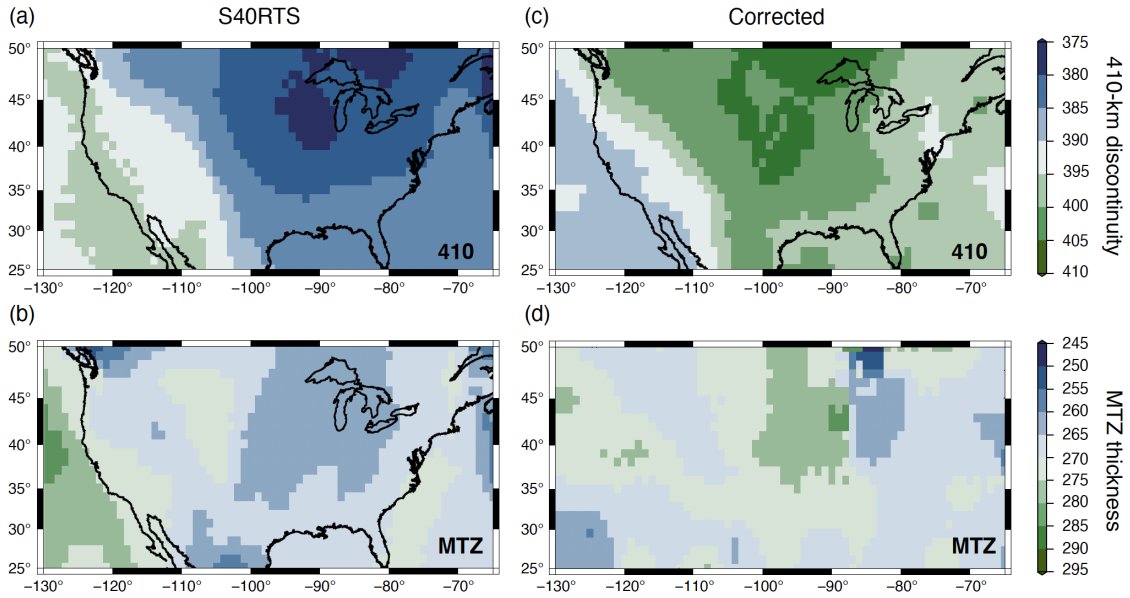

Figure 5.9: Depths of the 410-km discontinuity (top row) and the thicknesses of the transition zone (bottom row). Panels (a) and (b) are estimated from spectral-element-method seismograms calculated for model S40RTS. Panels (c) and (d) show the same estimates after ray-theoretical corrections have been applied to the waveforms.

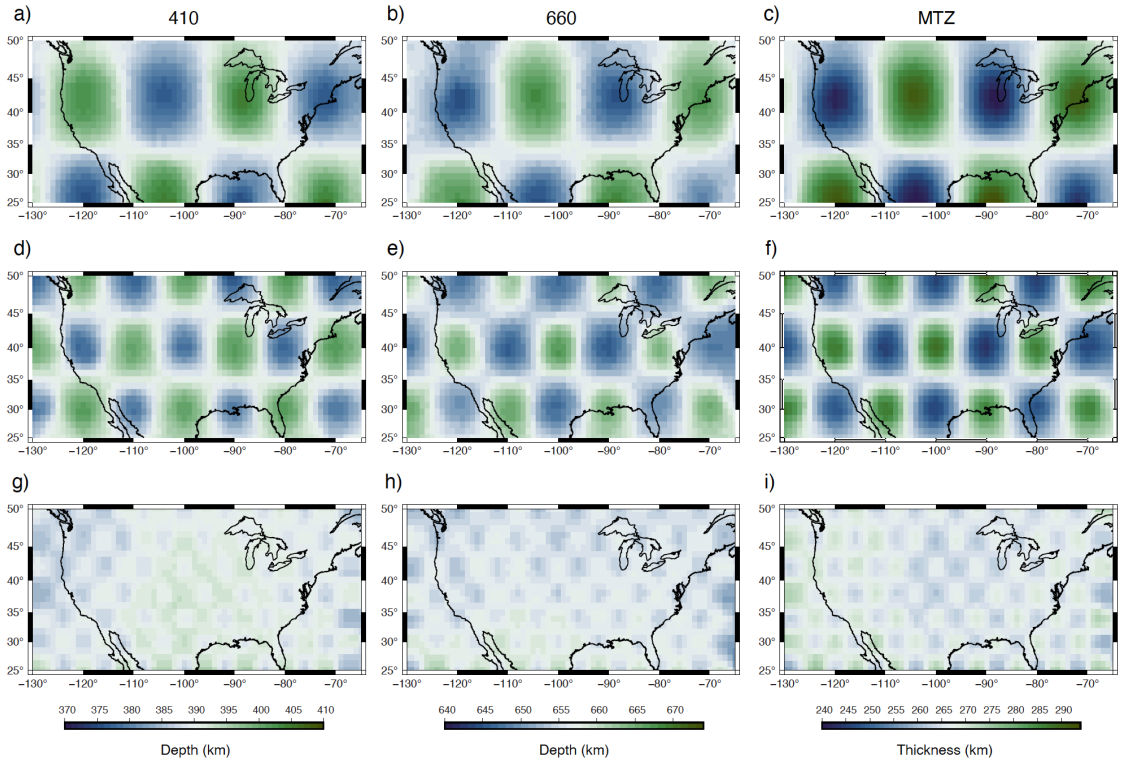

Figure 5.10: Depth maps of the 410-km, 660-km discontinuities, and MTZ thickness using the CRP imaging method for $8° \times 8°$ (a, b, c), $5° \times 5°$ (d, e, f) and $2° \times 2°$ (g, h, l) input topography models.

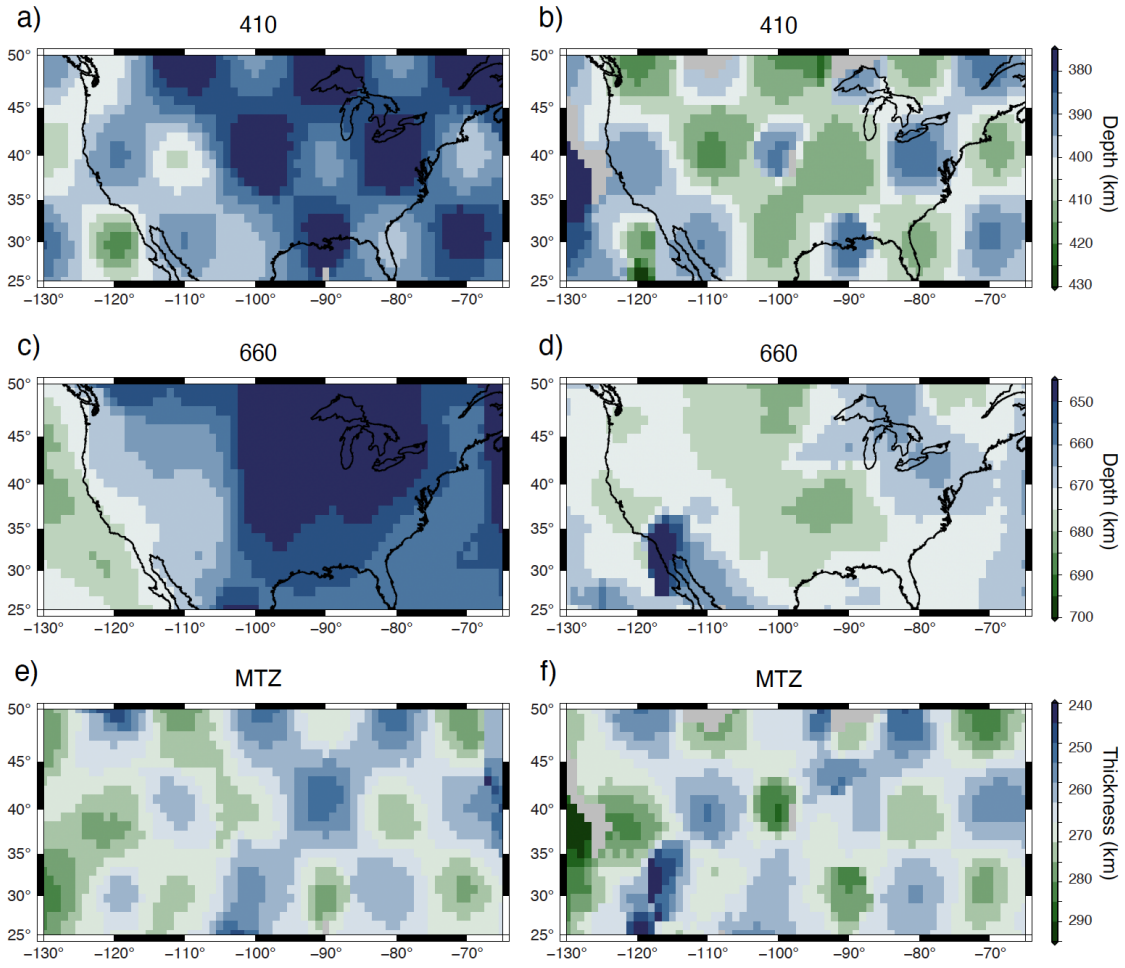

Figure 5.11: Maps of the 410-km (a and b) and 660-km (c and d) discontinuities, and the thickness of the MTZ (e and f) inferred for a model with the S40RTS model velocity structure for the mantle and $5^\circ \times 5^\circ$ harmonic undulations on the 410. In the maps along the right column (b, d, f) the effects of the velocity structure have been removed by using ray-theoretical traveltime corrections.

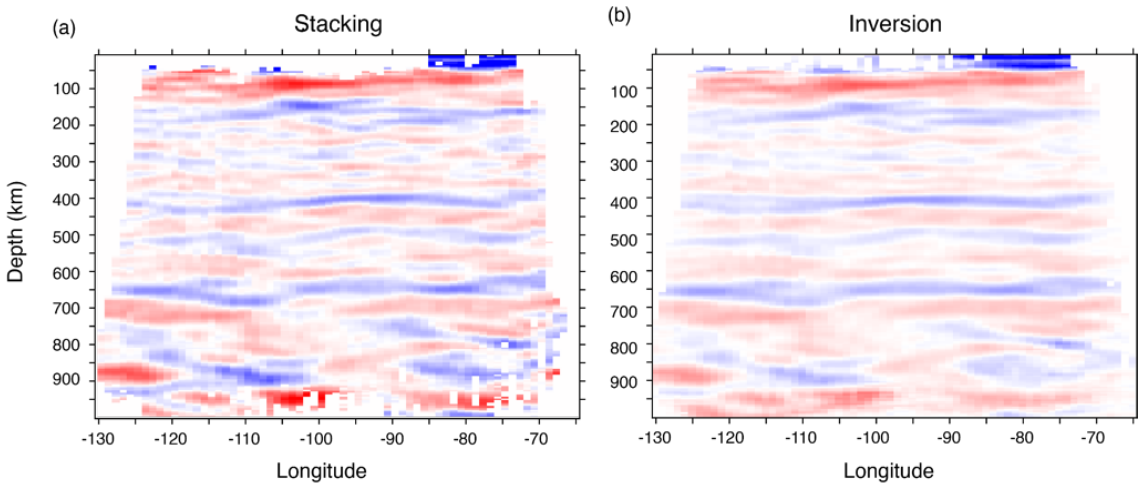

Figure 5.12: Vertical section of the CRP image along 40°N determined by our stacking method (a) and SB19's inversion method (b). See also Figure 4. The color scale is the same as Figure 4a. Because CRP imaging is based on 1-D wave propagation, it is difficult to estimate the amplitude of Ssds produced by local reflecting boundaries and undulating global discontinuities. If a reflecting boundary exists only beneath the source, the source-side contribution to Ssds is underestimated because half of the amplitude of Ssds is attributed to a reflection on the receiver side. On the other hand, the source-side reflection is overestimated if a reflection boundary exists only beneath the USArray. We expect therefore that the impedance contrasts of reflecting boundaries are uncertain despite our large set of amplitudes from earthquakes at all azimuths from the USArray. Our implementation of the inversion approach results in a misfit reduction smaller than 10%, underscoring the difficulty of separating source-side and receiver-side contributions to Ssds waveforms and that the impedance contrasts are uncertain. The synthetic tests by SB19 also illustrate this.

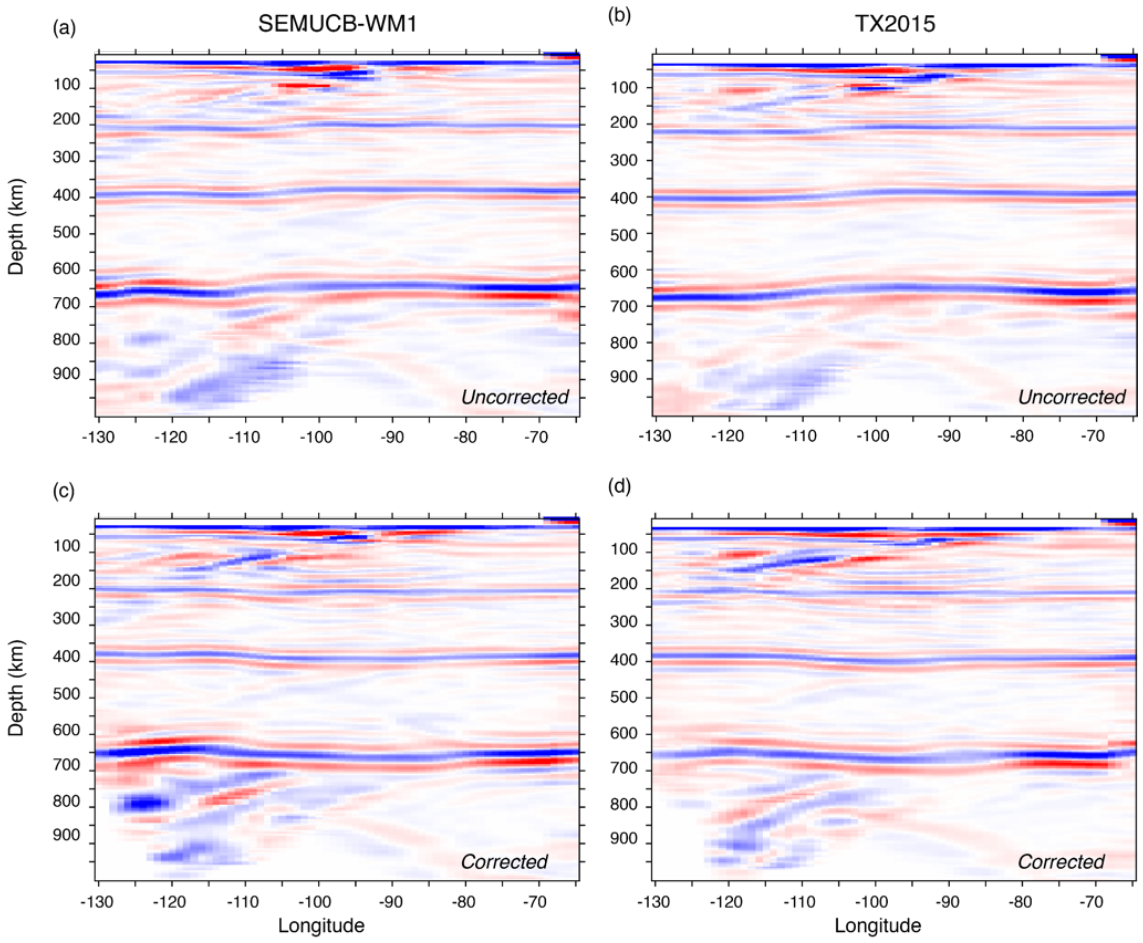

Figure 5.13: CRP image along the 35° parallel determined for (a and c) SEMUCB-WM1 and (b and d) TX2015 synthetics without (in a and b) and with (in c and d) ray-theoretical corrections. The color scale is the same as Figure 4a.

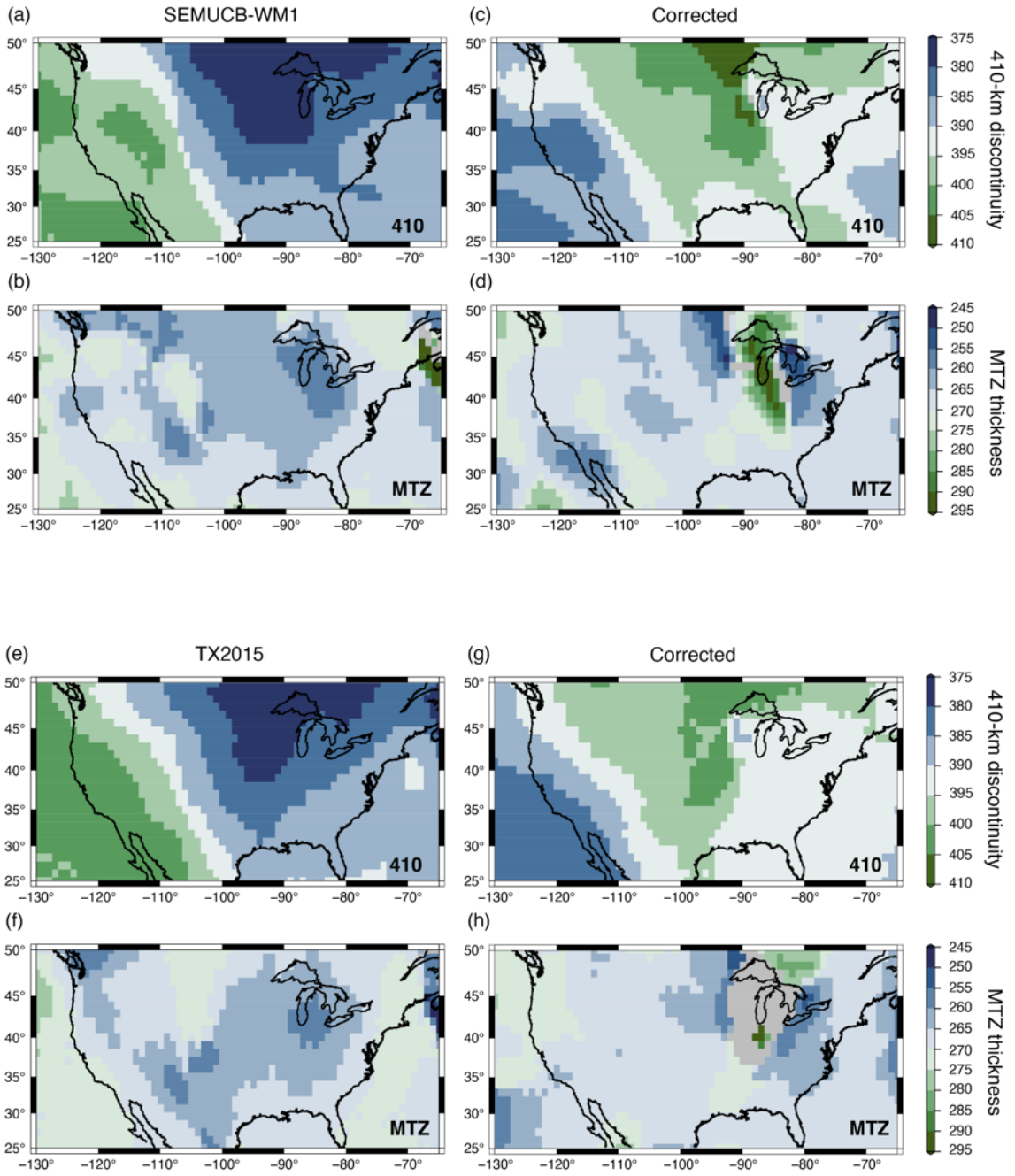

Figure 5.14: Depths of the 410 and the thickness of the MTZ obtained by CRP imaging spectral-element-method seismograms computed for model SEMUCB-WM1 (a–d) and TX2015 (e–h) with and without ray-theoretical traveltime corrections. Compare to Figure 9.

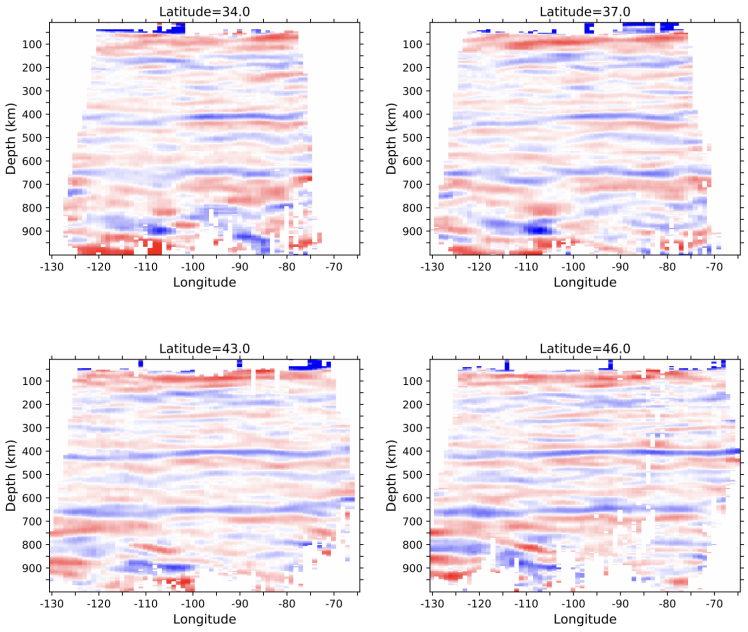

Figure 5.15: Vertical section of the CRP image along 34°N, 37°N, 43°N, and 46°N. Red and blue indicate positive and negative polarities, respectively. The color scale used is the same as in Figure 4a.

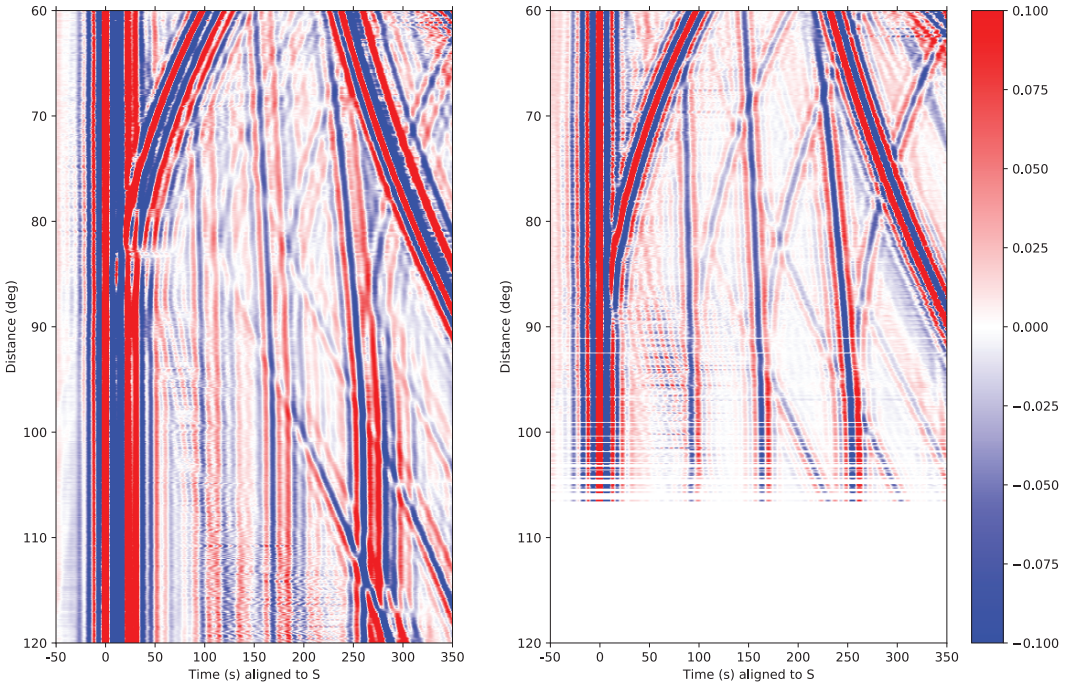

Figure 5.16: Record section of synthetic vertical waveforms aligned to S waves (same as Figure 1) from the PREM model with (left) and without (right) the crust.

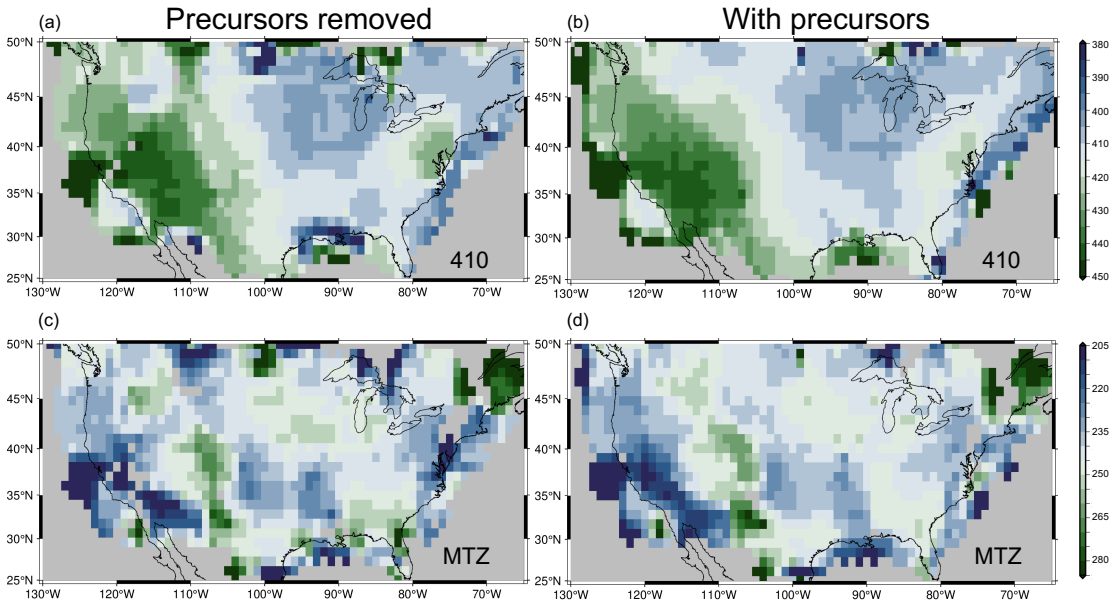

Figure 5.17: (a) and (b) are the depth map of the 410-km discontinuity. (c) and (d) are the thickness maps of the MTZ. Subtitles indicate whether precursors are considered.

CHAPTER 6

Extracting 410-km and 660-km Reflections from the Coda Correlation Wavefield *

6.1 Introduction

Hours-long ground motions recorded after earthquakes are produced by seismic waves reflecting off the surface and Earth's inner and outer core, generating continuous reflection and refractions that crisscross Earth's interior. Cross-correlation and stacking techniques have proven invaluable in unraveling the complex seismic phases. Coda correlation (*Tkalčić et al.*, 2020) has gained prominence in recent years to be a powerful tool in estimating the travel time of a plethora of phases and exploring Earth's layered structures, and even extending its applications to other planets like Mars and the Moon (*Wang and Tkalčić*, 2023).

However, reflections from the 410-km and 660-km discontinuities within the mantle transition zone (MTZ) are considerably weaker compared to the core phases. This raises a question: Can coda correlation emerge as an effective tool for imaging the mantle transition zone? Here, we present our findings on the coda correlation signal of P410p using the Southern California Seismic Network, a down-and-up wave associated with the mantle transition zone, detected within a specific inter-station distance range.

P410p should in principle follow any seismic phase. Consequently, by cross-correlating long records of coda, we anticipate the generation of a discernible correlation signal. As depicted in Figure 1, consider a specific reflection or refraction phase (depicted by the blue dashed line). After this phase reaches the Earth's surface (indicated by the thick black curve), it reflects downwards and reflects upwards at the 610-km or 410-km discontinuities which are the upper and lower boundaries of the mantle transition zone. As in the theory of ambient noise, we can treat the station recording the original phase (magenta triangle) as

*Chapter 6 is to be submitted to *The Seismic Records*: Liu, Meichen, Jeroen Ritsema, and Zack Spica. "Extracting 410-km and 660-km Reflections from the Coda Correlation Wavefield"

the source, while the station recording the reflected phase (green triangle) can be seen as the receiver. The cross-correlation between the two recorded signals will reveal a pronounced signal at the arrival time of the two phases. By leveraging the precise timing of this signal using a large range of inter-station distances, we can build a travel time curve for this reflection and constrain the velocity structure and depths of the 410-km discontinuity.

6.2 Exploration on Global Correlograms

To validate our analysis procedures, we conducted two sets of correlation computations using earthquake data from Global Seismic Network (GSN) stations and USArray Backbone stations.

We employed global earthquakes following the approach established in *Tkalčić et al.* (2020) for consistency. Before analysis, we removed instrument responses, performed rotation, and resampled the data to a 10 Hz sampling rate. We further performed running-absolute mean normalization in the periods in time and frequency domains aimed at enhancing the visibility of weak signals. We linearly stacked correlation functions at each bin of the inter-station distance and filtered to 15$\sim$50 s.

We first selected 117 earthquakes that occurred globally from 2010 to 2020 with magnitudes falling within the range of Mw6.5 to 7.5 and depths exceeding 100 km recorded by 36 USArray Backbone stations and focused on the time window 3 to 6 hrs after each earthquake event. The results, as depicted in Fig. 6.2, revealed pronounced correlation signals of body and surface waves in the vertical components, while the radial and transverse components primarily exhibited Rayleigh waves. Therefore, we decided to focus on the vertical components for subsequent analysis.

Subsequently, we extend our analysis to a broader array of stations within GSN to ensure comprehensive coverage of the inter-station distance spanning 0 to 180 degrees. We further optimized our approach by utilizing three distinct time windows, each covering 3-hour intervals: 3$\sim$6 hrs, 6$\sim$9 hrs, and 9$\sim$12 hrs following the earthquake origin time. Fig. 6.3a presents the correlogram mirroring the pattern observed in Fig. 2 of *Tkalčić et al.* (2020). Our confidence in the validity of the correlogram was further reinforced through a validation process employing synthetic waveforms generated using Mineos software (*Masters et al.*, 2011) based on normal mode summation. We simulated waveforms recorded at GSN stations for 117 earthquakes, and we subjected them to the same correlation analysis as the GSN waveforms. Shown in Fig. 6.3b, the correlogram of synthetic waveforms exhibited a striking similarity to that of GSN waveforms, underscoring the reliability and consistency of our analysis processes and the validation of our approach.

6.3 Exploration on Regional Correlograms

Reflecting waveform amplitude, when considering the reflection coefficient, typically peaks at near-normal incidence. Over hours-long propagation periods, seismic waves with large incidence angles tend to become indiscernible, while those with near-normal incidence remain prominent. Hence, reflections at 410-km and 660-km discontinuities are expected to be near vertical to the Earth's surface. This informs us that cross-correlation of coda waveforms from nearby stations is the most likely approach to identify a robust correlation signal between original phases and their corresponding reflections. Furthermore, due to the near-normal incidence and estimated from S and P wave velocities, the travel time difference between the original phase and reflected phases should be within 5 minutes. As such, in the following analysis, we refined our scope to a shorter time range, and we employed a regional seismic network to calculate correlograms.

We use 855 earthquakes with magnitudes larger than Mw6.5 that occurred between 2000-2021 and were recorded by the Southern California Station Network (Fig. 6.4). Fig. 6.5 shows the distribution of inter-station distance. About 90% of station pairs have an inter-station distance smaller than 4 degrees, ensuring we have enough small pairs of stations with a small inter-station distance.

As global studies, our analysis used coda waves commencing three hours after the earthquake origin time. We used ten continuous windows, each spanning ten minutes. Within each of these windows, we calculated a correlation function, resulting in a total of ten correlation functions, and took their average to be the final correlation function S dedicated to a unique station pair. With a bin size of 0.01 degrees, we compute the root stack

$$\sqrt{\frac{1}{n}\sum_{i=1}^{n}\sqrt{S_i}}, \tag{6.1}$$

consolidating the correlation functions for pairs with inter-station distances falling within the same bin. To further enhance the signal, we take the square root of the summation within each bin. Note that we applied a filter to the correlograms in the frequency range of 0.03$\sim$0.1 Hz, aiming to unveil finer layering structures demanding higher resolution for accurate identification of correlation signals.

In Fig. 6.6a, we present the resulting correlogram, where dashed lines, running from top to bottom, correspond to the theoretical arrival times of reflection waves calculated from iasp91, including S660p, S410p, P660p, and P410p. Here, the numerical values denote the reflection depth, while subsequent characters indicate whether the reflected waves are P or

S waves. A strong Rayleigh wave correlation signal with the highest slowness is evident, along with a signal arriving at a lag time of approximately 120 seconds, coinciding with the lag time curve of Pv410p. Beyond 200 seconds, amplitudes are also relatively large, but distinguishing whether they represent signals or background noise proves challenging. We highlight that useful information 2 degrees is obscured by the dominant Rayleigh wave signal. To address this, we applied an FK filter to eliminate signals with phase velocities smaller than 0.06 deg/s, as illustrated in Fig. 6.7. The filtered correlogram, shown in Fig. 6.6b, effectively reduces the influence of the Rayleigh wave. While this filtered version provides some improvement over the unfiltered one, discriminating correlation beyond 2 degrees remains a challenging task. There appears to be a signal that follows a similar trend to the Pv410p curve but lags by approximately 20 seconds. Notably, no apparent signals align with the theoretical arrival curves of the other three reflecting phases.

6.4 Preliminary discussions and conclusions

We established the coda correlation analyzing procedure and explored its potential for detecting reflections from the mantle transition zone. Our investigation, utilizing data from USArray Backbone stations, has revealed that coda correlation proves effective primarily for vertical components. Subsequent analysis with GSN stations has not only validated our analytical processes but also prompted us to apply coda correlation within the Southern California Seismic Network. Within this regional context, we successfully identified potential reflection waves, possibly P410p, after applying an FK filter to the correlogram results.

Successful reconstruction of the global coda wavefield validates our analyzing procedure, though, we have several problems to solve in the study of the reflection on MTZ. The first problem is the unobserved P660p phase. A stronger reflection from the 660-km discontinuity than the 410-km discontinuity is expected due to the larger velocity contrast at 660-km discontinuity. As shown in Fig 5.3, the reflection from 660-km discontinuity is at least as discernible as the reflection from 410-km discontinuity. One plausible explanation could be the significant depth variation associated with the 660-km discontinuity, which might dilute the reflection signal when averaged globally. However, the depth variation of 660-km discontinuity is not enough to explain complete the disappearance of the P660p phase in the correlogram, because the 660-km reflection remains strong after stacking across the contiguous US, again demonstrated by the record section in Fig 5.3. The other plausible reason is the P660p and S410p overlap and counteract each other. This is possible at a distance of about 4 degrees when the two phases arrive simultaneously. At a

distance of 0-1 degree, the two phases actually should add to a stronger signal.

The second problem is the inconsistent move-out of the potential S660p phase with the theoretical move-out. We are unable to check the move-out of P410p for 1.5 degrees and above covered by a strong Rayleigh wave, whereas for S660p, the theoretical move-out is not matched. We are therefore skeptical that the S660p is observed.

The third problem is the travel time delay of the observed P660p phase. In Fig 6.6, the travel time of P660p is delayed by about 15 s. The delayed time corresponds to a 410-km discontinuity deeper by about 60 km, which is a substantial amount.

The fourth problem is that the reflection at MTZ is not necessarily beneath the Southern California Seismic network. During the several hours of propagation, seismic waves undergo multiple reflections between the Earth's surface and primary discontinuities. The reflection at MTZ may occur after any of the surface reflections. Consequently, the lag time of reflections may reflect global average results rather than from the regional area beneath recording stations. Therefore the arrival time of P660p should be a global average, making the large delay time of P660p more unreasonable.

Consequently, before moving forward to inverse the velocity structure and depths of the MTZ, we decide to revisit the data and method. In pursuit of improved results, we plan to enhance our data processing approach. We need to refine our stacking method such as phase-weight stacking and frequency bandwidth selection. We also need to exclude recordings with poor signal-to-noise ratios or glitches.

Another method to validate the MTZ reflection phases is synthetic tests. However, we face challenges in conducting synthetic tests. While Mineos excels at generating precise synthetic waveforms, it is primarily limited to low frequencies, with an upper bound of 0.04 Hz from our tests. Our optimal frequency range for regional studies lies between 0.03 and 0.1 Hz. We initially explored the Direct Solution Method but encountered issues with the inaccurate coda waves due to the excessive length of the simulated time range. Inaccurate coda waves result in wrong correlograms. We are committed to exploring alternative methods to address this limitation. Successful synthetic testing holds the promise of significantly enhancing our understanding and interpretation of the correlation signals associated with reflections from the 410-km and 660-km discontinuities.

In conclusion, our successfully reconstructed global correlogram and identified major core phases. We observed plausible reflection phases from MTZ P660p in the regional correlogram but remain cautious about it. We will revisit and recheck plausible MTZ reflection phases using synthetic tests.

6.5 Figures - Chapter 6

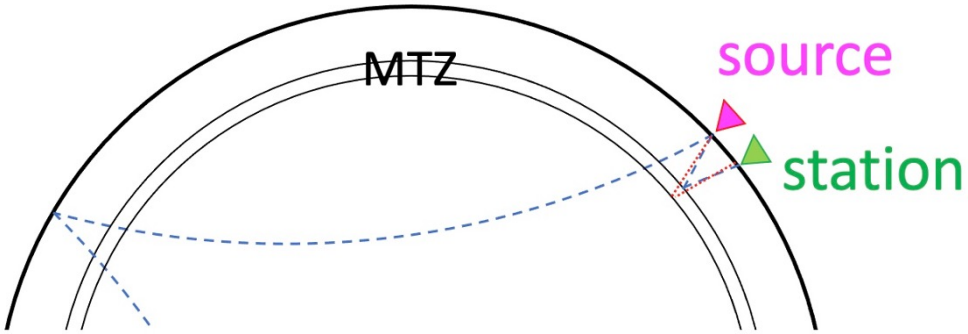

Figure 6.1: Schetch map of additional reflections at mantle transition zone (MTZ).

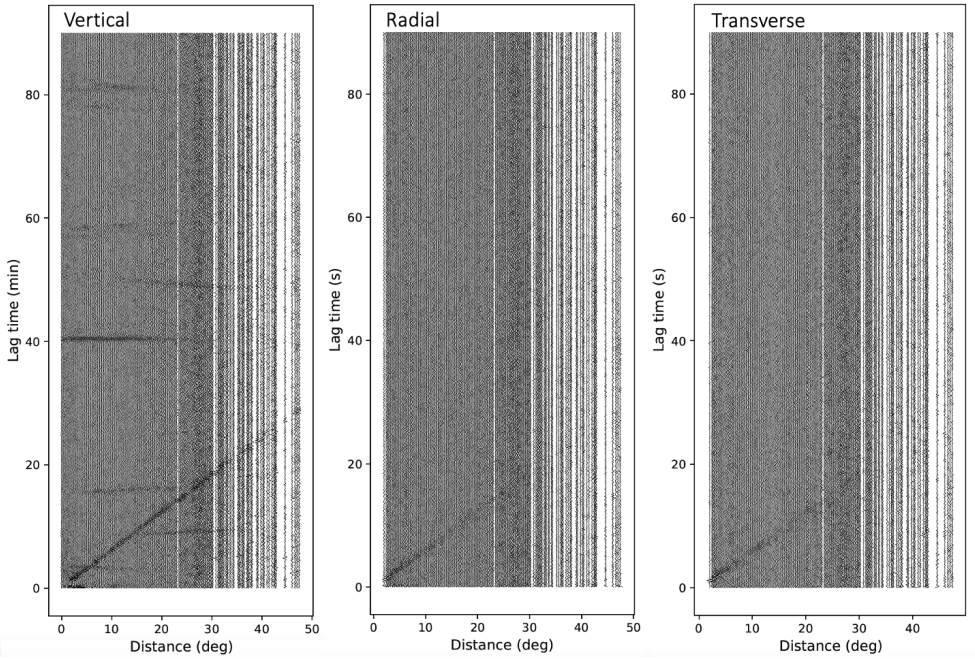

Figure 6.2: Correlograms of the vertical, radial, and transverse component using the US-Array Backbone stations.

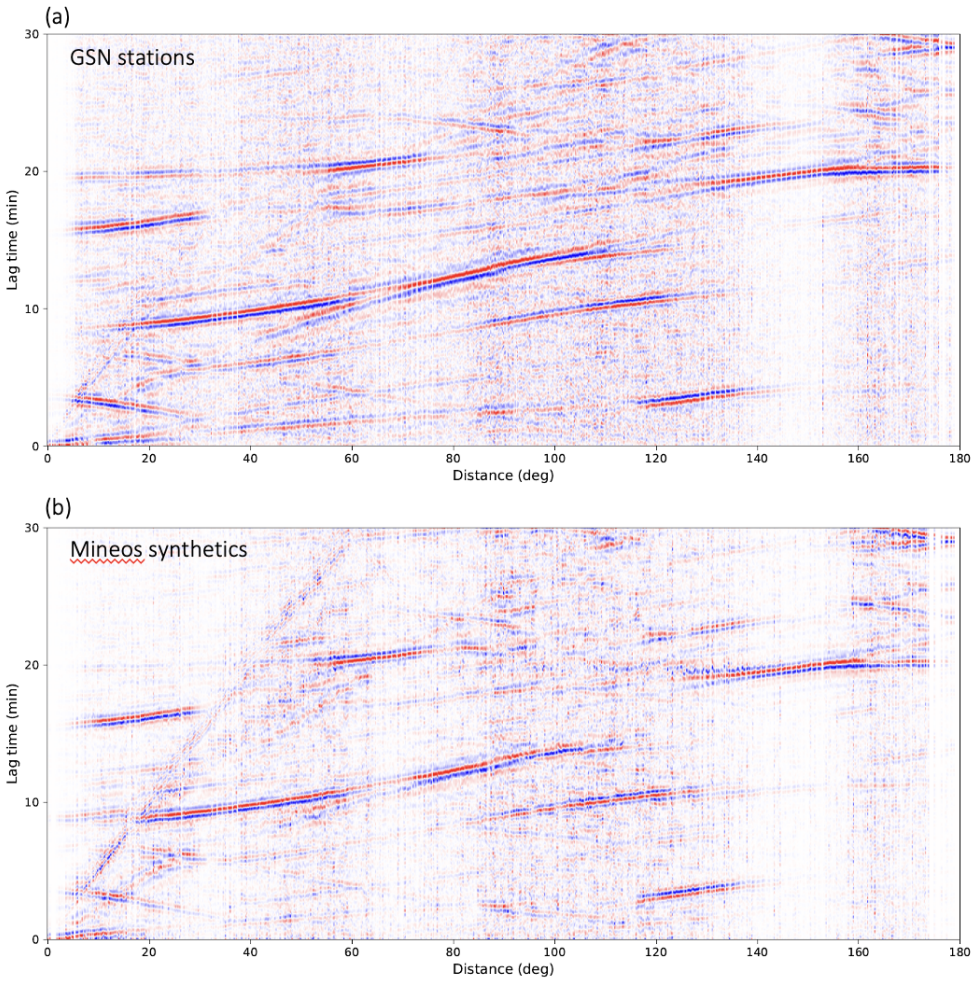

Figure 6.3: Correlograms of seismic waveforms recorded by GSN stations and synthetic waveforms.

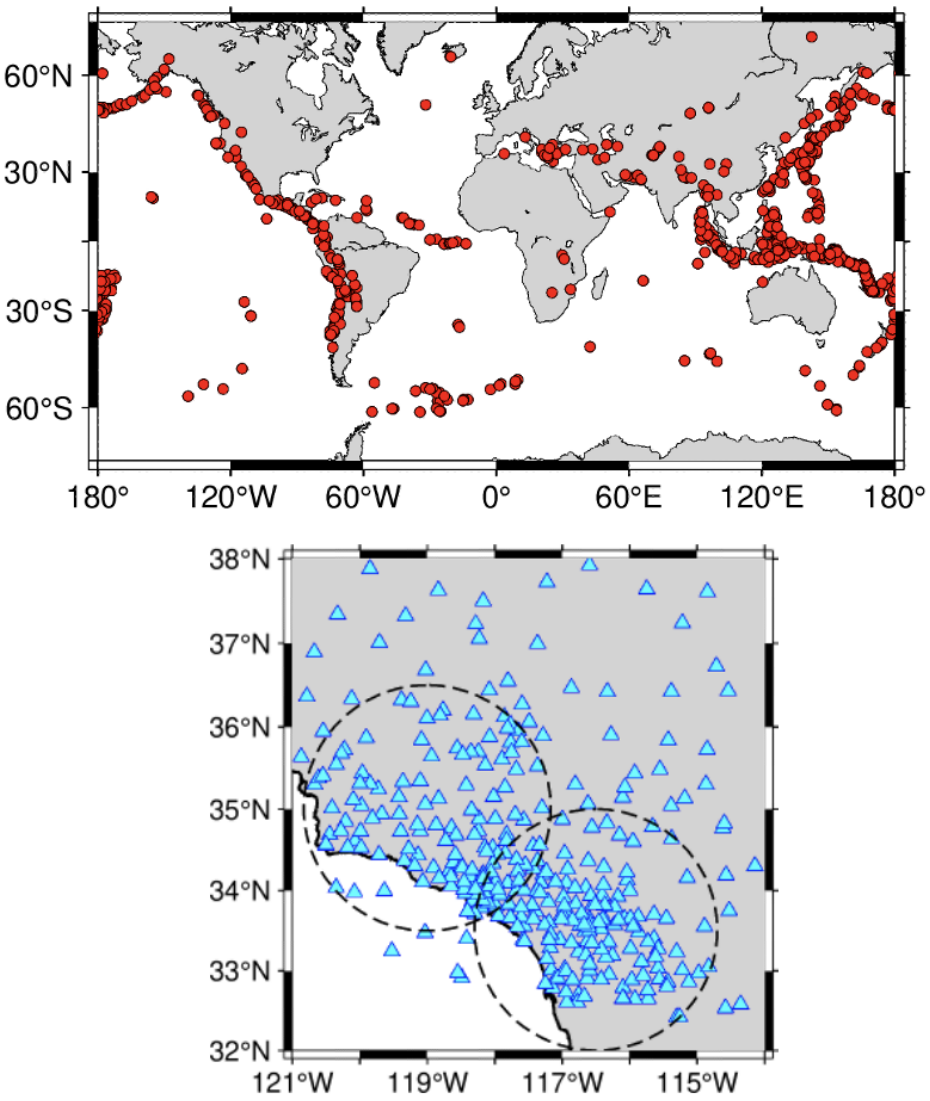

Figure 6.4: Maps of 855 earthquakes (red circles) and Sourthern California Network stations (cyan triangles).

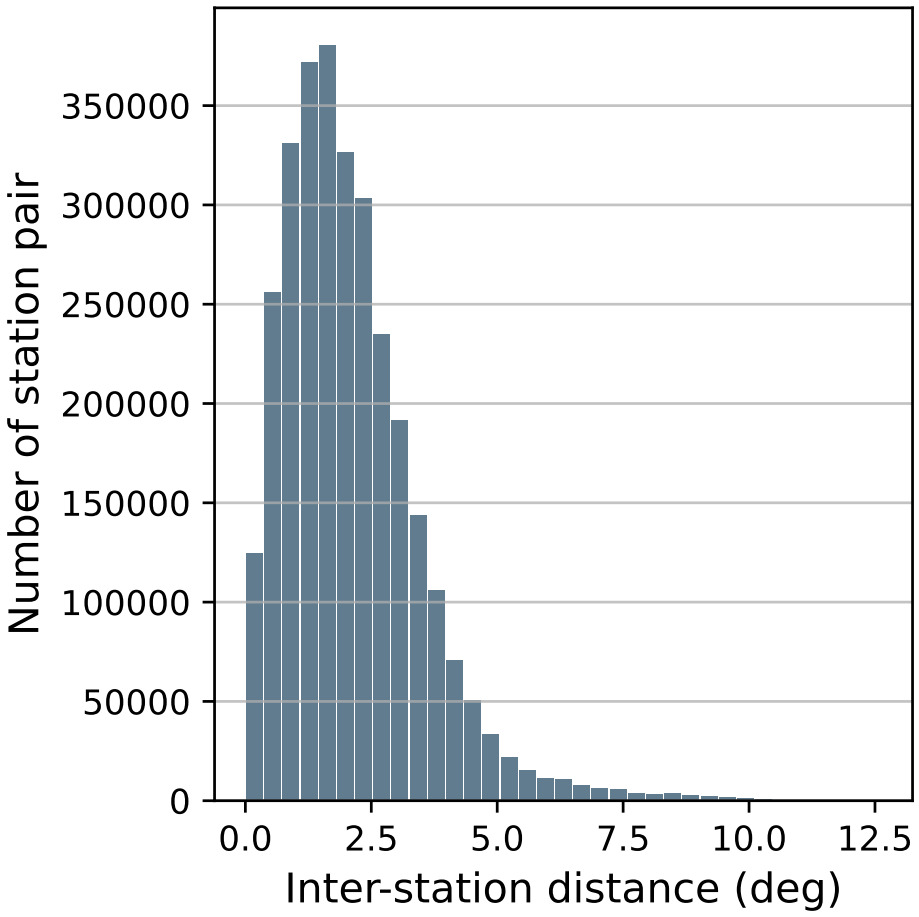

Figure 6.5: Distribution of inter-station distance for the Southern California Station Network.

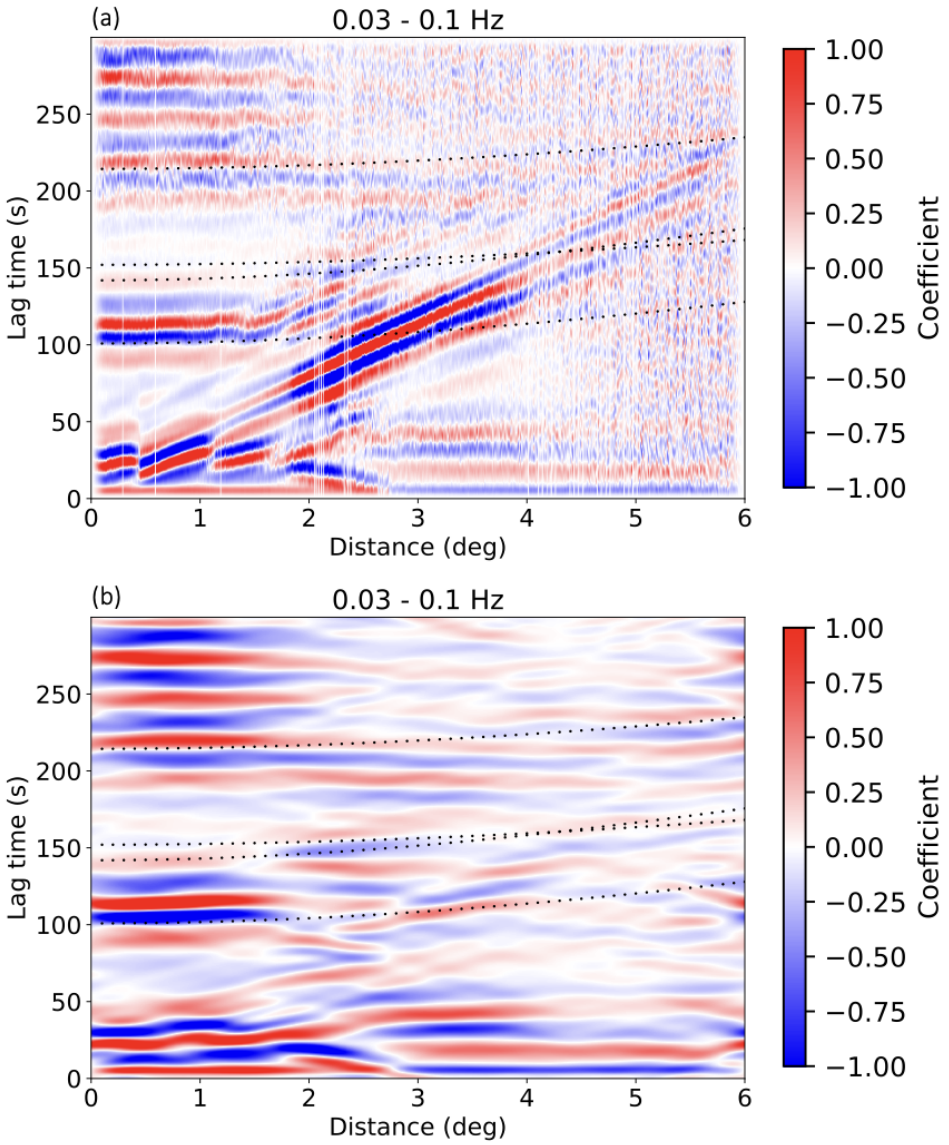

Figure 6.6: Correlogram using the Southern California Seismic Network color-coded by the cross-correlation coeffect of coda waves. The coefficient is normalized to 1. (a) Original correlogram filtered to 0.03 to 0.1 Hz. (b) FK-filtered correlogram based on (a) to remove the Rayleigh wave.

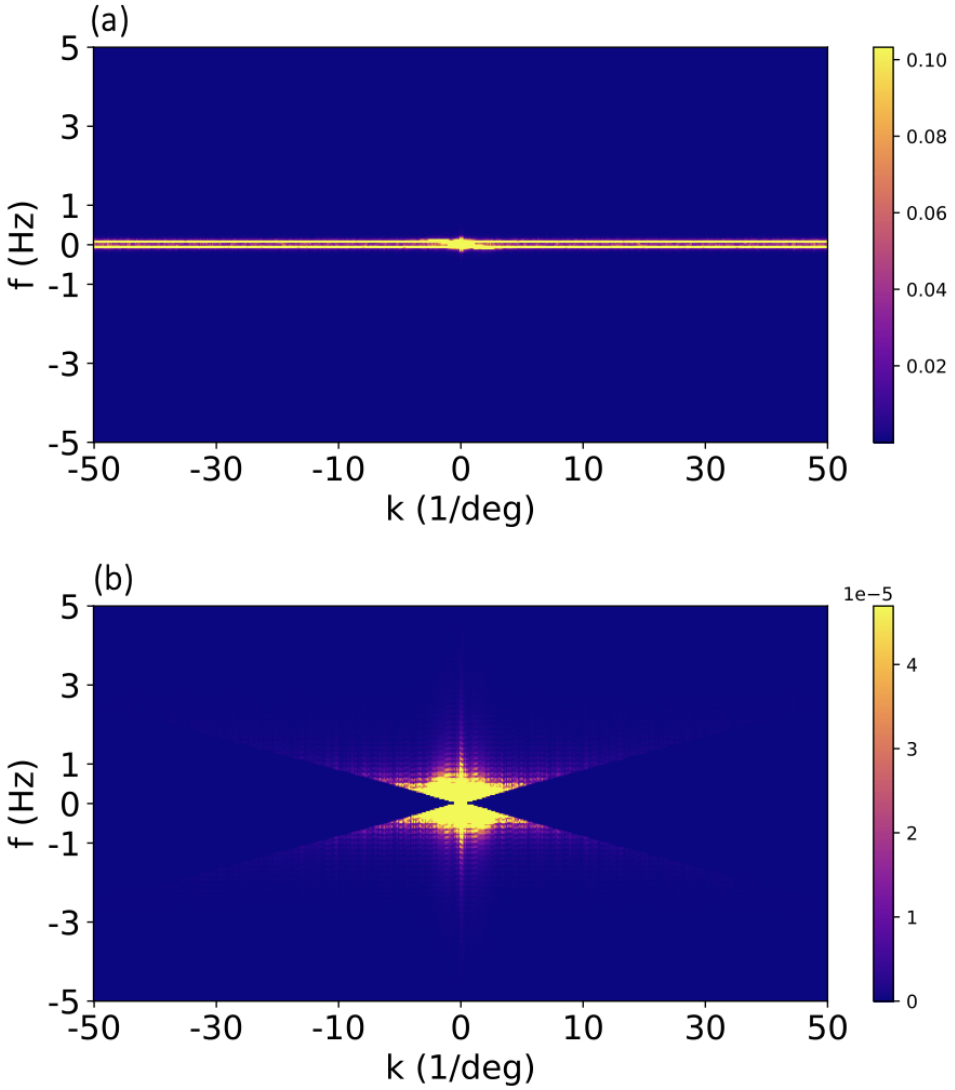

Figure 6.7: Illustration of FK filter. (a) Frequency-wavenumber spectra of Fig. 6.6a using 2d Fourier Transform (b) Spectra with wave velocity smaller than 20s/deg in (a) is whitened. Apply inverse 2d Fourier Transform to obtain Fig. 6.6b.

CHAPTER 7

Preliminary Exploration on Distributed Acoustic Sensing Data in Cordova, Alaska *

7.1 Introduction

Distributed Acoustic Sensing (DAS) has emerged as a transformative geophysical technology, leveraging optical fibers to establish an ultra-dense seismo-acoustic array. Through the monitoring of phase shifts in Rayleigh-scattered laser pulses, DAS provides a means to capture high-resolution acoustic vibrations and strain fluctuations. This technology has proven to be incredibly versatile, finding applications in a wide range of fields, including subsurface structure imaging, seismic activity monitoring, earthquake source investigations, urban vibration studies, and the exploration of oceanic dynamics, as demonstrated in various studies *Lindsey et al.* (2019); *Zhan* (2020); *Lindsey and Martin* (2021); *Li et al.* (2023). The sensitivity of DAS to various signal types, including seismic waves in the Earth's solid crust, ocean acoustic waves, and ocean gravity waves, has expanded its potential for use across diverse scientific domains.

In particular, Ocean Bottom Distributed Acoustic Sensing (OBDAS) is cost-effective and resilient in harsh environments, and marine fiber cables are widespread. It offers opportunities to study coastal ocean dynamics, seafloor geodesy, and geo-hazard investigations. In particular, long-period waves (periods >1 s) recorded by OBDAS enable high-resolution subsurface imaging, as demonstrated by (*Viens et al.*, 2023), and facilitate the ocean current measurement. Recent OBDAS investigations have successfully identified temperature changes associated with internal tidal fluctuations (*Ide et al.*, 2021; *Williams et al.*, 2023), at a level of precision necessary for measuring subtle seafloor strain signals once temperature variations are corrected (*Zumberge et al.*, 2018).

*Chapter 7 is in preparation: Liu, Meichen, Zack Spica, and Jeroen Ritsema. "Preliminary Exploration on Distributed Acoustic Sensing Data in Cordova, Alaska"

The focus of our research centers on a 50-kilometer-long ocean-bottom DAS Array integrated into the submarine cable that links Cordova and Valdez in Alaska, as illustrated in Figure 7.1. This DAS Array consists of 4,992 channels, each with a gauge length of 10 meters. It extends from Cordova towards the ocean, with a turning point 7.7 km north of Cordova. The dataset collected by this DAS Array from May 4 to July 21, 2023, at a sampling rate of 100 Hz, presents a unique opportunity to delve into long-period signals and subsurface structures. In the following subsection, we will present our findings regarding long-period signals and structural imaging through inversion of surface wave dispersion curves visible in cross-correlation functions.

7.2 Long-period Tidal Signals

We identified long-period fluctuations in DAS strain that align with tidal variations. We plot the detrended and demeaned strain for channels 300 to 1200 for 100 hrs starting from May 4, 2022. The strain data were low-passed to 0.025 Hz. As shown in Fig. 7.2b, we observe apparent wave propagation between around channel 400 to channel 1200 with a period of approximately 12 hrs. The periods correlate with tide height records from the National Oceanic and Atmospheric Administration (NOAA) station at Cordova.

This finding substantiates DAS's capacity to record long-period waves, marking the first observation of tides causing DAS strain. Differing from internal tides observed at greater depth using temperature data (William et al., 2023), these tidal fluctuations reflect changes in seawater pressure.

Two clearest tidal signals are evident between channels 400 to 950. These channels were situated in waters less than 50 meters deep, as illustrated in Figure 7.2b. The signal strength can likely be attributed to amplification in relatively soft soil near the shoreline. This observation not only offers insights into the sediment properties of the seafloor where DAS cables are buried but also implies that DAS can be used to detect long-period signals and be a resource for tsunami monitoring and early warning systems.

Secondly, the tidal signals were recorded close to where the cable changed direction. Both ends of the DAS cable were connected to the open ocean, so the ocean waves may propagate towards channel 770 from both sides simultaneously. The interactions of the convergence of seawater may have contributed to the amplification of these tidal signals.

7.3 Subsurface Structure Imaging

To image subsurface structures, we followed a systematic process consisting of the following steps.
(1) Correlation and Stacking: We cross-correlate a source channel with other channels, utilizing 200 epochs of 10-minute strain rate data. The results were stacked to reveal the propagation of Rayleigh waves from the source channel to various other channels. For example, by cross-correlated channel 500 with all other channels, we will be able to see a high correlation signal starting from channel 500 and propagating towards channel 5000 and channel 0 both ways, though we will notice the signal fade away as the propagation length increases.
(2) Dispersion Calculation: Focusing on a particular receiver channel, we isolated a 100-channel section of correlation functions centered around it. Within this window, we computed the dispersion. To transition from the time-space correlation domain to the frequency-wavenumber domain, a 2D Fourier Transform was applied. This transformation allowed us to determine the phase velocity at different frequencies and extract dispersion curves.
(3) Averaging Dispersions: To enhance the accuracy of our dispersion curves, we systematically selected five sources with a 20-channel step centered on the receiver channel. For instance, when generating dispersion curves for channel 500, we averaged the dispersions of correlation functions from channels 450 to 550, originating from source channels 460, 480, 500, 520, and 540.
(4) Identification of Fundamental Modes: By manual inspection of local maxima, we identified dispersion curves of fundamental modes and, on occasion, overtones at the target receiver channels. In subsequent inversion processes, we only considered the fundamental modes.
(5) Inversion with Geopsy: The inversion of the fundamental modes was carried out using Geopsy, a specialized software for data analysis and modeling.

Figure 7.3a presents an illustrative depiction of the extraction of fundamental modes, spanning from channel 240 to channel 1900 with a step of 10 channels. Gaps exist in the figure for some channels due to instances of indiscernible dispersion curves. We have categorized these channels into four distinct groups based on their fundamental modes. Channels within each cluster generally exhibit a comparable trend of fundamental modes, as portrayed in Figure 7.3b. From channel 240 to channel 1900, the frequency ranges of the extracted dispersion curves gradually shift towards the lower end of the spectrum, and concurrently, the largest phase velocities exhibit a gradual increase.

The inversion results are presented in Figure 7.4 for four groups. The variance in fre-

quency ranges leads to different inversed depth ranges. The dispersions at lower frequencies carry richer information about deeper structures, consequently leading to an incremental portrayal of depth from group A to D. Group A channels are characterized by relatively small shear wave velocities, with less than 1000 m/s within 100 meters depth, whereas group B at the same depth exhibit higher shear wave velocities. Groups C and D are capable of inversing deeper structures, extending up to 300 meters and 500 meters, respectively. Example dispersions at channels within groups A to D showcased in Figure 7.5 through Figure 7.8 provide closer looks into differences between groups. The consistency in patterns of each group echoes the grouping of dispersion curves plotted in Fig. 7.3 and we can see the apparent transition from high to low frequencies.

For post-1900 channels, the dispersion curves have such low frequencies that their extraction for inversion purposes becomes unfeasible, as we exemplified by the dispersion curve of channel 1800, which defies easy identification. Aligning this observation with the cable's elevation profile in Figure 7.1, we can see that the cable was buried increasingly deep from channel 0 to 1900, reaching its deepest around channel 2000, where it remained consistently deep for all subsequent channels. This intriguing connection between the evolution of dispersion curves, the increase in cable depth, and the distance from the coastline suggests that high-frequency sources originating from land exhibit a rapid attenuation as they propagate into the deeper realms of the ocean floor.

7.4 Preliminary conclusions & Future works

In the inversion of surface wave dispersion curves, we used a short time length (about 1 week) compared to the DAS recording time (about 2 months) while still obtaining clear fundamental modes and sometimes overtones of Rayleigh waves. We are unable to reconstruct the fine velocity structure along the cable from the rough dispersion curves. If the entire 2 months of data are cross-correlated and stacked, we expect to get much cleaner dispersion curves and more modes, therefore imaging the velocity structure in the shallow part.

As shown by Fig 7.5, 7.6, 7.7, and 7.8, the high-frequency dispersion curves become less obvious when moving towards the ocean. The reason is that urban noise is of more high-frequency energy. As the DAS cable extends towards the ocean, the urban noise decreases and the primary source becomes microseisms, for which the predominant frequency ranges are approximately 0.05 to 0.5 Hz. The high-frequency noise decreases as the distance to the coast increases. The current time window for cross-correlation is 10 minutes. We plan to use a variety of time window lengths, ranging from 10 minutes to 10 days to

adapt to different channel locations. Our goal is to identify the ocean's internal waves. With the acquisition of long-period signals, we show the potential in harnessing the full potential of the DAS cable for geophysical research.

Tidal signals displayed in Fig 7.2 serve as a promising indicator for the potential discovery of other long-period signals such as oceanic internal waves. To understand the formation of this tidal wave, we will first analyze the temperature recordings at the same channels. *Williams et al.* (2023) observed temperature tidal signals of DAS changing with tides, indicating that the temperature may significantly affect when the cable is unburied and affected by the seawater. Our DAS cable is buried, though, the bury depth is relatively shallow ($<$15m) for channels recording tidal signals. In addition to the temperature influence, we also need to consider special local geological settings such as the convergence of seawater around channel 770, soft soil amplification, and the regional sea level changes.

In the forthcoming phases of the research, we intend to refine our techniques, extend the scope of our investigations, and leverage DAS technology to its full potential. These endeavors will deepen our understanding of the Earth's subsurface and expand our capabilities in monitoring a wide range of geophysical phenomena.

7.5 Figures - Chapter 7

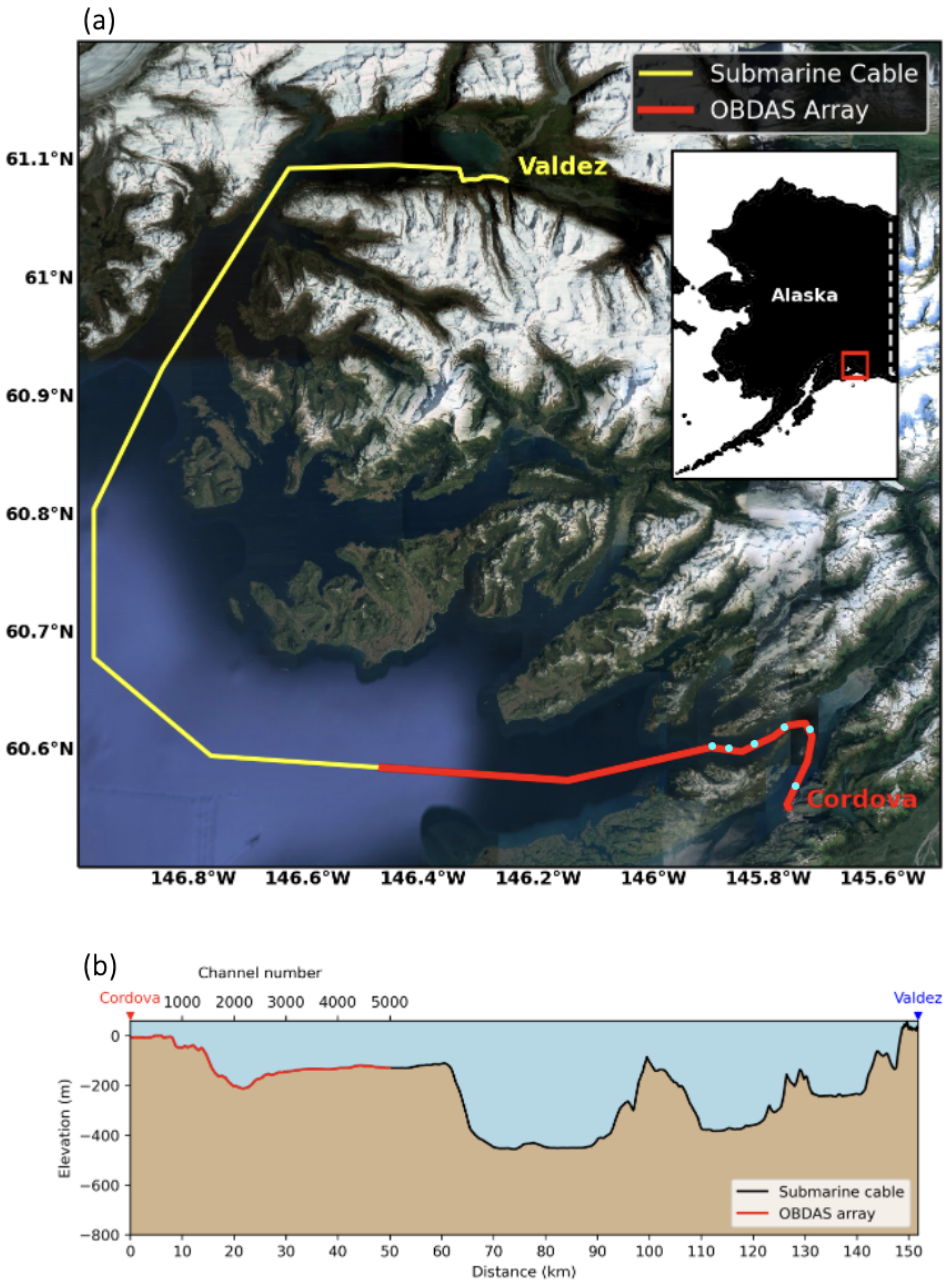

Figure 7.1: (a) Bird-view map of the DAS cable in Alaska, spanning from Cordova to Valdez. The location of the map is highlighted by a red square in the inset map. Cyan points represent specific channels located along the cable, beginning with channel 240 at Cordova and progressing sequentially toward the ocean. Channels 770, 1090, 1440, 1660, and 1810 are marked accordingly. (b) Elevation profile of the DAS cable along its length.

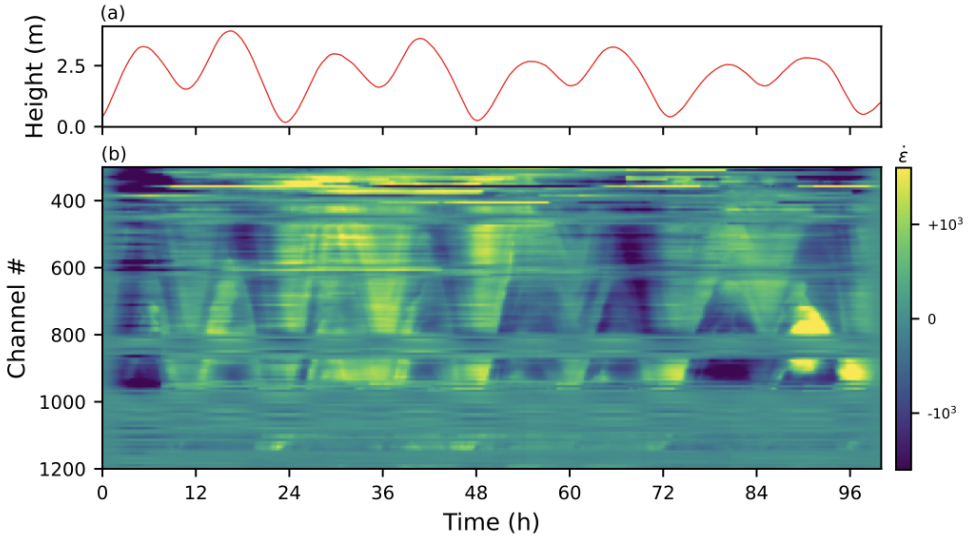

Figure 7.2: Temporal evolution of (a) tidal heights recorded at Cordova, Alaska and (b) OBDAS strain data. Time reference: 2022-05-04 19:39:56. The two plots exhibit a strong correlation with very similar periods.

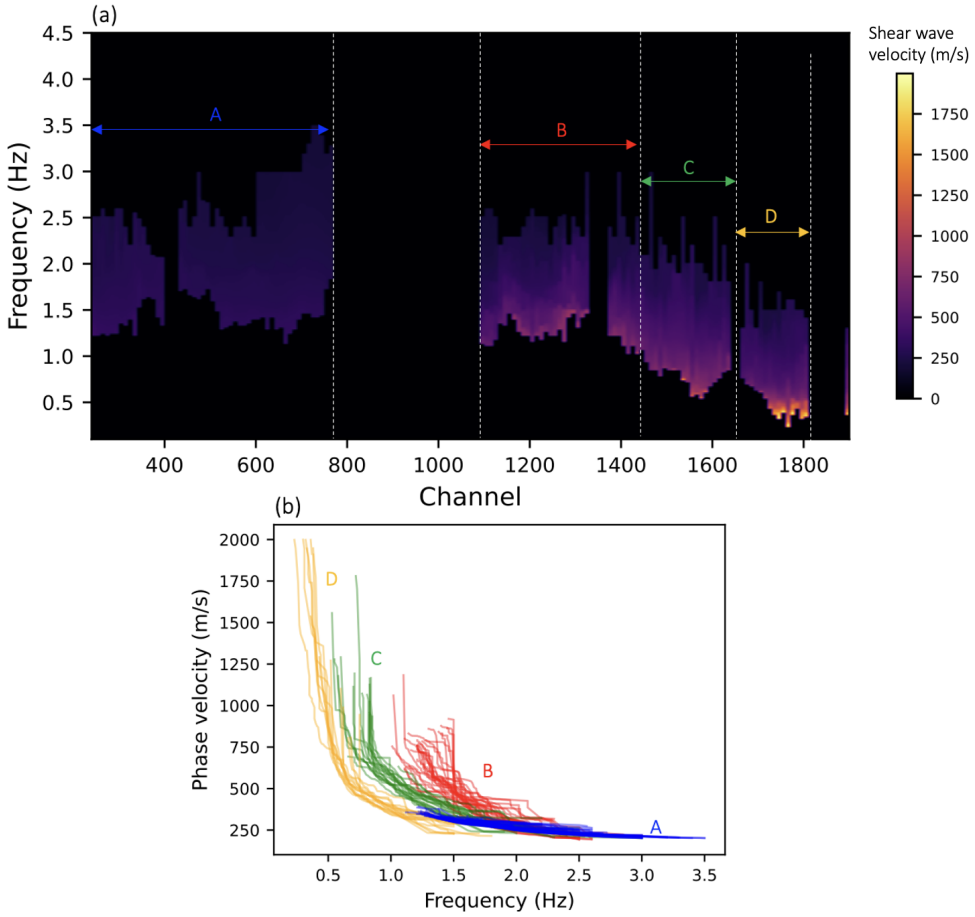

Figure 7.3: (a) Fundamental modes from channels 240 to 1900, sampled at 10-channel intervals. The color scale represents phase velocity at specific frequencies. Delineated by dashed lines, groups A, B, C, and D encompass distinct channel ranges characterized by consistent fundamental modes. (b) Color-coded fundamental modes for four groups in one plot.

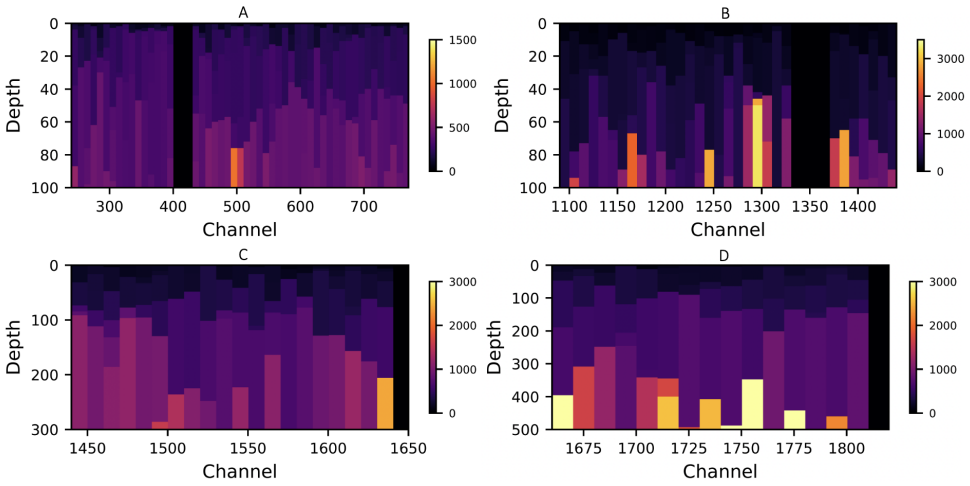

Figure 7.4: Inversion results for channels in groups A, B, C, and D. The color scales represent shear wave velocities.

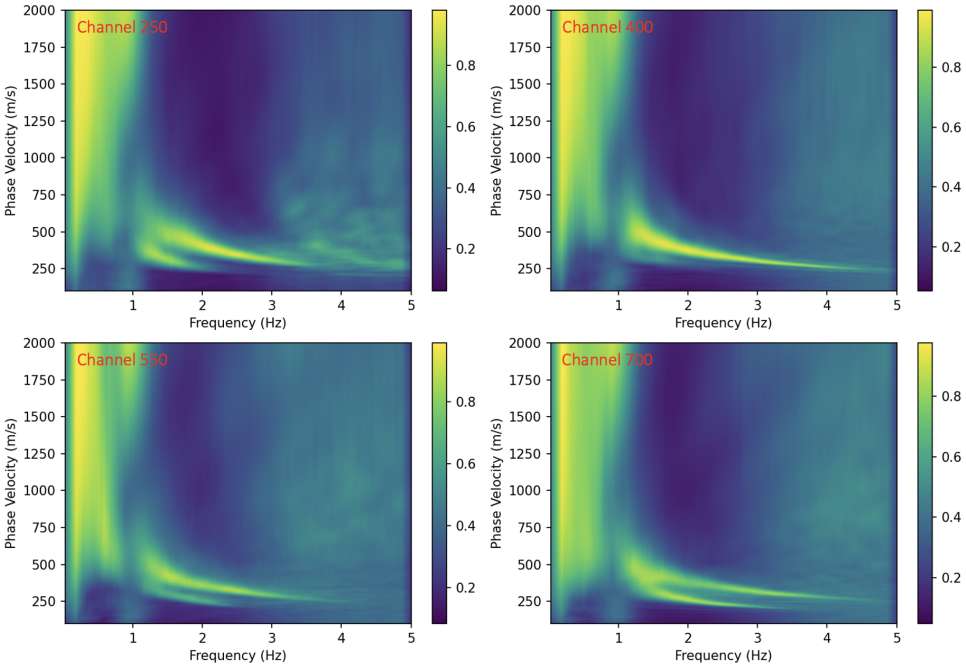

Figure 7.5: Dispersions at channels 250, 400, 550, and 700 within group A.

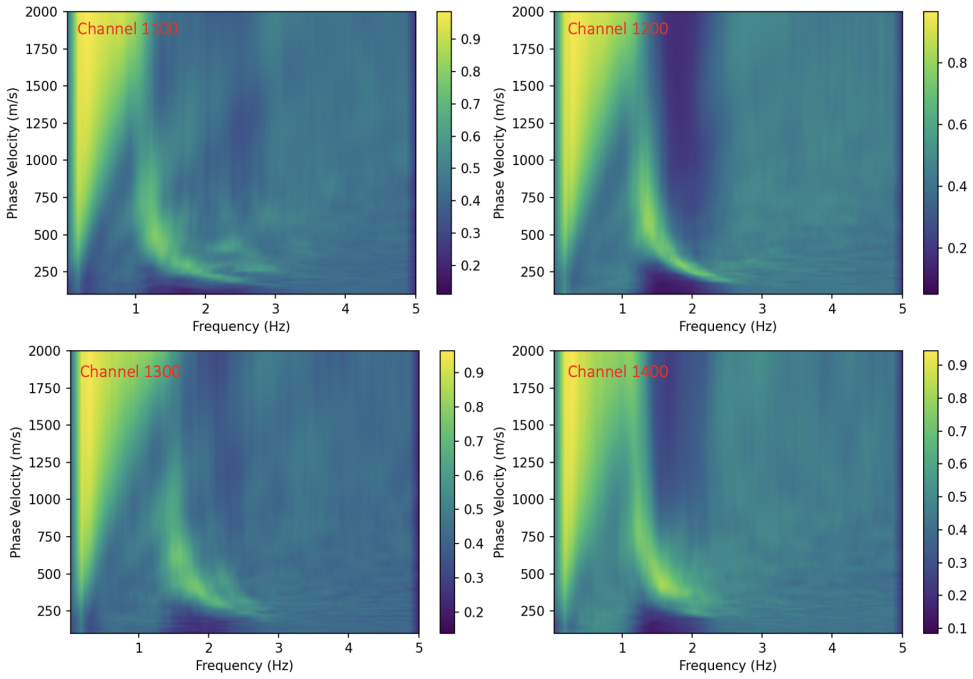

Figure 7.6: Dispersions at channels 1100, 1200, 1300, and 1400 within group B.

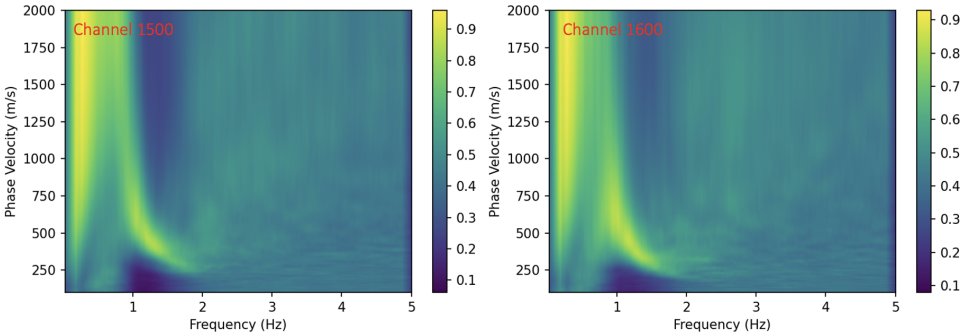

Figure 7.7: Dispersions at channels 1500 and 1600 within group C.

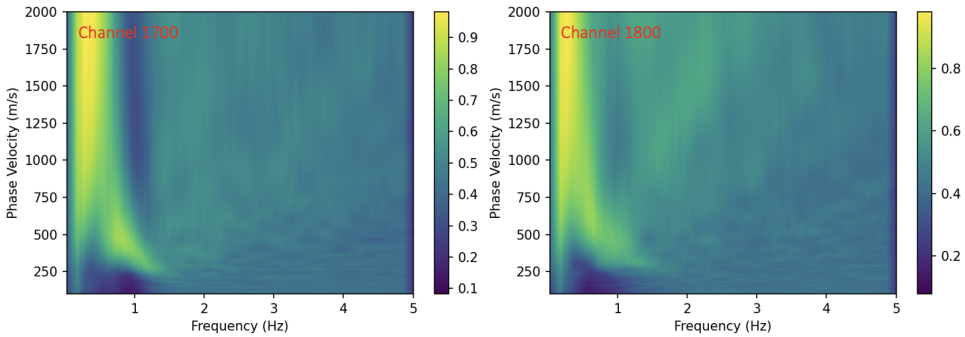

Figure 7.8: Dispersions at channels 1700 and 1800 within group D.

CHAPTER 8

Conclusions

In summary, the thesis probed two fundamental seismological research areas, earthquake source faulting processes and subsurface structures imaging, through seismic waveform analysis. Seismic waves, modulated by the excitation source and propagation media jointly, are the best resource for research. Performing waveform analysis in time and frequency domains and stacking approaches, we enhanced the estimation of corner frequencies and stress drops of earthquake sources in Chapters 2, 3, and 4, and explored the subsurface structure imaging using various phases and approaches in Chapters 5, 6, and 7.

Stress drop is the source parameter highly related to earthquake energy release and frequency content. Our exploration of stress drop starts with deep-focus earthquakes in Chapter 2. Employing the Brune source model, similar to its application in shallow earthquakes, we proved that teleseismic P-wave and S-wave spectra can be used for the estimation of source parameters. The medians of the stress drop estimates are approximately one order of magnitude higher than that of global shallow earthquakes, supporting that deep-focus earthquakes have different rupture mechanisms from shallow earthquakes. Deep-focus earthquakes are observed in the subduction zone at the depth of the MTZ. Phase transformation and shear-induced heating are the two leading mechanism assumptions featuring larger and smaller stress drops. Estimating stress drops of deep-focus earthquakes and comparing the range to that of shallow earthquakes help us gain insight into the rupture process in the MTZ, and therefore is indicative of the subduction dynamics. Limited by the data, we obtained a 3-order-magnitude variation of stress drop estimates, implying the involvement of both mechanisms for deep-focus earthquakes.

The complexity observed in earthquake sources, featuring multiple subevents compared to the simple pulse of Brune's source model, motivates the investigation of stress drops of multi-subevent earthquakes in Chapter 3. Decomposing SCARDEC source time functions, we find that over half of Mw 5.5–8.0 earthquakes exhibit multiple subevents, highlighting the common complexity of earthquakes. Our findings indicate that, under the Brune source model, corner frequency estimates may predominantly reflect the stress change of

the largest asperity rather than the average stress drop over the entire rupture area. This insight helps elucidate the substantial variance in stress drop estimates resulting from different methods defining stress drops in varying ways. We identified challenges during Chapters 2 and 3 about the lack of high-quality spectra and the large stress drop variation. To address these challenges, we introduce the point-based stacking method in Chapter 4. This approach maximizes the utilization of source spectra at each frequency point, demonstrating superior stability and accuracy in synthetic tests compared to the conventional trace-based stacking method under conditions of insufficient spectra. The variation in stress drops calculated using the new method is one order of magnitude less than that using the conventional method, particularly for deep-focus earthquakes where the number and quality of available source spectra are limited.

The implementation of the point-based stacking method on deep-focus earthquakes will allow us to compare stress drop variations with the conventional trace-based stacking method presented in Chapter 1. This comparative analysis offers insights into potential reductions in stress drop variations and prompts an exploration of self-similarity in stress drop behavior, investigating its correlations with earthquake attributes like magnitude, depth, and focal mechanism. Analyzed by the same method, a complete profile of the stress drop spanning from the shallow to the deep interior of the Earth will be built, which is indicative of the change in the earthquake physical mechanism.

Though focused on different parts of stress drop studies, the problem that connects Chapters 2, 3, and 4 is the large stress drop variation. In Chapter 3 we realized the oversimplification of the Brune source model. In Chapter 4 we tried to reduce the variation caused by data uncertainty. However, there exists intrinsic ambiguity in the stress drop that researchers estimate. The original stress drop defined in *Brune* (1970) was for a homogeneous rupture. Currently, the source parameter stress drop is referred to as the average stress drop. However, as shown in Chapter 3, the estimated stress drop may represent a focused part of the rupture rather than the entire rupture area. For heterogeneous rupture, the definition of the average stress drop is ambiguous. How to determine the range where the stress drop is averaged? Is the stress drop averaged on area, energy, or the moment (*Noda et al.*, 2013)? To solve the stress drop variation, it is necessary to accommodate the conflict between oversimplified stress drop definition and the source complexity. Additional parameters are probably needed. For example, *Ji and Archuleta* (2021) proposed double-corner-frequency models of source spectra, with two corner frequencies corresponding to two stress drops. The ultimate goal of additional parameters is to plot a better map of the stress drop over the rupture. In this case, slip inversion of a large earthquake accompanying a synthetic test would be a useful method to find appropriate additional parameters for

better characterizing the stress drop distribution over the rupture.

In the realm of subsurface structure imaging, our study centered on the mantle transition zone. In Chapter 5, utilizing long-period SH wave reverberation, we observed that the depth difference mapping of the 410-km and 660-km discontinuities beneath the western and central-eastern United States significantly improved with the incorporation of a 3-D velocity model, underscoring the necessity of considering 3-D velocity variations for accurate subsurface imaging. Through an assessment using SPECFEM synthetic waveforms, we determined that the SH reverberation imaging method based on a 3-D model performs optimally under realistic conditions, particularly when both topographic variation and undulations exist on the 410-km discontinuity. However, our resolution test revealed limitations in discerning patterns smaller than 2 by 2 degrees due to frequency constraints. Our interest in the mantle transition zone extended to coda waves in Chapter 6, where we explored the extraction of reflections from the 410-km and 660-km discontinuities using correlation wavefields of coda waves arriving hours after earthquake occurrences. We reconstructed the global correlogram with core phases and identified potential reflection signals from the MTZ, affirming the capability of coda correlation in detecting weak signals. To enhance our interpretation of these reflection signals, we plan to conduct synthetic tests involving high-frequency coda waves at frequencies up to 0.1 Hz.

Our comprehensive studies on Earth's structure span from deep to shallow depths. In Chapter 7, we conducted a preliminary exploration of Distributed Acoustic Sensing (DAS) data in Cordova, Alaska, to capture information on near-surface structures. Detecting strongly correlated tidal signals with tide heights, we validated the potential of DAS for long-period signal detection. Further applying surface wave inversion through cross-correlation, we imaged the subsurface velocity structure. Our exploration of Distributed Acoustic Sensing (DAS) data for long-period signal detection will persist. While our current investigation of DAS data is preliminary, the observed tidal signals, the availability of temperature data, and the 2-month-long recordings present a promising avenue for detecting long-period signals.

Our separate investigations of the source parameter and velocity structure imaging will significantly enhance the understanding of the attenuation property of the Earth. Compared to the global velocity structure, the attenuation structure is much less constrained. Travel times of seismic waves, determined by the velocity structure, are easy to measure. Waveform amplitude decay of seismic waves, representing the damping of the wave energy, is more complex to measure. As aforementioned, the recorded seismic wave is a convolution of the source and the structure. If the source is well understood, the waveform amplitude with the source effect deconvolved represents the attenuation effect of the media that seis-

mic waves propagate through. With a complete profile of stress drop for global earthquakes in a wide depth range, we may be able to inverse the attenuation structure of certain regions with dense ray path coverage or a rough global attenuation structure.

BIBLIOGRAPHY

Abercrombie, R. E. (1995), Earthquake source scaling relationships from- 1 to 5 ML using seismograms recorded at 2.5-km depth, *Journal of Geophysical Research: Solid Earth*, *100*(B12), 24,015–24,036.

Abercrombie, R. E. (2014), Stress drops of repeating earthquakes on the san andreas fault at parkfield, *Geophysical Research Letters*, *41*(24), 8784–8791.

Abercrombie, R. E. (2015), Investigating uncertainties in empirical Green's function analysis of earthquake source parameters, *Journal of Geophysical Research: Solid Earth*, *120*(6), 4263–4277.

Abercrombie, R. E., X. Chen, and J. Zhang (2020), Repeating earthquakes with remarkably repeatable ruptures on the san andreas fault at parkfield, *Geophysical Research Letters*, *47*(23), e2020GL089,820.

Abercrombie, R. E., D. T. Trugman, P. M. Shearer, X. Chen, J. Zhang, C. N. Pennington, J. L. Hardebeck, T. H. Goebel, and C. J. Ruhl (2021), Does earthquake stress drop increase with depth in the crust?, *Journal of Geophysical Research: Solid Earth*, *126*(10), e2021JB022,314.

Abt, D. L., K. M. Fischer, S. W. French, H. A. Ford, H. Yuan, and B. Romanowicz (2010), North american lithospheric discontinuity structure imaged by ps and sp receiver functions, *Journal of Geophysical Research: Solid Earth*, *115*(B9).

Aki, K. (1967), Scaling law of seismic spectrum, *Journal of geophysical research*, *72*(4), 1217–1231.

Aki, K. (1972), Earthquake mechanism, *Tectonophysics*, *13*(1-4), 423–446.

Aki, K., and B. Chouet (1975), Origin of coda waves: source, attenuation, and scattering effects, *Journal of geophysical research*, *80*(23), 3322–3342.

Allmann, B. P., and P. M. Shearer (2007), Spatial and temporal stress drop variations in small earthquakes near parkfield, california, *Journal of Geophysical Research: Solid Earth*, *112*(B4).

Allmann, B. P., and P. M. Shearer (2009), Global variations of stress drop for moderate to large earthquakes, *Journal of Geophysical Research: Solid Earth*, *114*(B1).

Anderson, J. G. (1997), Seismic energy and stress-drop parameters for a composite source model, *Bulletin of the Seismological Society of America*, *87*(1), 85–96.

Ando, R., and Y. Kaneko (2018), Dynamic rupture simulation reproduces spontaneous multifault rupture and arrest during the 2016 mw 7.9 kaikoura earthquake, *Geophysical Research Letters*, *45*(23), 12–875.

Antolik, M., D. Dreger, and B. Romanowicz (1996), Finite fault source study of the great 1994 deep Bolivia earthquake, *Geophysical research letters*, *23*(13), 1589–1592.

Archuleta, R. J., and C. Ji (2016), Moment rate scaling for earthquakes $3.3 \leq M \leq 5.3$ with implications for stress drop, *Geophysical Research Letters*, *43*(23), 12–004.

Atkinson, G. M. (1993), Earthquake source spectra in eastern north america, *Bulletin of the Seismological Society of America*, *83*(6), 1778–1798.

Bai, L., Y. Zhang, and J. Ritsema (2012), An analysis of ss precursors using spectral-element method seismograms, *Geophysical Journal International*, *188*(1), 293–300.

Baltay, A., S. Ide, G. Prieto, and G. Beroza (2011), Variability in earthquake stress drop and apparent stress, *Geophysical Research Letters*, *38*(6).

Bensen, G., M. Ritzwoller, and N. M. Shapiro (2008), Broadband ambient noise surface wave tomography across the united states, *Journal of Geophysical Research: Solid Earth*, *113*(B5).

Beresnev, I., and G. Atkinson (2001), Subevent structure of large earthquakes—a ground-motion perspective, *Geophysical Research Letters*, *28*(1), 53–56.

Bilek, S. L., and T. Lay (1998), Variation of interplate fault zone properties with depth in the japan subduction zone, *Science*, *281*(5380), 1175–1178.

Bina, C. R. (1997), Patterns of deep seismicity reflect buoyancy stresses due to phase transitions, *Geophysical research letters*, *24*(24), 3301–3304.

Bina, C. R., and G. Helffrich (1994), Phase transition clapeyron slopes and transition zone seismic discontinuity topography, *Journal of Geophysical Research: Solid Earth*, *99*(B8), 15,853–15,860.

Boatwright, J. (1980), A spectral theory for circular seismic sources; simple estimates of source dimension, dynamic stress drop, and radiated seismic energy, *Bulletin of the Seismological Society of America*, *70*(1), 1–27.

Boatwright, J. (1984), The effect of rupture complexity on estimates of source size, *Journal of Geophysical Research: Solid Earth*, *89*(B2), 1132–1146.

Boué, P., P. Poli, M. Campillo, H. Pedersen, X. Briand, and P. Roux (2013), Teleseismic correlations of ambient seismic noise for deep global imaging of the earth, *Geophysical Journal International*, *194*(2), 844–848.

Bowden, D. C., and V. C. Tsai (2017), Earthquake ground motion amplification for surface waves, *Geophysical Research Letters*, *44*(1), 121–127.

Branch, M. A., T. F. Coleman, and Y. Li (1999), A subspace, interior, and conjugate gradient method for large-scale bound-constrained minimization problems, *SIAM Journal on Scientific Computing*, *21*(1), 1–23.

Brune, J. N. (1970), Tectonic stress and the spectra of seismic shear waves from earthquakes, *Journal of geophysical research*, *75*(26), 4997–5009.

Calderoni, G., A. Rovelli, Y. Ben-Zion, and R. Di Giovambattista (2015), Along-strike rupture directivity of earthquakes of the 2009 L'Aquila, central italy, seismic sequence, *Geophysical Journal International*, *203*(1), 399–415.

Campus, P., and S. Das (2000), Comparison of the rupture and radiation characteristics of intermediate and deep earthquakes, *Journal of Geophysical Research: Solid Earth*, *105*(B3), 6177–6189.

Chambers, K., J. Woodhouse, and A. Deuss (2005), Topography of the 410-km discontinuity from pp and ss precursors, *Earth and Planetary Science Letters*, *235*(3-4), 610–622.

Chen, X., and P. Shearer (2011), Comprehensive analysis of earthquake source spectra and swarms in the salton trough, california, *Journal of Geophysical Research: Solid Earth*, *116*(B9).

Chen, Y., and L. Wen (2015), Global large deep-focus earthquakes: Source process and cascading failure of shear instability as a unified physical mechanism, *Earth and Planetary Science Letters*, *423*, 134–144.

Chounet, A., M. Vallée, M. Causse, and F. Courboulex (2018), Global catalog of earthquake rupture velocities shows anticorrelation between stress drop and rupture velocity, *Tectonophysics*, *733*, 148–158.

Claerbout, J. F. (1968), Synthesis of a layered medium from its acoustic transmission response, *Geophysics*, *33*(2), 264–269.

Cooley, J. W., and J. W. Tukey (1965), An algorithm for the machine calculation of complex fourier series, *Mathematics of computation*, *19*(90), 297–301.

Cotton, F., R. Archuleta, and M. Causse (2013), What is sigma of the stress drop? seis-mol res lett 84: 42–48.

Courboulex, F., M. Vallée, M. Causse, and A. Chounet (2016), Stress-drop variability of shallow earthquakes extracted from a global database of source time functions, *Seismological Research Letters*, *87*(4), 912–918.

Courboulex, F., D. A. Castro-Cruz, A. Laurendeau, L. F. Bonilla, A. Alvarado, and E. Bertrand (2022), Ground motion simulations in quito (ecuador) due to major earthquakes from the subduction zone, *Geophysical Journal International*, *229*(3), 2192–2208.

Crotwell, H. P., T. J. Owens, J. Ritsema, et al. (1999), The taup toolkit: Flexible seismic travel-time and ray-path utilities, *Seismological Research Letters*, *70*, 154–160.

Danré, P., J. Yin, B. P. Lipovsky, and M. A. Denolle (2019), Earthquakes within earthquakes: Patterns in rupture complexity, *Geophysical Research Letters*, *46*(13), 7352–7360.

Das, S., and K. Aki (1977), Fault plane with barriers: A versatile earthquake model, *Journal of geophysical research*, *82*(36), 5658–5670.

Deng, K., and Y. Zhou (2015), Wave diffraction and resolution of mantle transition zone discontinuities in receiver function imaging, *Geophysical Journal International*, *201*(3), 2008–2025.

Denolle, M. A. (2019), Energetic onset of earthquakes, *Geophysical Research Letters*, *46*(5), 2458–2466.

Denolle, M. A., and P. M. Shearer (2016), New perspectives on self-similarity for shallow thrust earthquakes, *Journal of Geophysical Research: Solid Earth*, *121*(9), 6533–6565.

Dziewonski, A. M., and D. L. Anderson (1981), Preliminary reference Earth model, *Physics of the earth and planetary interiors*, *25*(4), 297–356.

Eddy, C. L., and G. Ekström (2014), Local amplification of rayleigh waves in the continental united states observed on the usarray, *Earth and Planetary Science Letters*, *402*, 50–57.

Eshelby, J. D. (1957), The determination of the elastic field of an ellipsoidal inclusion, and related problems, *Proceedings of the Royal Society of London. Series A. Mathematical and Physical Sciences*, *241*(1226), 376–396.

Fan, W., S. S. Wei, D. Tian, J. J. McGuire, and D. A. Wiens (2019), Complex and Diverse Rupture Processes of the 2018 Mw 8.2 and Mw 7.9 Tonga-Fiji Deep Earthquakes, *Geophysical Research Letters*, *46*(5), 2434–2448.

Fischer, T. (2005), Modelling of multiple events using empirical green's functions: method, application to swarm earthquakes and implications for their rupture propagation, *Geophysical Journal International*, *163*(3), 991–1005.

Flanagan, M. P., and P. M. Shearer (1998), Global mapping of topography on transition zone velocity discontinuities by stacking ss precursors, *Journal of Geophysical Research: Solid Earth*, *103*(B2), 2673–2692.

Frankel, A., and L. Wennerberg (1989), Microearthquake spectra from the Anza, California, seismic network: site response and source scaling, *Bulletin of the Seismological Society of America*, *79*(3), 581–609.

French, S., and B. A. Romanowicz (2014), Whole-mantle radially anisotropic shear velocity structure from spectral-element waveform tomography, *Geophysical Journal International*, *199*(3), 1303–1327.

Frohlich, C. (1989), The nature of deep-focus earthquakes, *Annual Review of Earth and Planetary Sciences*, *17*(1), 227–254.

Gallovič, F., and L. Valentová (2020), Earthquake stress drops from dynamic rupture simulations constrained by observed ground motions, *Geophysical Research Letters*, *47*(4), e2019GL085,880.

Gao, S. S., and K. H. Liu (2014), Mantle transition zone discontinuities beneath the contiguous united states, *Journal of Geophysical Research: Solid Earth*, *119*(8), 6452–6468.

García, D., S. K. Singh, M. Herráiz, J. F. Pacheco, and M. Ordaz (2004), Inslab earthquakes of central mexico: Q, source spectra, and stress drop, *Bulletin of the Seismological Society of America*, *94*(3), 789–802.

Geller, R. J. (1976), Scaling relations for earthquake source parameters and magnitudes, *Bulletin of the Seismological Society of America*, *66*(5), 1501–1523.

Goertz-Allmann, B. P., A. Goertz, and S. Wiemer (2011), Stress drop variations of induced earthquakes at the basel geothermal site, *Geophysical Research Letters*, *38*(9).

Goto, K., Z. Suzuki, and H. Hamaguchi (1987), Stress distribution due to olivine-spinel phase transition in descending plate and deep focus earthquakes, *Journal of Geophysical Research: Solid Earth*, *92*(B13), 13,811–13,820.

Grand, S. P., and D. V. Helmberger (1984), Upper mantle shear structure of north america, *Geophysical Journal International*, *76*(2), 399–438.

Green, H., and P. Burnley (1989), A new self-organizing mechanism for deep-focus earthquakes, *Nature*, *341*(6244), 733.

Green, H., F. Shi, K. Bozhilov, G. Xia, and Z. Reches (2015), Phase transformation and nanometric flow cause extreme weakening during fault slip, *Nature Geoscience*, *8*(6), 484.

Green, H. W., and H. Houston (1995), The mechanics of deep earthquakes, *Annual Review of Earth and Planetary Sciences*, *23*(1), 169–213.

Gu, Y. J., A. M. Dziewoński, and G. Ekström (2003), Simultaneous inversion for mantle shear velocity and topography of transition zone discontinuities, *Geophysical Journal International*, *154*(2), 559–583.

Guo, Z., and Y. Zhou (2020), Finite-frequency imaging of the global 410-and 660-km discontinuities using ss precursors, *Geophysical Journal International*, *220*(3), 1978–1994.

Hardebeck, J. L., and A. Aron (2009), Earthquake stress drops and inferred fault strength on the hayward fault, east san francisco bay, california, *Bulletin of the Seismological Society of America*, *99*(3), 1801–1814.

Hartzell, S., C. Mendoza, and Y. Zeng (2013), Rupture model of the 2011 mineral, virginia, earthquake from teleseismic and regional waveforms, *Geophysical Research Letters*, *40*(21), 5665–5670.

Haugland, S. M., J. Ritsema, D. Sun, J. Trampert, and M. Koroni (2020), Common reflection point mapping of the mantle transition zone using recorded and 3-d synthetic scs reverberations, *Geophysical Journal International*, *220*(1), 724–736.

Hayes, G. P. (2017), The finite, kinematic rupture properties of great-sized earthquakes since 1990, *Earth and Planetary Science Letters*, *468*, 94–100.

Hopper, E., and K. M. Fischer (2018), The changing face of the lithosphere-asthenosphere boundary: Imaging continental scale patterns in upper mantle structure across the contiguous us with sp converted waves, *Geochemistry, Geophysics, Geosystems*, *19*(8), 2593–2614.

Houston, H. (2015), 4.13 - Deep Earthquakes, in *Treatise on Geophysics (Second Edition)*, edited by G. Schubert, second edition ed., pp. 329 – 354, Elsevier, Oxford, doi:https://doi.org/10.1016/B978-0-444-53802-4.00079-8.

Huang, Y., and J.-P. Ampuero (2011), Pulse-like ruptures induced by low-velocity fault zones, *Journal of Geophysical Research: Solid Earth*, *116*(B12).

Huang, Y., G. C. Beroza, and W. L. Ellsworth (2016), Stress drop estimates of potentially induced earthquakes in the Guy-Greenbrier sequence, *Journal of Geophysical Research: Solid Earth*, *121*(9), 6597–6607.

Ide, S., E. Araki, and H. Matsumoto (2021), Very broadband strain-rate measurements along a submarine fiber-optic cable off cape muroto, nankai subduction zone, japan, *Earth, Planets and Space*, *73*(1), 1–10.

Imanishi, K., and W. L. Ellsworth (2006), Source scaling relationships of microearthquakes at Parkfield, CA, determined using the SAFOD pilot hole seismic array, *Earthquakes: Radiated Energy and the Physics of Faulting*, *170*, 81–90.

Ji, C., and R. J. Archuleta (2021), Two empirical double-corner-frequency source spectra and their physical implications, *Bulletin of the Seismological Society of America*, *111*(2), 737–761.

Ji, C., and R. J. Archuleta (2022), A source physics interpretation of nonself-similar double-corner-frequency source spectral model ja19_2s, *Seismological Society of America*, *93*(2A), 777–786.

Kanamori, H., and D. L. Anderson (1975), Theoretical basis of some empirical relations in seismology, *Bulletin of the seismological society of America*, *65*(5), 1073–1095.

Kanamori, H., and E. E. Brodsky (2004), The physics of earthquakes, *Reports on Progress in Physics*, *67*(8), 1429.

Kanamori, H., D. L. Anderson, and T. H. Heaton (1998), Frictional melting during the rupture of the 1994 Bolivian earthquake, *Science*, *279*(5352), 839–842.

Kaneko, Y., and P. Shearer (2014), Seismic source spectra and estimated stress drop derived from cohesive-zone models of circular subshear rupture, *Geophysical Journal International*, *197*(2), 1002–1015.

Kaneko, Y., and P. Shearer (2015), Variability of seismic source spectra, estimated stress drop, and radiated energy, derived from cohesive-zone models of symmetrical and asymmetrical circular and elliptical ruptures, *Journal of Geophysical Research: Solid Earth*, *120*(2), 1053–1079.

Karato, S.-i., M. R. Riedel, and D. A. Yuen (2001), Rheological structure and deformation of subducted slabs in the mantle transition zone: implications for mantle circulation and deep earthquakes, *Physics of the Earth and Planetary Interiors*, *127*(1-4), 83–108.

Kikuchi, M., and H. Kanamori (1994), The mechanism of the Deep Bolivia Earthquake of June 9, 1994, *Geophysical Research Letters*, *21*(22), 2341–2344, doi:10.1029/94GL02483.

Kirby, S. H. (1987), Localized polymorphic phase transformations in high-pressure faults and applications to the physical mechanism of deep earthquakes, *Journal of Geophysical Research: Solid Earth*, *92*(B13), 13,789–13,800.

Komatitsch, D., and J. Tromp (2002), Spectral-element simulations of global seismic wave propagation—i. validation, *Geophysical Journal International*, *149*(2), 390–412.

Komatitsch, D., Z. Xie, E. Bozdağ, E. Sales de Andrade, D. Peter, Q. Liu, and J. Tromp (2016), Anelastic sensitivity kernels with parsimonious storage for adjoint tomography and full waveform inversion, *Geophysical Journal International*, *206*(3), 1467–1478.

Koroni, M., and J. Trampert (2016), The effect of topography of upper-mantle discontinuities on ss precursors, *Geophysical Journal International*, *204*(1), 667–681.

Koroni, M., and J. Trampert (2021), Imaging global mantle discontinuities: a test using full-waveforms and adjoint kernels, *Geophysical Journal International*, *226*(3), 1498–1516.

Laske, G., G. Masters, Z. Ma, and M. Pasyanos (2013), Update on crust1. 0—a 1-degree global model of earth's crust, in *Geophysical research abstracts*, vol. 15, p. 2658, EGU General Assembly 2013, Vienna, Austria.

Lay, T., and H. Kanamori (1981), An asperity model of large earthquake sequences, *Earthquake prediction: An international review*, *4*, 579–592.

Lay, T., H. Kanamori, and L. Ruff (1982), *The asperity model and the nature of large subduction zone earthquakes*, na.

Li, J., T. Kim, N. Lapusta, E. Biondi, and Z. Zhan (2023), The break of earthquake asperities imaged by distributed acoustic sensing, *Nature*, *620*(7975), 800–806.

Li, Y., C. Doll Jr, and M. Toksöz (1995), Source characterization and fault plane determination for mblg= 1.2 to 4.4 earthquakes in the charlevoix seismic zone, quebec, canada, *Bulletin of the Seismological Society of America*, *85*(6), 1604–1621.

Lin, Y.-Y., and N. Lapusta (2018), Microseismicity simulated on asperity-like fault patches: On scaling of seismic moment with duration and seismological estimates of stress drops, *Geophysical Research Letters*, *45*(16), 8145–8155.

Lindsey, N. J., and E. R. Martin (2021), Fiber-optic seismology, *Annual Review of Earth and Planetary Sciences*, *49*, 309–336.

Lindsey, N. J., T. C. Dawe, and J. B. Ajo-Franklin (2019), Illuminating seafloor faults and ocean dynamics with dark fiber distributed acoustic sensing, *Science*, *366*(6469), 1103–1107.

Liu, M., Y. Huang, and J. Ritsema (2020), Stress drop variation of deep-focus earthquakes based on empirical green's functions, *Geophysical Research Letters*, *47*(9), e2019GL086,055.

Liu, T., and P. M. Shearer (2021), Complicated lithospheric structure beneath the contiguous us revealed by teleseismic s-reflections, *Journal of Geophysical Research: Solid Earth*, *126*(5), e2020JB021,624.

Lu, C., and S. P. Grand (2016), The effect of subducting slabs in global shear wave tomography, *Geophysical Journal International*, *205*(2), 1074–1085.

Luco, J. E. (1985), On strong ground motion estimates based on models of the radiated spectrum, *Bulletin of the Seismological Society of America*, *75*(3), 641–649.

Madariaga, R. (1976), Dynamics of an expanding circular fault, *Bulletin of the Seismological Society of America*, *66*(3), 639–666.

Masters, G., J. Woodhouse, and G. Freeman (2011), Mineos v1.0.2 [software], doi:NoDOI.

Meade, C., and R. Jeanloz (1991), Deep-focus earthquakes and recycling of water into the earth's mantle, *Science*, *252*(5002), 68–72.

Meng, L., J.-P. Ampuero, and R. Bürgmann (2014), The 2013 Okhotsk deep-focus earthquake: Rupture beyond the metastable olivine wedge and thermally controlled rise time near the edge of a slab, *Geophysical Research Letters*, *41*(11), 3779–3785.

Motazedian, D., and G. M. Atkinson (2005), Stochastic finite-fault modeling based on a dynamic corner frequency, *Bulletin of the Seismological Society of America*, *95*(3), 995–1010.

Moulik, P., and G. Ekström (2014), An anisotropic shear velocity model of the earth's mantle using normal modes, body waves, surface waves and long-period waveforms, *Geophysical Journal International*, *199*(3), 1713–1738.

Mueller, C. S. (1985), Source pulse enhancement by deconvolution of an empirical Green's function, *Geophysical Research Letters*, *12*(1), 33–36.

Neele, F., H. de Regt, and J. Van Decar (1997), Gross errors in upper-mantle discontinuity topography from underside reflection data, *Geophysical Journal International*, *129*(1), 194–204.

Nishida, K. (2013), Global propagation of body waves revealed by cross-correlation analysis of seismic hum, *Geophysical Research Letters*, *40*(9), 1691–1696.

Noda, H., N. Lapusta, and H. Kanamori (2013), Comparison of average stress drop measures for ruptures with heterogeneous stress change and implications for earthquake physics, *Geophysical Journal International*, *193*(3), 1691–1712.

Oth, A. (2013), On the characteristics of earthquake stress release variations in japan, *Earth and Planetary Science Letters*, *377*, 132–141.

Paola, N. D., R. E. Holdsworth, C. Viti, C. Collettini, and R. Bullock (2015), Can grain size sensitive flow lubricate faults during the initial stages of earthquake propagation?, *Earth and Planetary Science Letters*, *431*, 48 – 58, doi:https://doi.org/10.1016/j.epsl.2015.09.002.

Papageorgiou, A. S., and K. Aki (1983), A specific barrier model for the quantitative description of inhomogeneous faulting and the prediction of strong ground motion. i. description of the model, *Bulletin of the Seismological Society of America*, *73*(3), 693–722.

Park, S., V. C. Tsai, and M. Ishii (2019), Frequency-dependent p wave polarization and its subwavelength near-surface depth sensitivity, *Geophysical Research Letters*, *46*(24), 14,377–14,384.

Pedersen, H., and A. Colombi (2018), Body waves from a single source area observed in noise correlations at arrival times of reflections from the 410 discontinuity, *Geophysical Journal International*, *214*(2), 1125–1135.

Persh, S. E., and H. Houston (2004), Strongly depth-dependent aftershock production in deep earthquakes, *Bulletin of the Seismological Society of America*, *94*(5), 1808–1816.

Poli, P., and G. A. Prieto (2016), Global rupture parameters for deep and intermediate-depth earthquakes, *Journal of Geophysical Research: Solid Earth*, *121*(12), 8871–8887.

Poli, P., M. Campillo, H. Pedersen, and L. W. Group (2012), Body-wave imaging of earth's mantle discontinuities from ambient seismic noise, *Science*, *338*(6110), 1063–1065.

Prieto, G. A., B. Froment, C. Yu, P. Poli, and R. Abercrombie (2017), Earthquake rupture below the brittle-ductile transition in continental lithospheric mantle, *Science Advances*, *3*(3), e1602,642.

Purvance, M. D., and J. G. Anderson (2003), A comprehensive study of the observed spectral decay in strong-motion accelerations recorded in guerrero, mexico, *Bulletin of the Seismological Society of America*, *93*(2), 600–611.

Revenaugh, J., and T. H. Jordan (1991), Mantle layering from scs reverberations: 2. the transition zone, *Journal of Geophysical Research: Solid Earth*, *96*(B12), 19,763–19,780.

Ritsema, J., H. J. van Heijst, and J. H. Woodhouse (2004), Global transition zone tomography, *Journal of Geophysical Research: Solid Earth*, *109*(B2).

Ritsema, J., A. Deuss, H. Van Heijst, and J. Woodhouse (2011), S40rts: a degree-40 shear-velocity model for the mantle from new rayleigh wave dispersion, teleseismic traveltime and normal-mode splitting function measurements, *Geophysical Journal International*, *184*(3), 1223–1236.

Ross, Z. E., and Y. Ben-Zion (2016), Toward reliable automated estimates of earthquake source properties from body wave spectra, *Journal of Geophysical Research: Solid Earth*, *121*(6), 4390–4407.

Ruhl, C., R. Abercrombie, and K. Smith (2017), Spatiotemporal variation of stress drop during the 2008 Mogul, Nevada, earthquake swarm, *Journal of Geophysical Research: Solid Earth*, *122*(10), 8163–8180.

Rychert, C. A., S. Rondenay, and K. M. Fischer (2007), P-to-s and s-to-p imaging of a sharp lithosphere-asthenosphere boundary beneath eastern north america, *Journal of Geophysical Research: Solid Earth*, *112*(B8).

Sato, T., and T. Hirasawa (1973), Body wave spectra from propagating shear cracks, *Journal of Physics of the Earth*, *21*(4), 415–431.

Savage, J. (1972), Relation of corner frequency to fault dimensions, *Journal of geophysical research*, *77*(20), 3788–3795.

Shearer, P. M. (1990), Seismic imaging of upper-mantle structure with new evidence for a 520-km discontinuity, *Nature*, *344*(6262), 121–126.

Shearer, P. M. (1991), Constraints on upper mantle discontinuities from observations of long-period reflected and converted phases, *Journal of Geophysical Research: Solid Earth*, *96*(B11), 18,147–18,182.

Shearer, P. M., and J. Buehler (2019), Imaging upper-mantle structure under usarray using long-period reflection seismology, *Journal of Geophysical Research: Solid Earth*, *124*(9), 9638–9652.

Shearer, P. M., G. A. Prieto, and E. Hauksson (2006), Comprehensive analysis of earthquake source spectra in southern California, *Journal of Geophysical Research: Solid Earth*, *111*(B6).

Shearer, P. M., R. E. Abercrombie, D. T. Trugman, and W. Wang (2019), Comparing egf methods for estimating corner frequency and stress drop from p wave spectra, *Journal of Geophysical Research: Solid Earth*, *124*(4), 3966–3986.

Sitharam, T., and P. Anbazhagan (2007), Seismic hazard analysis for the bangalore region, *Natural Hazards*, *40*, 261–278.

Sotiriadis, D., B. Margaris, N. Klimis, and A. Sextos (2021), Implications of high-frequency decay parameter,"κ-kappa", in the estimation of kinematic soil-structure interaction effects, *Soil Dynamics and Earthquake Engineering*, *144*, 106,665.

Tian, D., S. S. Wei, W. Wang, and F. Wang (2022), Stress drops of intermediate-depth and deep earthquakes in the tonga slab, *Journal of Geophysical Research: Solid Earth*, *127*(10), e2022JB025,109.

Tingle, T. N., H. W. Green, C. H. Scholz, and T. Koczynski (1993), The rheology of faults triggered by the olivine-spinel transformation in $\mathrm{Mg_2GeO_4}$ and its implications for the mechanism of deep-focus earthquakes, *Journal of Structural Geology*, *15*(9-10), 1249–1256.

Tkalčić, H., T.-S. Phm, and S. Wang (2020), The earth's coda correlation wavefield: Rise of the new paradigm and recent advances, *Earth-Science Reviews*, *208*, 103,285.

Tromp, J., C. Tape, and Q. Liu (2005), Seismic tomography, adjoint methods, time reversal and banana-doughnut kernels, *Geophysical Journal International*, *160*(1), 195–216.

Trugman, D. T. (2020), Stress-drop and source scaling of the 2019 ridgecrest, california, earthquake sequence, *Bulletin of the Seismological Society of America*, *110*(4), 1859–1871.

Trugman, D. T., and P. M. Shearer (2017), Application of an improved spectral decomposition method to examine earthquake source scaling in southern california, *Journal of Geophysical Research: Solid Earth*, *122*(4), 2890–2910.

Trugman, D. T., S. L. Dougherty, E. S. Cochran, and P. M. Shearer (2017), Source spectral properties of small to moderate earthquakes in southern kansas, *Journal of Geophysical Research: Solid Earth*, *122*(10), 8021–8034.

Uchide, T., and K. Imanishi (2016), Small earthquakes deviate from the omega-square model as revealed by multiple spectral ratio analysis, *Bulletin of the Seismological Society of America*, *106*(3), 1357–1363.

Uchide, T., P. M. Shearer, and K. Imanishi (2014), Stress drop variations among small earthquakes before the 2011 tohoku-oki, japan, earthquake and implications for the main shock, *Journal of Geophysical Research: Solid Earth*, *119*(9), 7164–7174.

Ulrich, T., A.-A. Gabriel, J.-P. Ampuero, and W. Xu (2019), Dynamic viability of the 2016 mw 7.8 kaikōura earthquake cascade on weak crustal faults, *Nature communications*, *10*(1), 1213.

Vallée, M. (2013), Source time function properties indicate a strain drop independent of earthquake depth and magnitude, *Nature communications*, *4*, 2606.

Vallée, M., and V. Douet (2016), A new database of source time functions (stfs) extracted from the scardec method, *Physics of the Earth and Planetary Interiors*, *257*, 149–157.

Van der Lee, S., and G. Nolet (1997), Upper mantle s velocity structure of north america, *Journal of Geophysical Research: Solid Earth*, *102*(B10), 22,815–22,838.

Viens, L., M. Perton, Z. J. Spica, K. Nishida, T. Yamada, and M. Shinohara (2023), Understanding surface wave modal content for high-resolution imaging of submarine sediments with distributed acoustic sensing, *Geophysical Journal International*, *232*(3), 1668–1683.

Wang, E., A. M. Rubin, and J.-P. Ampuero (2014), Compound earthquakes on a bimaterial interface and implications for rupture mechanics, *Geophysical Journal International*, *197*(2), 1138–1153.

Wang, S., and H. Tkalčić (2023), On the formation of global inter-source correlations and applications to constrain the interiors of the earth and other terrestrial planets, *Journal of Geophysical Research: Solid Earth*, *128*(8), e2023JB027,236.

Wang, Y., and S. M. Day (2017), Seismic source spectral properties of crack-like and pulse-like modes of dynamic rupture, *Journal of Geophysical Research: Solid Earth*, *122*(8), 6657–6684.

Williams, E. F., A. Ugalde, H. F. Martins, C. E. Becerril, J. Callies, M. Claret, M. R. Fernandez-Ruiz, M. Gonzalez-Herraez, S. Martin-Lopez, J. L. Pelegri, et al. (2023), Fiber-optic observations of internal waves and tides, *Journal of Geophysical Research: Oceans*, p. e2023JC019980.

Wu, Q., M. Chapman, and X. Chen (2018), Stress-drop variations of induced earthquakes in oklahoma, *Bulletin of the Seismological Society of America*, *108*(3A), 1107–1123.

Xu, W., C. Lithgow-Bertelloni, L. Stixrude, and J. Ritsema (2008), The effect of bulk composition and temperature on mantle seismic structure, *Earth and Planetary Science Letters*, *275*(1-2), 70–79.

Ye, L., T. Lay, H. Kanamori, and K. D. Koper (2013), Energy release of the 2013 Mw 8.3 Sea of Okhotsk earthquake and deep slab stress heterogeneity, *Science*, *341*(6152), 1380–1384.

Ye, L., T. Lay, H. Kanamori, and L. Rivera (2016), Rupture characteristics of major and great (mw7.0) megathrust earthquakes from 1990 to 2015: 1. source parameter scaling relationships, *Journal of Geophysical Research: Solid Earth*, *121*(2), 826–844, doi:https://doi.org/10.1002/2015JB012426.

Yin, J., Z. Li, and M. A. Denolle (2021), Source time function clustering reveals patterns in earthquake dynamics, *Seismological Society of America*, *92*(4), 2343–2353.

Yoshioka, S., R. Daessler, and D. A. Yuen (1997), Stress fields associated with metastable phase transitions in descending slabs and deep-focus earthquakes, *Physics of the earth and planetary interiors*, *104*(4), 345–361.

Yu, H., R. M. Harrington, H. Kao, Y. Liu, R. E. Abercrombie, and B. Wang (2020), Well proximity governing stress drop variation and seismic attenuation associated with hydraulic fracturing induced earthquakes, *Journal of Geophysical Research: Solid Earth*, *125*(9), e2020JB020,103.

Zhan, Z. (2017), Gutenberg–Richter law for deep earthquakes revisited: A dual-mechanism hypothesis, *Earth and Planetary Science Letters*, *461*, 1–7.

Zhan, Z. (2020), Distributed acoustic sensing turns fiber-optic cables into sensitive seismic antennas, *Seismological Research Letters*, *91*(1), 1–15.

Zhan, Z., S. Ni, D. V. Helmberger, and R. W. Clayton (2010), Retrieval of moho-reflected shear wave arrivals from ambient seismic noise, *Geophysical Journal International*, *182*(1), 408–420.

Zhan, Z., H. Kanamori, V. C. Tsai, D. V. Helmberger, and S. Wei (2014), Rupture complexity of the 1994 Bolivia and 2013 Sea of Okhotsk deep earthquakes, *Earth and Planetary Science Letters*, *385*, 89 – 96, doi:https://doi.org/10.1016/j.epsl.2013.10.028.

Zhan, Z., P. M. Shearer, and H. Kanamori (2015), Supershear rupture in the 24 May 2013 Mw 6.7 Okhotsk deep earthquake: Additional evidence from regional seismic stations, *Geophysical Research Letters*, *42*(19), 7941–7948.

Zhao, L., and S. Chevrot (2003), Ss-wave sensitivity to upper mantle structure: Implications for the mapping of transition zone discontinuity topographies, *Geophysical research letters*, *30*(11).

Zumberge, M. A., W. Hatfield, and F. K. Wyatt (2018), Measuring seafloor strain with an optical fiber interferometer, *Earth and Space Science*, *5*(8), 371–379.